A Light Scattering Model for Large Particles with Surface Roughness

Harry Ballington

Submitted to the University of Hertfordshire in partial fulfilment of the requirements of the degree of Doctor of Philosophy

Atmospheric and Climate Physics Group
Department of Physics, Astronomy & Mathematics
School of Physics, Engineering & Computer Science
University of Hertfordshire

October 8, 2024

Abstract

The scattering of light from particles with roughened surfaces occupies a gap in our understanding because they have size dimensions spanning multiple length scales. Subtle changes in the symmetries and features of a particles geometry can lead to significant changes in its optical properties. Combined with the fact that many applications of light scattering are concerned with the bulk properties of an ensemble of particles with varying shapes and sizes, this makes it particularly challenging to study them through experiment and to model via simulation. The goal of this work is to develop a model to solve a multi-scale problem in an approximate yet fast and computationally feasible manner, to aid in characterising the optical properties of particles with surface roughness. Accomplishing this will enhance current modelling capabilities and offer the potential to compute single scattering parameters with greater accuracy, leading to a deeper understanding across a wide range of applications.

For particles with size much larger than the wavelength, the existing work is generally limited to ray-tracing approaches based on geometric optics, as well as some physical-optics hybrid methods based on an equivalence between the orientation averaged scattering of roughened and distorted smooth particle geometries. The use of geometric optics is a good approximation if the particle size dimensions are much greater than the wavelength of light, but the accuracy decreases with decreasing size dimension. To address this limitation, the model developed in this study, the Parent Beam Tracer method, improves upon geometric optics by accounting for diffraction effects, which become important when the length scale becomes comparable to the wavelength. The basic principles of pioneering ray-tracing studies provide the inspiration for the model, which also includes a novel ray backtracing technique for application to particles with a variety of surface textures. It utilises a surface integral diffraction equation, allowing it to capture the interplay between wavelength, surface roughness, and overall particle shape in the computation of 2D scattering patterns. It is the first physical-geometric optics hybrid method of its kind to compute the full Mueller matrix from particles with surface roughness, which can be achieved in a time reduced by several orders of magnitude compared to other methods, such as the discrete dipole approximation. By comparison of 2D scattering patterns measured by experiment with those predicted by the model, the prospective user may be able to better characterise particles beyond the capabilities of current resolution-limited imaging techniques. In summary, this report details the key findings based on the development of a physical-optics hybrid light scattering model for particles with overall size[1] much larger than the wavelength of light, but with surface roughness on a scale comparable to the wavelength. In addition, this work describes new evidence showing that the length scale of surface roughness has a negligible effect on the orientation averaged scattering, suggesting that surface roughness can be quantified solely by an amplitude.

This report is structured into the following sections: First, a range of applications are introduced in Section 1, and the motivation for developing the model is discussed. A brief review of existing literature is given, with particular emphasis on the difficulties encountered

[1] Overall size is intended to be the largest characteristic length scale of the particle, which may be loosely interpreted as the diameter of a sphere with the same volume.

in representing the size, shape, and surface texture of particles in theoretical light scattering models. The analysis of 2D scattering patterns as a means of characterising particles beyond the resolution of current imaging techniques is also discussed. Second, an introduction to some basic scattering theory is given in Section 2, which may be a useful resource for the reader for a better understanding of the proceeding sections. Third, Section 3 gives a brief review of some existing theoretical methods, with a greater depth of focus on the principles of geometric optics. These principles are then leveraged in Section 4, which describes and explains the novel techniques in the Parent Beam Tracer method. Section 5 discusses applications of the model; 2 benchmark studies comparing its accuracy against the numerically exact discrete dipole approximation are presented, as well as a study on the single scattering properties of roughened, thin hexagonal plates across a range of sizes and refractive indices. The work is summarised in Section 6, which concludes this report.

Acknowledgements

I would like to express my deepest thanks to my supervisors, Dr. Evelyn Hesse and Prof. Ranjeet Sokhi.

To Ranjeet, I sincerely appreciate of his professional approach to research, and his understanding of the academic process. I am grateful for his guidance towards an understanding of the wider application of my work, and for his mentorship in connecting results with the work of other experts in research.

To Evelyn, I am immensely thankful for her unwavering patience and support throughout the course of this project. Her feedback, support, and expertise has been invaluable, not only towards the progress of this work, but also in fostering my growth and objectives as a researcher. I am grateful for her belief and interest in my ideas, and for the many hours we have spent in discussion. Thank you for being a source of inspiration and support throughout this process, which has been both a challenging and a rewarding one.

I am grateful for the developers of the ADDA computer code, which has been an invaluable tool for validating results during this project. Dr. Antti Penttilä deserves a special thanks for making available his Fortran computer codes, without which were very useful for ADDA computations for particles with surface roughness.

Contents

Chapter 1

Introduction

1.1 Applications and Motivation

Light scattering is a fundamental process with extensive applications across various fields. Calibration of laboratory instrumentation relies on theoretical calculations, and the discernment of cell health or disease in biomedical testing is informed by the examination of single scattering properties [1, 2]. This includes, for instance, detection of rupturing or destruction of red blood cells (hemolysis) from smoking [3]; an affected cell is shown in Figure 1.1. Flow cytometry is a powerful tool based on light scattering for measuring the size and internal complexity or granularity of cells [4]. It is used in many applications, including immunology, molecular biology, bacteriology, virology, cancer biology, and infectious disease monitoring. In occupational health, light scattering is used to monitor dust sizes, to prevent dust explosions in industries, and to detect hazardous substances like asbestos [5–7]. An example of a butuminous coal particle is shown in Figure 1.1b, of which the flammability generally decreases with increasing size [5].

In the marine environment, which is composed of the oceans, floating sea ice, and the atmosphere above, light is scattered and absorbed by a variety of particles, including aerosols, particles and bubbles in suspension, and grain boundaries in sea ice. The scattering effects of which, are influenced by particle size, shape, refractive index, and the angle of scattering. Understanding the scattering process is important for understanding cloud formation, radiative transfer, heating and cooling of the Earth, as well as visibility, which plays a role in the life of humans and marine ecology. In the submarine environment, ambient light is significantly polarised, and many creatures have evolved to use this to their advantage. Some species of crustacean have evolved to have nearly transparent bodies, making them less visible to predators. Some crustaceans and cephaloids use dichroic channels in their retinas to use polarised light to help them navigate underwater. The increasing use of diesel in marine transport is thought to be a major source of carbonaceous soot in the marine environment. These particles have high refractive index in both the real and imaginary components, which mean they have an important effect on the scattering of light. An iron-oxide particle derived from diesel combustion is shown in Figure 1.1c [8]. Strong evidence also exists, suggesting that photosynthesis productivity is sensitive to the handedness of circularly polarised light [10]. Right-handed polarisation is thought to increase productivity in *Dunaliella euchlora*

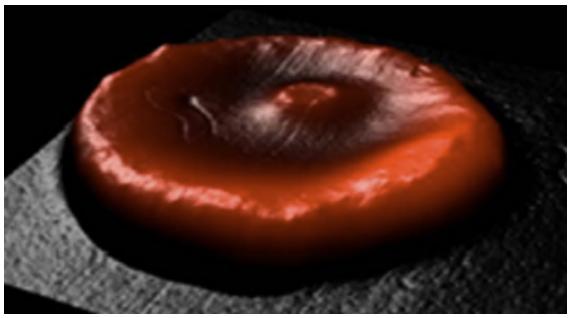

(a) Deformed red blood cell with diameter 12 µm [3].

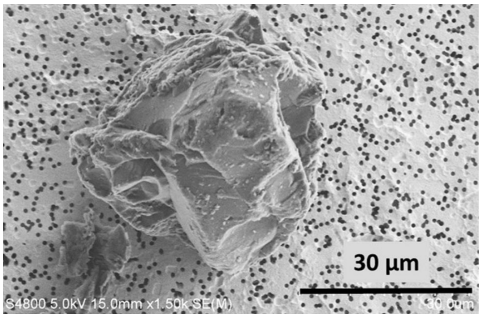

(b) Bituminous coal dust particle [5].

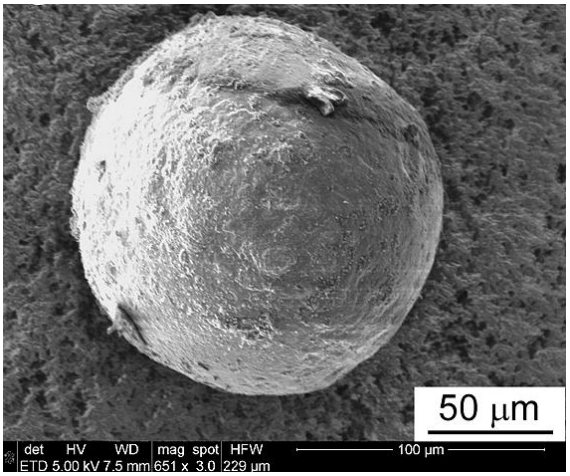

(c) Scanning electro micrograph of a nearly spherical iron-oxide particle derived from diesel [8].

(d) Vegetative, green *Dunaliella euchlora* cell [9]. The bar represents 10 µm.

Figure 1.1

algae (Figure 1.1d), which may be due to the circular dichroism in the pigments. Many scatterers have been found to show a degree of non-random group orientation, such as marine organisms and inorganic materials like sediments and dust. Clearly, light scattering is an important process in the marine environment.

Weather and climate models rely on single scattering parameters as inputs to radiative transfer computations [11], which are important for understanding and predicting the Earth's climate system. Cirrus clouds play an important role in the Earth-atmosphere radiative balance owing to their large global coverage [12]. They take on the appearance of fibrous, threadlike, white-feather clouds resembling hair curls, and are composed primarily of ice crystals ranging in sizes from microns to millimeters [13]. Fundamental understanding of the light-scattering and polarisation effects of ice particles is a useful tool in the interpretation of bidirectional reflectances, fluxes, and heating rates [14, 15]. Multiple scattering calculations are important for determining irradiances in climate studies and radiances in remote sensing. The accurate calculation of scattering matrices and integrated parameters, including single scattering albedo, asymmetry parameter, and scattering and extinction cross sections and efficiencies, remains central to these applications.

A quantitative analysis of light scattering can provide a useful tool for applications with specific angular detection ranges and resolution. For example, the instruments of the Small Ice Detector family [16] detect light scattered in the region between 6° and 25° from the forwards direction, which is useful for studying halos and coronae phenomena caused by ice crystals. Light detection and ranging (Lidar) instruments detect direct backscattering and is a valuable tool for remote-sensing applications. The backscattered light is analysed, which can give valuable insights about the particles present. An understanding of how the shape, size, and refractive index of a particle affects the backscattering is therefore of importance for interpreting results. Lidar is a useful technique because it is non-invasive, and the instrumentation can be situated on ground, in high-flying aircraft, or even on satellites. In the study of aerosols, Lidar can be used to analyse exotic clouds, and detect dust storms and wildfires. For water and mixed-phase clouds, it can be used to distinguish between liquid water and ice. With Lidar, the life cycle of raindrops can be traced as they fall, starting initially as snowflakes which melt into irregular, mixed phase particles, before collapsing into inhomogeneous, ice-containing raindrops [14]. An array of applications are focused on the inversion problem, where theoretical models are employed alongside experimental data to determine the size, shape, and particle complexity of a scatterer [17]. Two-wavelength detection can provide information about particle size and aid in discrimination of clouds and aerosols, as well as the identification of aerosol types [18].

The list of applications concerned with ice particles extends beyond the study of light scattering on Earth. Images taken of Enceladus, the sixth largest moon of Saturn, reveal the presence of ice and dust particles emitted from cryovolcanoes [19]. Analysis of the scattering from such particles is of interest, since life on Earth is thought to have originated from hydrothermal vents [20]. Astronomical data suggests that the ice particles are likely to be non-spherical in shape [21]. Ice crystal formation depends on temperature and supersaturation in general, which influence the hydrogen bonding, leading to most commonly hexagonal, sometimes cubical, and occasionally trigonal structures. It has been highlighted that more accurate light scattering simulations of such particles would be of great value in this area of research.

The physics of light scattering is governed by Maxwell's equations of electromagnetism. Light waves propagate according to the wave equation, a fundamental topic found in elementary textbooks [22]. For time harmonic fields, the physics is described by the vector Helmholtz equation [14, 23],

$$\nabla^2 \mathbf{E_{sca}} + n^2 k^2 \mathbf{E_{sca}} = 0, \tag{1.1}$$

where $\mathbf{E_{sca}}$ is the scattered electric field, n is refractive index, and k is the wavenumber. The solutions to which, depend on the particle refractive index n, as well as the size, shape, orientation, and surface roughness, which determine the boundary conditions. The material composition of a particle determines its refractive index, which also depends on the wavelength λ of the incident light. Solving the vector Helmholtz equation for single particles to obtain results of practical importance, however, is encumbered by the diverse array of particles found in nature. For instance, the bulk scattering properties of cirrus clouds, mineral dust clouds, or volcanic ash plumes depend on the properties of their constituent individual particles. In such cases, it is practically impossible to know the exact details of each particle.

The ensemble of particles is usually represented by a particle size distribution (PSD), which is obtained by fitting observational data to a gamma distribution [24]. The gamma distribution depends on the maximum particle dimension, as well as several parameters derived from the fitting process. The PSD is used to estimate the particle mass, cross-sectional area, and terminal velocity, from which the bulk cloud properties can be calculated [25]. For radiative transfer applications, single-scattering parameters are computed using light scattering models for a variety of particle habits. Here, the term "habit" describes the shape of the particle, which usually varies with particle size and atmospheric conditions. For example, common ice crystal habits include plates, columns (solid, hollow, or capped), needles, dendrites, bullet rosettes, and aggregates. Some captured cirrus particles are shown in Figure 1.2 [26]. Since light scattering simulations are size-dependent, the scattering is typically computed across a number of size bins spanning the range of the PSD. The effect of this, alongside the grouping of particles into sets of simplified habits, must give rise to some degree of error in the results. This affects the accuracy of weather and climate forecasting, which are influenced by the accuracy of single scattering properties derived from theoretical models.

1.2 Characterisation of Particle Geometry

The applicability of different theoretical light scattering models is heavily dependent on the size and shape of the particle. In 1932, Wadell proposed a characterization approach for nonspherical particles based on form, roundness, and surface texture [27]. The following sections discuss how these factors influence the physics of light scattering and the implications they have on the applicable theoretical methods and experimental techniques.

1.2.1 Size

With regards to size, the applicable methods generally depend on whether the particle size is much smaller than, comparable to, or much greater than the wavelength λ of incident light.

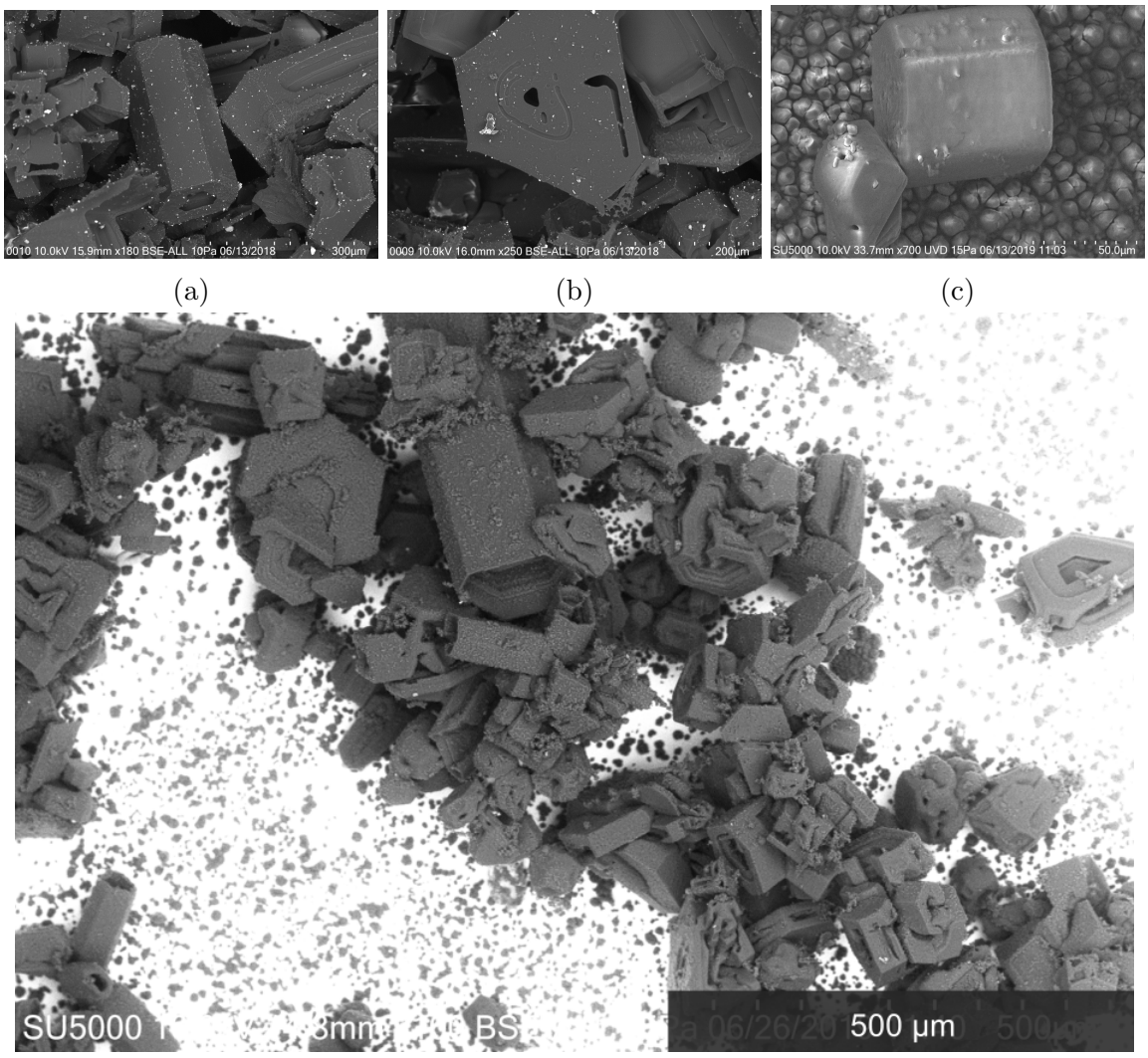

(a) (b) (c)

(d)

Figure 1.2: Cirrus particles captured in high definition with scanning electron cryomicroscopy [26].

Particles much smaller than the wavelength of incident light fall under the regime of Rayleigh scattering, with a scattered irradiance that scales proportional to $1/\lambda^4$ [28]. For particles with size dimensions comparable to the wavelength, which is sometimes referred to as the induction zone [29], a wide variety of methods exist. On the other end of the scale, particles with size dimensions much greater than the wavelength can usually be approximated by the laws of geometric optics, which models the propagation of light as moving along well defined paths known as rays. Several computationally efficient approaches using classical geometric optics (GO) were initially developed [30–34]. The methods use ray-tracing techniques to model the propagation of electromagnetic waves in the short wavelength limit as straight-line paths. Muinonen devised the modified Kirchhoff approximation, accounting for Fraunhofer diffraction in the forwards direction, as well as from reflected and transmitted beams, by approximating the diffracting surfaces as circular apertures [32]. Macke used an alternative method, accounting for external diffraction in the forwards direction by using the particle projected cross section as the diffracting aperture [35]. These approaches provide an approximate solution to the scattering problem with an accuracy that increases with the minimum dimension of the particle [36]. In recent years, several so-called physical-optics hybrid methods have been developed, which improve upon GO by accounting for additional diffractive effects [37–41] (further discussed in Sections 3.4.6 & 4.3). While these methods have been used to model a variety of particle geometries with smooth surfaces, few can be directly applied to compute light scattering from particles with surface roughness. Instead, several approaches are focused on the effects of deviations from perfect particle geometries. For instance, one of the first and now widely used techniques for this is the 'tilted-facets' method, which applies a stochastic distortion to the particle surface [35]. Another approach, which uses distorted smooth particle shapes to mimic varying degrees of surface roughness [42], has been implemented in several recent works [43–46]. A physical-optics method based on the subdivision of an incident wave into triangle-shaped beams was also developed and used to model strongly absorbing hexagonal prisms with surface roughness [47]. More discussion on theoretical methods is given in Section 3.

1.2.2 Shape

With regards to particle shape, the problem becomes more complicated. For spherical particles, Lorenz-Mie theory (Section 3.1) provides an elegant and efficient solution for computing the scattering [48]. Unfortunately, the general consensus among current research is that using Lorenz-Mie theory as an approximation for non-spherical particles can lead to significant errors. For instance, a study on the sensitivity of cirrus cloud albedo showed that assuming ice crystals to be spherical can easily lead to an overestimate of cloud optical thickness by a factor of 3 [49]. A study on the simulation of single and 3-layer cirrus cloud models found that the bidirectional reflection of cirrus is highly sensitive to whether the particles are characterised as spherical or quasi-spherical [50]. Although the shapes of ice crystals are highly varied, laboratory experiments and observations reveal that most geometries are composed of basic hexagonal structures [13]. Instead of spheres, the droxtal geometry has been proposed as a more realistic approximation for the shape of small ice particles [51]. For ice particles with 60 µm $< d <$ 1000 µm, where d is the maximum particle dimension, the aspect ratio depends on temperature, and the fraction of spherical particles in ice clouds

rapidly decreases with increasing particle size [52]. For non-spherical particles, several exact methods for solving the light scattering problem exist, including T-matrix [53–55], finite-difference time-domain [56–58], and the discrete dipole approximation [59–62]. However, these approaches become computationally expensive as the particle refractive index n and size parameter $X = |\pi d/\lambda|$ increase, where λ is the wavelength.

1.2.3 Surface Roughness

Generally speaking, surface roughness can be modelled by either using a smooth surface with modifications to the physics to simulate the effects of roughness [35, 63–65], or by generating a surface with physical roughness according to a roughness scheme, such as Koch fractals [35], Voronoi particles [66], Gaussian roughness [67–69], or Chebychev polynomial series [70].

An example of the former approach, is the tilted-facets method [35], wherein the propagation direction of reflected and refracted rays is perturbed by applying a random "tilt" to the surface in a Monte Carlo-style approach. The obvious advantage of such approaches is that they are simple and relatively straightforward to implement. The disadvantages are that the perturbed surface is not well-defined[1], which restricts the accuracy and range of methods that can be applied, and that applying excessive amounts of tilt can lead to unphysical results.

Alternatively, using a roughness scheme to generate a morphologies gives rise to particles with well-defined surfaces, which might be an analytical function or a surface mesh made up of many elements. One example is the use of Chebyshev functions, although more often these are used to represent particle distortion, instead [12, 71]. Gaussian roughness schemes are a widely adopted choice and can be defined by a standard deviation and a coherence length of an autocorrelation function [72–74]. A recent study used a statistical model based on fractional Brownian motion to produce a thin roughness element characterised by a horizontal and a vertical scale [75]. Rougher elements were found to increase transmittance through the surface and showed smoother angular scattering functions when compared with their smooth counterparts.

An advantage of knowing the precise information about the surface topology, is the applicability of more accurate theories, such as the discrete dipole approximation (DDA) [59], T-matrix [76], psuedo-spectral time-domain [77], or the discontinuous Galerkin time-domain methods [78]. Unfortunately, most roughnesses schemes are either restricted to specific geometries or defined on a case-by-case basis, which limits the ease at which they can be applied on a wider scale. One current challenge is that, since there are a multitude of ways of parametrising surface roughness, it is not always clear how to compare one roughness scheme with another. A proposed solution to this problem is a surface normal roughness metric for ice based on an analysis of anisotropic morphology in the prismatic plane, which can be applied to both modelled stochastic surfaces and observed samples [79].

The characterisation of the geometry of ice particles has proved fairly challenging owing to the sensitivity of ice crystal habits to temperature and humidity, combined with limitations of capturing images with sufficient resolution. Cirrus cloud temperatures generally

[1]The perturbation is applied independently for each ray, meaning that two rays incident at the same location will generally "see" different surfaces.

range from $-19°$ in the lower layer to $-58°$ in the upper layer [13, 51, 80]. Crystal formation of quasi-spherical geometries is favoured in the upper layer, which have aspect ratios close to 1. The middle layer is sometimes referred to as the growth layer, where pristine columns, plates, and bullets may be found, with increasing aspect ratios. In the lower layer, the air is warmer and can hold more moisture, which can lead to a state of subsaturation. This promotes sublimation, which can lead to a wide variety of complex geometries. On the macroscopic scale, pristine shapes found in the growth layer can join together to create complex formations such as rosettes and aggregates. On the microscopic scale, the sublimation is characterised by smooth and rounded shapes, as well as grooving [81]. Because of the extreme temperatures ice crystals are found in, it has been only recently possible to retrieve and preserve samples from clouds in nature. Magee et al. used a balloon-borne payload to capture, seal, and return ice particles from cirrus clouds to be analysed using a cryo-scanning election microscope [26]. Across thousands of measured cirrus particles, they observed highly varied particle shapes across different habits, including multiple scales of sub-wavelength scale roughening, and even greater complexity than previously expected. In order to circumvent the technical challenges of resolution-limited camera imaging of ice particles, there have been many attempts to indirectly determine the particle shape through the analysis of light scattered by the particles. When a surface with roughness scatters an incident wave, the interference between outgoing waves from different parts of the surface leads to a scattering pattern that contains various information about the geometrical and physical properties of the particle. The analysis of certain texture features in the image can be used retrieve information about the characteristics of the roughness of a surface [82]. The texture features can be quantified by applying a grey-level co-occurence matrix (GLCM), which relates the brightness levels between different pixels in a scattered intensity image [83]. Some examples of the features include:

- Contrast: A measure of the local variations in the GLCM.
- Correlation: The joint probability occurrence of specified pixel pairs.
- Energy: A measure of uniformity, which is equal to the sum of the squared elements in the GLCM.
- Homogeneity: A measure of the closeness of the distribution of elements in the GLCM to the GLCM diagonal.

Ulanowski et al. found that the surface area of intensity peaks, or speckle, is inversely proportional to the particle size [84]. The work was extended for inferring the roughness properties of atmospheric ice particles measured with the Small Ice Detector 3 [85]. Based on measurements of lab samples of ice and mineral dust, they formulated a combined roughness value, which is based on a combination of the energy, kurtosis, root mean square, and standard deviation of the greyscale scattered intensity pattern. It was found that most in-situ samples from flight data showed random speckle in the patterns, corresponding to very rough and/or complex ice crystal geometries.

1.3 Summary

The interaction of light with matter is a fundamental process with broad applications in fields such as biomedical testing, occupational health, marine environments, weather and climate modelling, remote sensing, and astrophysics. Understanding of how particles scatter light helps us to detect disease, calibrate instruments, monitor hazardous substances, and predict and preserve the environment. The scattering depends on the size, shape, orientation, and surface texture of the particles. In many applications, there is increasing evidence that particles are often non-spherical, which can lead to inaccurate predictions and misinterpretation of data, if spherical shapes are assumed. For particles with size much larger than the wavelength, GO is a widely adopted tool for theoretical light scattering models. If the particle size parameter is not large [86], or if the scale of surface roughness is comparable to or greater than the wavelength, then the spreading of energy, or diffraction, when light scatters, becomes more significant; an effect which is not accounted for in GO. This work aims to devise a model for computing light scattering based on GO for particles with overall size much larger than the wavelength, but with physical roughness of length scale comparable to the wavelength. Can such a model be devised, and how does its accuracy and speed compare with existing methods? Can the model also be capable of computing single-scattering parameters and 2D scattering patterns, which have great value across many applications? Before these questions can be answered, a brief overview of the theoretical framework for light scattering is described in the following chapter.

Chapter 2

Fundamental Theory of Electromagnetic Scattering

2.1 Basic Scattering Theory

In this section, the basic theory for the scattering of an electromagnetic plane wave is given. The scattering geometry consists of a particle with centre of mass located at the origin and an illuminating incident plane wave with an electromagnetic field that can be described by

$$\mathbf{E^i} = \mathbf{E_0^i} e^{ik_0(\hat{\mathbf{K}}_\mathbf{0}\cdot\mathbf{r}-\omega t)}, \tag{2.1}$$

$$\mathbf{H^i} = \mathbf{H_0^i} e^{ik_0(\hat{\mathbf{K}}_\mathbf{0}\cdot\mathbf{r}-\omega t)}, \tag{2.2}$$

where $\mathbf{E^i}$ and $\mathbf{H^i}$ are the electric and magnetic incident fields, respectively, $\hat{\mathbf{K}}_\mathbf{0} = -\hat{\mathbf{z}}$ is the propagation vector defined along the $-\hat{\mathbf{z}}$ axis, λ is the wavelength of incident light, $k_0 = 2\pi/\lambda$ is the wavenumber, ω is the angular frequency, and t is time. $\mathbf{E_0^i}$ and $\mathbf{H_0^i}$ are complex amplitude vectors and form a mutually orthognoal triad with $\hat{\mathbf{K}}_\mathbf{0}$ according to $\mathbf{H_0^i} = \hat{\mathbf{K}}_\mathbf{0} \times \mathbf{E_0^i}$. In general, the interaction of the electromagnetic field with the particle causes the energy of the wave to be redistributed into multiple directions. As a result, both the intensity and polarisation of the scattered electromagnetic field may vary as a function of position. A spherical coordinate system is introduced, with the forwards scattering direction $\theta = 0°$ is defined to be aligned with the $-\hat{\mathbf{z}}$ axis such that the position $\mathbf{r}$ at a distance R in the far-field is given by

$$\mathbf{r} = \begin{pmatrix} x \\ y \\ z \end{pmatrix} = \begin{pmatrix} R\sin\theta\cos\phi \\ R\sin\theta\sin\phi \\ -R\cos\theta \end{pmatrix}, \tag{2.3}$$

where θ and ϕ are the polar and azimuthal angles, respectively. For each unique pair of θ and ϕ values, there exists a scattering plane containing $-\hat{\mathbf{z}}$ and $\hat{\mathbf{r}}$, as shown in Figure 2.1. For $\theta = 0°$ or $\theta = 180°$, any scattering plane containing the z-axis can be used. At a large distance from the particle, it can be shown that the scattered field takes the form of an outgoing spherical wave [29], which is transverse such that the scattered electric field is perpendicular to $\hat{\mathbf{r}}$. This is called the far-field approximation ($k_0 r >> 1$), wherein the

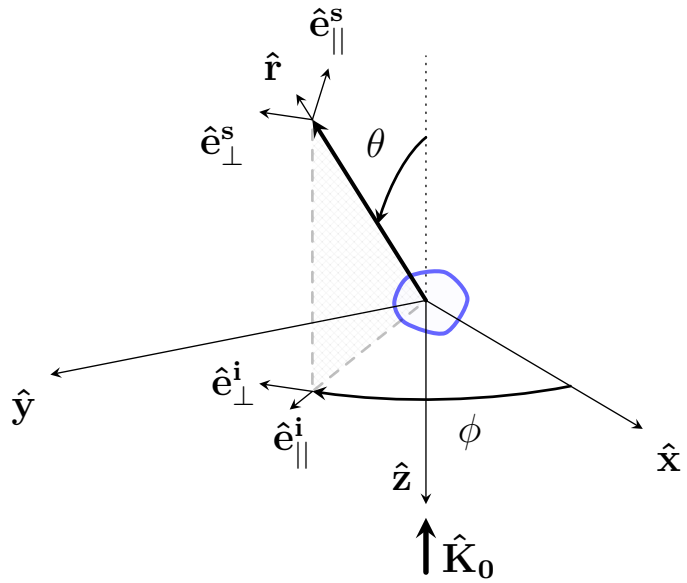

Figure 2.1: Scattering geometry for incident light along the -$\hat{\mathbf{z}}$-axis. An arbitrary scattering particle is shown in blue, centered on the origin. The scattering direction makes an angle θ to the -$\hat{\mathbf{z}}$-axis. The incident and scattered directions define the scattering plane.

scattered field at a distance r from the scatterer is described by

$$\mathbf{E^s} = \frac{e^{ik_0 r}}{-ik_0 r}\mathbf{E^s_0}. \tag{2.4}$$

Since both the incident and scattered electric fields are perpendicular to their respective propagation directions, it is convenient to split the amplitude vectors into components parallel and perpendicular to the scattering plane, such that

$$\mathbf{E^i_0} = a^i_{||}e^{i\delta^i_{||}}\hat{\mathbf{e}}^{\mathbf{i}}_{||} + a^i_{\perp}e^{i\delta^i_{\perp}}\hat{\mathbf{e}}^{\mathbf{i}}_{\perp} =, \quad \mathbf{E^s_0} = a^s_{||}e^{i\delta^s_{||}}\hat{\mathbf{e}}^{\mathbf{s}}_{||} + a^s_{\perp}e^{i\delta^s_{\perp}}\hat{\mathbf{e}}^{\mathbf{s}}_{\perp}, \tag{2.5}$$

where a and δ represent real-valued constants, and $\hat{\mathbf{e}}_{||}$ and $\hat{\mathbf{e}}_{\perp}$ are orthogonal unit vectors given by

$$\begin{aligned} \hat{\mathbf{e}}^{\mathbf{i}}_{||} &= \cos\phi\ \hat{\mathbf{x}} + \sin\phi\ \hat{\mathbf{y}}, & \hat{\mathbf{e}}^{\mathbf{i}}_{\perp} &= \sin\phi\ \hat{\mathbf{x}} + \cos\phi\ \hat{\mathbf{y}} \\ \hat{\mathbf{e}}^{\mathbf{s}}_{||} &= \cos\theta\cos\phi\ \hat{\mathbf{x}} + \cos\theta\sin\phi\ \hat{\mathbf{y}} - \sin\theta\ \hat{\mathbf{z}}, & \hat{\mathbf{e}}^{\mathbf{s}}_{\perp} &= \sin\phi\ \hat{\mathbf{x}} + \cos\phi\ \hat{\mathbf{y}}. \end{aligned}$$

A diagram summarising the scattering geometry is shown in Figure 2.1. On a macroscopic scale, a discontinuity in the electric permitivity ϵ and permeability μ occurs at the boundary between the particle and the surrounding medium (ie. on the particle surface). It is therefore common to impose the following boundary condition, which implies continuity of the tangential component of the electric field:

$$(\mathbf{E_1} - \mathbf{E_2}) \times \hat{\mathbf{n}} = 0, \tag{2.6}$$

where $\mathbf{E_1}$ and $\mathbf{E_2}$ are the electric fields on either side of the boundary and $\hat{\mathbf{n}}$ is the outward-facing surface surface normal. Based on the linearity of Eq. 2.6, a relation can be formed to relate the near and scattered fields. To this end, the amplitude scattering matrix $\mathbf{S} = \left(\begin{smallmatrix} S_2 & S_3 \\ S_4 & S_1 \end{smallmatrix}\right)$ is introduced, which relates $\mathbf{E^s}$ to $\mathbf{E^i}$ by

$$\mathbf{E}^s = \begin{pmatrix} E_{||} \\ E_{\perp} \end{pmatrix}^s = \begin{pmatrix} S_2 & S_3 \\ S_4 & S_1 \end{pmatrix} \begin{pmatrix} E_{||} \\ E_{\perp} \end{pmatrix}^i . \tag{2.7}$$

For a wave unaffected by a scatterer, the amplitude matrix is defined as the identity matrix,

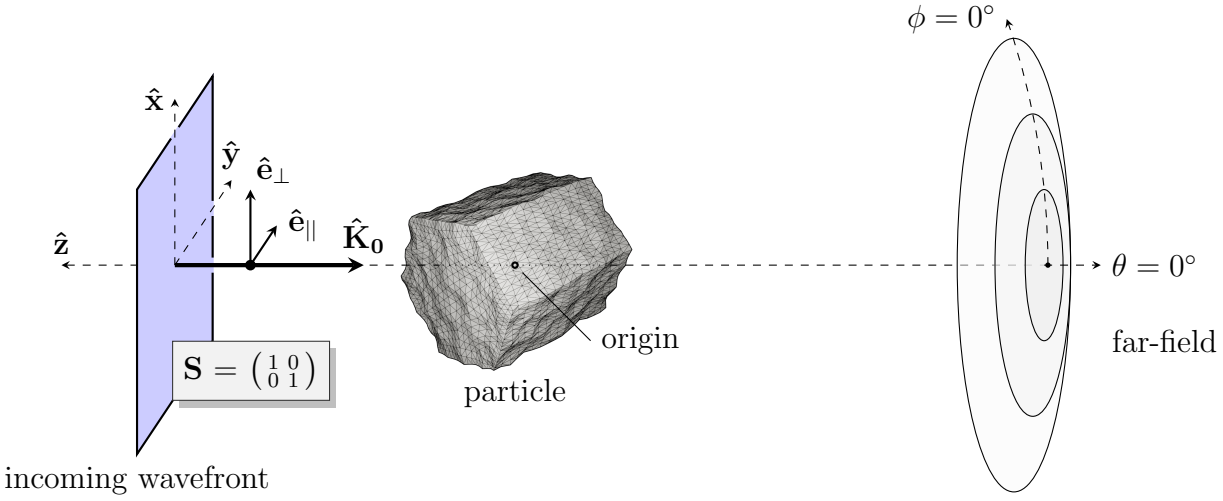

Figure 2.2: The scattering geometry. An unpolarised plane wave is incident along the $\hat{\mathbf{z}}$ axis, with perpendicular and parallel electric field vectors defined along the $\hat{\mathbf{x}}$ and $\hat{\mathbf{y}}$ axes, respectively. The particle is positioned with centre of mass on the origin. The far-field is located at a distance R from the origin, with contour lines of constant θ shown for convenience.

$\mathbf{I} = \left(\begin{smallmatrix} 1 & 0 \\ 0 & 1 \end{smallmatrix}\right)$. In this work, the initial amplitude matrix is chosen to be defined with respect to the yz plane with orthonormal field unit vectors $\hat{\mathbf{e}}_{\perp}$ and $\hat{\mathbf{e}}_{||}$ along the $\hat{\mathbf{x}}$ and $\hat{\mathbf{y}}$ directions, respectively. A diagram summarising the scattering geometry is shown in Figure 2.2.

2.2 Stokes Vectors & Amplitude Matrices

As shown in Eq. 2.5, the amplitude of a wave can be split into 2 perpendicular components. The amplitudes $a_{||}$ and $a_{\perp}$ and relative phase $\delta = \delta_{||} - \delta_{\perp}$ describe the polarisation of the wave. If $E_{\perp}$ and $E_{||}$ are fully correlated over time then the wave is said to be polarised, whereas if they are uncorrelated the wave is unpolarised [28]. The intensity, and horizontal/vertical, diagonal, and circular polarisation can be conveniently described by the Stokes parameters,

I, Q, U, and V, respectively:

$$\begin{aligned} I &= a_{||}^2 + a_{\perp}^2, \\ Q &= a_{||}^2 - a_{\perp}^2, \\ U &= 2a_{||}a_{\perp}\cos(\delta), \\ V &= 2a_{||}a_{\perp}\sin(\delta). \end{aligned} \tag{2.8}$$

In general, Q and U depend on the choice of basis vectors, $\hat{\mathbf{e}}_{||}$ and $\hat{\mathbf{e}}_{\perp}$. The basis vectors may be rotated about the direction of propagation by an angle ψ to yield new basis vectors $\hat{\mathbf{e}}'_{||}$ and $\hat{\mathbf{e}}'_{\perp}$. The corresponding transformation for the Stokes parameters is given by

$$\begin{pmatrix} I' \\ Q' \\ U' \\ V' \end{pmatrix} = \begin{pmatrix} 1 & 0 & 0 & 0 \\ 0 & \cos 2\psi & \sin 2\psi & 0 \\ 0 & -\sin 2\psi & \cos 2\psi & 0 \\ 0 & 0 & 0 & 1 \end{pmatrix} \begin{pmatrix} I \\ Q \\ U \\ V \end{pmatrix}. \tag{2.9}$$

Eq. 2.9 is often used in light scattering models when summing the contributions of multiple scattered rays in a particular scattering plane. The equivalent transformation of the amplitude matrix is discussed in more detail in Section 3.4.4.

2.3 Mueller Matrices

Eq. 2.9 is an example of a 4×4 Mueller matrix (also known as a phase matrix), which describes a transformation of the Stokes parameters. A general phase matrix can be described by

$$\begin{pmatrix} I' \\ Q' \\ U' \\ V' \end{pmatrix} = \begin{pmatrix} S_{11} & S_{12} & S_{13} & S_{14} \\ S_{21} & S_{22} & S_{23} & S_{24} \\ S_{31} & S_{32} & S_{33} & S_{34} \\ S_{41} & S_{42} & S_{43} & S_{44} \end{pmatrix} \begin{pmatrix} I \\ Q \\ U \\ V \end{pmatrix}, \tag{2.10}$$

where, in general, S_{ij} are a function of θ and ϕ [28]. The elements of the Mueller matrix are not entirely independent and can be derived from the amplitude scattering matrix using standard relations (Appendix A) [87]. Some Mueller matrix examples for standard laboratory equipment are given in Table 2.1 [88]. It is straightforward to describe the physical representation of a few of the phase matrix elements S_{ij}. For unpolarised incident light, S_{11} represents the angular distribution of scattered light intensity. When normalised, it is often referred to as the phase function. S_{12}/S_{11} is the degree of linear polarisation, S_{13}/S_{11} the degree of diagonal polarisation, and S_{14}/S_{11} the degree of circular polarisation. The scattered intensity is determined by the first row elements of the phase matrix. While Mueller matrices can in this way describe the scattering effect of simple interactions, they can also be used to describe more complex interactions of light scattering. For instance, when an incident plane wave encounters a particle, the scattering of light depends on the wavelength, particle morphology, and refractive index. Accurately computing the Mueller matrices of different particles is of great importance for many atmospheric applications. In weather and climate models, knowledge of the amount of forward and back-scattering intensity is

of great importance for predicting the Earth-atmosphere radiation balance. In aircraft and satellite-based radiation measurements, knowledge of the Mueller matrix can be useful for instrument calibration and for discerning between different particles.

$\frac{1}{2}\begin{pmatrix} 1 & 1 & 0 & 0 \\ 1 & 1 & 0 & 0 \\ 0 & 0 & 0 & 0 \\ 0 & 0 & 0 & 0 \end{pmatrix}$	$\frac{1}{2}\begin{pmatrix} 1 & -1 & 0 & 0 \\ -1 & 1 & 0 & 0 \\ 0 & 0 & 0 & 0 \\ 0 & 0 & 0 & 0 \end{pmatrix}$
Horizontal linear polariser	Vertical linear polariser
$\begin{pmatrix} 1 & 0 & 0 & 0 \\ 0 & 1 & 0 & 0 \\ 0 & 0 & 0 & -1 \\ 0 & 0 & 1 & 0 \end{pmatrix}$	$\frac{1}{2}\begin{pmatrix} 1 & 0 & 0 & 0 \\ 0 & 1 & 0 & 0 \\ 0 & 0 & 1 & 0 \\ 0 & 0 & 0 & 1 \end{pmatrix}$
Quarter-wave plate	50% Attenuating filter

Table 2.1: Example Mueller matrices for some standard laboratory equipment. Horizontal and vertical linear polarisers only transmit parallel and perpendicular components of the E-field, respectively. A quarter-wave plate transforms an elliptical wave into a linear wave by shifting the relative phase δ by 90° [22]. A 50% attenuating filter has no effect on the polarisation but only transmits half the intensity.

2.4 Scattering Parameters

As mentioned in the previous section, a Mueller matrix is a function of scattering direction. The computation of which, results in a large amount of data that can be cumbersome to use in practice. Therefore, it is common to parametrise the scattering in order to reduce the amount of information needed for application. A summary of key scattering parameters are given in the proceeding subsections. Several integrated scattering parameters are introduced, which have no angular dependence. An example of their application includes global chemistry transport models, wherein they are used to forward model solar and infrared irradiance or flux [89].

2.4.1 Asymmetry Parameter

The asymmetry parameter g, is used to describe the amount of forward or back-scattered light, and is defined by

$$g = \int_0^{\pi} p_{11}(\theta) \cos\theta \; d\theta, \tag{2.11}$$

where the phase function p_{11} is S_{11} normalised over the solid angle, such that

$$p_{11} = \frac{S_{11}}{\int_0^{2\pi}\int_0^{\pi} S_{11}(\theta)\sin\theta \; d\theta d\phi}, \quad \int_0^{2\pi}\int_0^{\pi} p_{11}(\theta)\sin\theta \; d\theta d\phi = 1. \tag{2.12}$$

The asymmetry parameter takes values in the range $-1 < g < 1$. For $g = -1$, all scattered light is in the direction $\theta = -180°$, whereas for $g = +1$, the light is scattered entirely in the direction $\theta = 0°$ [28]. For $g = 0$, light is scattered symmetrically about $\theta = 90°$. It is an integrated scattering parameter, since the integration removes any angular dependence [89].

2.4.2 Scattering, Absorption, & Extinction Cross Sections

The power radiated from the scattering particle in the direction $\hat{\mathbf{r}}$ per unit solid angle, given by

$$\frac{d\sigma}{d\Omega} = \frac{r^2 |\epsilon_{\mathbf{s}}^* \cdot \mathbf{E_s}|^2}{|\epsilon_{\mathbf{i}}^* \cdot \mathbf{E_i}|^2}, \tag{2.13}$$

is called the differential scattering cross section, where

$$\epsilon_{\mathbf{i}} = \frac{\mathbf{E_0^i}}{|\mathbf{E_0^i}|}, \quad \epsilon_{\mathbf{s}} = \frac{\mathbf{E_0^s}}{|\mathbf{E_0^s}|}, \tag{2.14}$$

are called the polarisation vectors [29]. The total scattering cross section is then given by

$$\sigma_{scat} = \int \frac{d\sigma}{d\Omega}\, d\Omega = \int_{4\pi} I^{'}\, d\Omega, \tag{2.15}$$

where $d\Omega$ is the solid angle element $\sin(\theta)\ d\theta d\phi$, and $I^{'}$ is the scattered intensity as defined in Eq. 2.10. The scattering cross section may be physically interpreted as the total area from which incident energy is scattered (into any direction) by the particle. Owing to the combined effects of reflection, transmission, and external diffraction, the scattering cross section is often greater than the geometric cross section of the scatterer. If the particle has a geometrical cross section G, then the scattering efficiency factor is defined as

$$Q_{sca} = \sigma_{scat}/G. \tag{2.16}$$

The scattering efficiency represents the fraction of incident energy scattered by the particle. As the scatterer becomes much larger than the wavelength, the value of $Q_{sca} \to 2$, which is known as the extinction paradox. The amount of energy absorbed by the particle is given by the absorption cross section σ_{abs} and the corresponding absorption efficiency is $Q_{abs} = \sigma_{abs}/G$. For non-absorbing media, these are equal to 0. The total energy removed from the incident beam is called the extinction cross and is given by $\sigma_{ext} = \sigma_{sca} + \sigma_{abs}$. The extinction efficiency is defined analogously by $Q_{ext} = \sigma_{ext}/G$. The scattering, absorption, and extinction cross sections and their efficiencies are integrated scattering parameters.

2.4.3 Single-Scattering Albedo

The single-scattering albedo ω_0 is an integrated scattering parameter defined by

$$\omega_0 = \sigma_{sca}/(\sigma_{abs} + \sigma_{sca}). \tag{2.17}$$

From the law of conservation of energy, the single-scattering albedo take values in the range $0 < \omega_0 < 1$. For non-absorbing particles, $\omega_0 = 1$. In this case, all the extinction of light is due to scattering and therefore such particles are often described as "white", "shiny", "bright", or "reflective" [90]. Particles with extinction dominated by absorption have values of $\omega_0 \to 0$, and equal contributions of scattering and absorption give $\omega_0 = 0.5$. As the real part of the refractive index $\to 1$, the scattering efficiency $\to 0$, since the particle becomes less distinguishable from the surrounding air. In this case, the extinction is dominated by absorption, the denominator in Eq. 2.17 approaches σ_{abs}, and $\omega_0 \to 0$.

2.4.4 Back-Scattering Cross Section

Unlike the previous cross sections, the back-scattering cross section is not integrated over the solid angle. Instead, it takes the value of the differential scattering cross section at $\theta = 180°$. It is an essential parameter in Lidar applications, wherein the Lidar equation is used to relate the power of the returned signal to the emitted power and the range to the target. Higher values of backscattering cross section result in more light being scattered toward the sensor, creating a stronger signal, which must be accounted for in the analysis and filtering of data.

2.4.5 Depolarisation Ratio

The Lidar depolarisation ratio (LDR) δ is defined by

$$\delta = \frac{S_{11}(180°) - S_{22}(180°)}{S_{11}(180°) + S_{22}(180°)}. \tag{2.18}$$

In the Lidar backscatter depolarisation technique, the backscattered light can be used as a remote-sensing tool for the identification of aerosols, water and mixed-phase clouds, cirrus clouds, and for measuring precipitation and phase change [14]. Since most lasers emit polarised light, the depolarisation ratio is easily measured, and different values correspond to the presence of particles with different shapes. Basic theoretical studies for spherical, homogeneous particles predicts no depolarisation for single backscattering. On the other hand, geometric optics theory for hexagonal ice prisms predicts larger depolarisation ratios, with values of $\delta = 0.3$ for thin plates up to $\delta = 0.6$ for long columns. Snowflakes composed of randomly oriented dendritic ice crystals have been measured with $\delta \approx 0.5$, and freezing droplets with accumulating ice on facets can have δ values as high as 0.65. In addition, dust particles from fierce storms and fires have been observed to have δ in the range 0.1–0.2. From this, it can be concluded that the particles are non-spherical, and the lower δ values make them unambiguously distinguishable from ice particles.

Summary

In this chapter, the basic framework for electromagnetic theory has been introduced, which describes how an incident plane wave interacts with a scatterer, leading to a redistribution of the wave's energy into multiple directions. In the next chapter, just a few of the current theoretical light scattering models are introduced, with a particular emphasis on the techniques of GO.

Chapter 3

Theoretical Methods for Electromagnetic Scattering

3.1 Lorenz-Mie Theory

The scattering of a plane wave by a homogeneous sphere of arbitrary radius and refractive index is one of the few cases where Maxwell's equations can be solved in full [28]. The full derivation, developed by Gustav Mie in 1908 [48] is rather involved, so only a brief overview of the key results and where they come from will be given below. For this derivation, the work of van de Hulst is followed [91]. The vector wave equation for a homogeneous medium, given by

$$\nabla^2 \mathbf{A} + k^2 n^2 \mathbf{A} = 0, \tag{3.1}$$

where $k = 2\pi/\lambda$ is the wavenumber, n is the refractive index, and $\mathbf{A}$ is a vector solution, which must be satisfied by the fields inside and outside of the sphere. If ψ is a solution to the scalar wave equation, then it can be proven that the vectors $\mathbf{M}_\psi$ and $\mathbf{N}_\psi$, where

$$\mathbf{M}_\psi = \nabla \times (\mathbf{r}\psi), \tag{3.2}$$

$$nk\mathbf{N}_\psi = \nabla \times \mathbf{M}_\psi, \tag{3.3}$$

satisfy the vector wave equation. In addition, $\mathbf{M}_\psi$ and $\mathbf{N}_\psi$ are related by

$$nk\mathbf{M}_\psi = \nabla \times \mathbf{N}_\psi. \tag{3.4}$$

The scalar solutions u and v and their corresponding vector solutions $\mathbf{M}_u$, $\mathbf{N}_u$, $\mathbf{M}_v$, and $\mathbf{N}_v$ are then introduced. It may be shown that, an incident plane wave propagating along the z-axis, with an E-field polarized along the x-axis, can be defined by choosing u and v such that

$$u = e^{i\omega t} \cos\phi \sum_{m=1}^{\infty} (-i)^m \frac{2m+1}{m(m+1)} P_m^1(\cos\theta) j_m(kr), \tag{3.5}$$

$$v = e^{i\omega t} \sin\phi \sum_{m=1}^{\infty} (-i)^m \frac{2m+1}{m(m+1)} P_m^1(\cos\theta) j_m(kr), \tag{3.6}$$

where $P_m^1(\cos\theta)$ are associated Legendre functions of order 1 and $j_m(kr)$ are modified Bessel functions of the first kind. The outgoing scattered wave is sufficiently described by choosing u and v such that

$$u = e^{i\omega t} \cos\phi \sum_{m=1}^{\infty} -a_m (-i)^m \frac{2m+1}{m(m+1)} P_m^1(\cos\theta) h_m^{(2)}(kr), \tag{3.7}$$

$$v = e^{i\omega t} \sin\phi \sum_{m=1}^{\infty} -b_m (-i)^m \frac{2m+1}{m(m+1)} P_m^1(\cos\theta) h_m^{(2)}(kr), \tag{3.8}$$

where a_m and b_m are coefficients to be fixed and $h_m^{(2)}(kr)$ are modified Bessel functions of the second kind. Similarly, to define the field inside the sphere,

$$u = e^{i\omega t} \cos\phi \sum_{m=1}^{\infty} n c_m (-i)^m \frac{2m+1}{m(m+1)} P_m^1(\cos\theta) j_m(nkr), \tag{3.9}$$

$$v = e^{i\omega t} \sin\phi \sum_{m=1}^{\infty} n d_m (-i)^m \frac{2m+1}{m(m+1)} P_m^1(\cos\theta) j_m(nkr), \tag{3.10}$$

where c_m and d_m are coefficients to be fixed and the argument of the modified Bessel function of the first kind has been adjusted to incorporate the refractive index of the sphere. The coefficients a_m, b_m, c_m, and d_m are fixed by applying boundary conditions. In particular, the tangential components of $\mathbf{E}$ and $\mathbf{H}$ must be conserved across the boundary, as defined by Eq. 2.6. By defining the Riccati-Bessel functions,

$$\psi_m(z) = z j_m(z) = \sqrt{\frac{\pi z}{2}} J_{m+\frac{1}{2}}(z), \tag{3.11}$$

$$\chi_m(z) = -z n_m(z) = -\sqrt{\frac{\pi z}{2}} N_{m+\frac{1}{2}}(z), \tag{3.12}$$

$$\zeta_m(z) = \psi_m(z) + i\chi_m(z), \tag{3.13}$$

where J_m and N_m are Bessel functions of the first and second kind, respectively, the solutions for a_m and b_m are

$$a_m = \frac{\psi_m'(y)\psi_m(x) - n\psi_m(y)\psi_m'(x)}{\psi_m'(y)\zeta_m(x) - n\psi_m(y)\zeta_m'(x)}, \tag{3.14}$$

$$b_m = \frac{n\psi'_m(y)\psi_m(x) - \psi_m(y)\psi'_m(x)}{n\psi'_m(y)\zeta_m(x) - \psi_m(y)\zeta'_m(x)}. \tag{3.15}$$

Here, primes denote derivatives and the arguments x and y are

$$x = \frac{2\pi}{\lambda}, \quad y = nka. \tag{3.16}$$

Finally, if the infinite sums are defined as

$$S_1(\theta) = \sum_{m=1}^{\infty} \frac{2m+1}{m(m+1)} \big(a_m \pi_m \cos\theta + b_m \tau_m \cos\theta\big), \tag{3.17}$$

$$S_2(\theta) = \sum_{m=1}^{\infty} \frac{2m+1}{m(m+1)} \big(b_m \pi_m \cos\theta + a_m \tau_m \cos\theta\big), \tag{3.18}$$

then the resultant field components are given by

$$E_\theta = H_\phi = -\frac{i}{kr} e^{-i(kr+\omega t)} \cos\phi S_2(\theta), \tag{3.19}$$

$$E_\phi = -H_\theta = \frac{i}{kr} e^{-i(kr+\omega t)} \sin\phi S_1(\theta). \tag{3.20}$$

Eqs. 3.19 and 3.20 are exact solutions, which define the resultant fields at all points both inside and outside of the sphere. For computational purposes, one only needs to use Eqs. 3.11–3.20 to arrive at the resultant fields. In practice, m is truncated at some maximum value m_{max}, which limits the numerical accuracy. For spheres with small deformations, it is possible to compute fields using first-order perturbation theory on an inscribed sphere [92]. Improved results have been found using equivolumic spheres, instead [93, 94].

3.2 T-Matrix

Similar to the approach taken in Section 3.1, the T-Matrix method, originally developed by Peter C. Waterman [76], expresses the incident and scattered fields as a sum of vector spherical wave functions. The T-matrix relates the coefficients of the incident to the scattered fields and the matrix elements depend on the material, size, shape, and orientation of the particle. Owing to its analytic nature, the T-matrix can be averaged over all orientations, which speeds up computations for large numbers of randomly oriented particles by several factors of 10 [54]. For this reason, computations involving the T-matrix are efficient and can be used to model scattering from thousands of particles in random orientation [54]. One benefit of the T-matrix method is that it can be applied to nonspherical particles with axial symmetry, unlike Mie theory. One way to compute the T-matrix is the extended boundary condition method. It is based on the vector Huygens principle, which states that the total field outside a bounded surface S containing the scatterer is equal to the sum of the incident

field and an integral over S. Furthermore, for a perfectly conducting particle, as is often assumed, all fields within the particle fall to 0. Therefore, the following relationship can be deduced:

$$\mathbf{E^i}(\mathbf{r}) + \text{integral over S} = \begin{cases} 0, & \text{inside S} \\ \mathbf{E}(\mathbf{r}), & \text{outside S} \end{cases}$$

In other words, the surface currents induced by the incident field generate a scattered field which cancels the incident field inside the particle. One must first expand the surface current and a free-space Green's function into spherical elementary functions with both known and unknown coefficients. By exploiting orthogonality and integrating numerically, the expansion coefficients defining the surface field can be determined. These coefficients can then be used to analytically compute the scattered field. In recent years, the T-matrix method has become a powerful and widespread tool for computing scattered fields from non-spherical particles.

3.3 Discrete Dipole Approximation

The discrete dipole approximation (DDA) was first proposed by Purcell and Pennypacker in 1973 [59]. The DDA provides a flexible approach to computing the scattered field from a particle of arbitrary shape [60]. The DDA method is regarded as a "numerically exact" method, which means that it converges to the true solution with refining discretisation [95]. The accuracy of the DDA method has been well studied, and the error in fulfillment of reciprocity[1] in some tests has been shown to be less than $10^{-5}\%$ [96]. The particle geometry is divided into a grid of point dipoles which interact with each other and the incident field to produce the scattered field. If a self-consistent solution to the dipole polarisations can be found, then the external electric field and hence the scattering properties of the particle can be deduced. In general, one must solve a set of linear, complex equations, which are responsible for the majority of the computational burden of this method.

Purcell and Pennypacker's method uses a simple cubic lattice to contain the particle geometry and places N point dipoles with index $j = 1, ..., N$ attached to lattice vertices. Each dipole has a polarisability α_j, leading to a dipole moment

$$\mathbf{P_j} = \alpha_j \mathbf{E_{ext,j}}, \tag{3.21}$$

where $\mathbf{E_{ext,j}}$ is the external electric field vector at the position of the j^{th} dipole. In general, α_j is a tensor but for isotropic media it may be regarded as a scalar quantity. Eq. 3.21 can be rewritten as a set of N complex vector equations such that

$$\mathbf{P_j} = \alpha_j(\mathbf{E_{inc,j}} - \sum_{k \neq j} \mathbf{A_{jk}}\mathbf{P_k}), \tag{3.22}$$

where the complexity accounts for the phase of the incident field and the summation accounts for interactions between the field of one dipole and another. Each $\mathbf{A_{jk}}$ is a 3 x 3 symmetric

[1] The fulfillment of reciprocity refers to the fact that Maxwell's equations are symmetric with respect to the interchange of the source and observation points [14, 96]. It is a useful check for validating numerical results.

matrix describing the effect of the 3-vector polarisation $\mathbf{P_k}$ on the 3-vector polarisation $\mathbf{P_j}$. The summation term is given (for completeness) by

$$\mathbf{A_{jk}P_k} = \frac{\exp(ikr_{jk})}{r_{jk}^3}\left(k^2\mathbf{r_{jk}} \times (\mathbf{r_{jk}} \times \mathbf{P_k}) + \frac{1-ikr_{jk}}{r_{jk}^2} \times \left[r_{jk}^2\mathbf{P_k} - 3\mathbf{r_{jk}}(\mathbf{r_{jk}} \cdot \mathbf{P_k})\right]\right) \quad (j \neq k), \tag{3.23}$$

where $\mathbf{r_{jk}}$ is the vector from the j^{th} to the k^{th} dipole. Eq. 3.22 describes the polarisation of each dipole. This set of equations may be concatenated into a single matrix equation

$$\tilde{\mathbf{A}}\tilde{\mathbf{P}} = \tilde{\mathbf{E}}_{\mathbf{inc}}, \tag{3.24}$$

where $\tilde{\mathbf{P}}$ and $\tilde{\mathbf{E}}_{\mathbf{inc}}$ have $3N$ elements and $\tilde{\mathbf{A}}$ is a $3N$ x $3N$ matrix which can be inverted to find the dipole polarisations and hence the external field using Eq. 3.21. For matrix inversion, a number of iterative solvers can be found in the Parallel Iterative Methods package [97], which include CG, CGNR, CGNE, BiCG, CGS, BiCGSTAB, QMR, and TFQMR.

3.4 Classical Geometric Optics

3.4.1 Introduction

The previous subsections describe several well-established exact or numerically exact methods for light scattering computations. However, as the particle size, complexity, or refractive index increases, the computational resources required for most methods increases rapidly. For instance, the truncation order of Lorenz-Mie and T-Matrix style approaches can become large, and the set of basis functions used for the spherical wave expansion can become unstable at high orders [14]. DDA computations in 3 dimensions require computational grid sizes that scale with the cubed size of the particle, which can result in impractically large memory requirements. This can lead to slow matrix inversion convergence, and, in the worst case, there may be no convergence [62]. In practice, many problems cannot be solved with exact methods and therefore approximate methods with improved computational efficiency must be used. Geometric optics (GO) is a widespread probing tool in wave propagation problems in the short wavelength limit across many areas of physics. The behaviour of a wave propagating under geometric optics principles is often introduced from Fermat's principle, which states that the path taken by a "ray" between two points is the path that can be travelled in the least time [86]. In many cases, this leads to wave behaviour that can be simplified as travelling along straight line paths. Historically, the use of GO generally has 2 main understandings. On the one hand, it is a method of ray analysis as a means of forming images, which is an approach with applications in optics design, for example. On the other hand, it is method with much wider application as means of wave field approximation. Although the history of empirical studies on geometric optics dates back to over 1000 years ago [98], more recent work has been influenced by the Debye formulation of the problem, which is derived from Maxwells equations [23]. This approach introduces the eikonal as the solution to the wave equation in the limits of geometric optics, ie. under

the assumptions that the amplitude, wavevector, and refractive index do not vary significantly over the wavelength. Its simplicity makes for an appealing and intuitive approach to many areas concerned with wave propagation in physics, including electromagnetism, elastic and sound waves, plasma and liquid dynamics, and quantum mechanics. In this section, an overview of the fundamental concepts of geometric optics in the context of light scattering is given.

3.4.2 Ray Tracing

Ray tracing is a core component of the GO approach. If an initial field distribution is known across a surface, then a ray is the coordinate-space projection of a point on that surface [23]. In practice, the scattering particle is usually represented as a closed surface consisting of many facets, where each facet is a list of coplanar vertices. For a plane wave in homogeneous media, the family of rays emerging from the surface will travel along straight-line paths, which simplifies the wave propagation problem to one of determining the intersections of lines with polygons. To determine the parts of the particle surface which are illuminated by an incident plane wave, straight-line paths are traced along the propagation direction towards the particle. If the ray is found to intersect with a polygon representing one of the particle facets, then it is deduced that that part of the particle surface is illuminated by the incident wave. In order to accurately sample the different paths that can be taken by the wave, ray tracing codes need to trace a huge number of incident rays. To circumvent this, modern codes represent collections of similar rays as beams, and use polygon clipping algorithms to split beams up as they are traced [40, 41]. The method of ray tracing may be split into 2 parts. First, the intersection point of a ray with the unbounded plane of a polygon is found. Second, a check is performed to determine if the intersection point lies within the bounded area of the polygon. A diagram illustrating the method is shown in Figure 3.1.

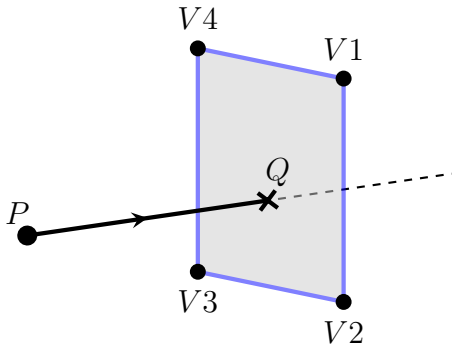

Figure 3.1: Diagram illustrating the ray casting problem. A ray is initialised at point P with a propagation direction $\hat{\mathbf{K}}_\mathbf{0}$. The facet of a particle is represented by a polygon with several vertices. The point Q represents the intersection of the ray with the plane containing the polygon. A check must be performed to determine if Q lies within the bounds of the polygon.

Intersection Point with the Unbounded Plane

The intersection point $\mathbf{r_Q}$ of a ray with the plane containing the polygon is determined using the equation of the plane and the ray equation. The former is given by

$$\hat{\mathbf{N}} \cdot \mathbf{r} = ax + by + cz = d, \tag{3.25}$$

where $\hat{\mathbf{N}} = (a\hat{\mathbf{x}}, b\hat{\mathbf{y}}, c\hat{\mathbf{z}})$ is the unit normal vector to the plane, a, b, c, and d are the plane coefficients, x, y, z are cartesian coordinates, and $\mathbf{r}$ is a the position vector of a point in the plane. The surface normal can be determined by taking the cross product of two edge vectors. For instance, if $\mathbf{F_i}$ is the vector from vertex V_i to vertex V_{i+1}, then the surface normal is given by

$$\hat{\mathbf{N}} = \frac{\mathbf{F_i} \times \mathbf{F_{i+1}}}{|\mathbf{F_i}||\mathbf{F_{i+1}}|}. \tag{3.26}$$

The sign of $\hat{\mathbf{N}}$ is determined by whether a clockwise or anti-clockwise vertex ordering is chosen as viewed externally. The remaining plane coefficient d is then easily found by substituting the position of one of the facet vertices. The ray with propagation direction $\hat{\mathbf{K}}_\mathbf{0}$ can be described by a parametric equation of a line:

$$\mathbf{r}(\tau) = \mathbf{r_P} + \tau\hat{\mathbf{K}}_\mathbf{0}, \tag{3.27}$$

where τ is a parameter representing the distance travelled by the ray from its origin $\mathbf{r_P}$. The distance τ_Q from the ray origin to the intersection with the plane is given by

$$\tau_Q = \frac{(\mathbf{V_i} - \mathbf{r_P}) \cdot \hat{\mathbf{N}}}{\hat{\mathbf{K}}_\mathbf{0} \cdot \hat{\mathbf{N}}}. \tag{3.28}$$

Here, $(\mathbf{V_i} - \mathbf{r_P})$ is the vector from the ray origin to the position vector of any vertex in the facet. A diagram for reference is shown in Figure 3.2. Care must be taken if the propagation direction and plane are coplanar (ie. $\hat{\mathbf{K}}_\mathbf{0} \cdot \hat{\mathbf{N}} = 0$), since in this case the ray will never intersect with the plane and τ_Q is undefined. Once τ_Q is known, it can be substituted into the ray equation (Eq. 3.27) to obtain the position of the intersection point with the plane.

Point-in-Polygon Check

Several methods exist for determining if the point of intersection with the plane lies within a polygon. For example, for polygons with 3 vertices, the intersection point can be projected onto a barycentric coordinate system centered on the triangle. If all components are positive and their sum is less than 1, then the point lies within the triangle. For polygons with more vertices, methods such as computing the winding number [99], or the ray-casting technique exist. The ray-casting technique involves casting a ray lying in the plane from the point of intersection Q. If the ray intersects an odd number of times with the edges of the polygon, then the point lies within the polygon, else, it lies outside the polygon. If the polygon is convex, then a simple approach based on edge normals can be used, which is discussed below.

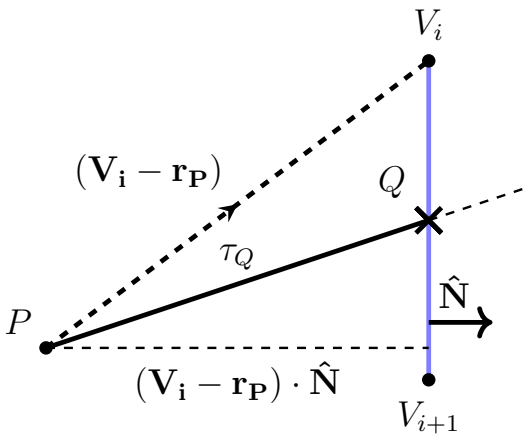

Figure 3.2: Diagram illustrating the geometry for obtaining τ_Q, which describes the distance travelled by the ray from P to the intersection with the plane containing the facet.

The edge normal $\hat{\mathbf{N}}_\mathbf{i}^\mathbf{F}$ is a vector which lies in the plane and is also perpendicular to the edge vector $\hat{\mathbf{F}}_\mathbf{i}$. It is defined by

$$\hat{\mathbf{N}}_\mathbf{i}^\mathbf{F} = \hat{\mathbf{F}}_\mathbf{i} \times \hat{\mathbf{N}}, \tag{3.29}$$

which ensures that it points outwards from the centre of the polygon. For each vertex, the dot product of the edge normal and the vector to the point of intersection can be computed. If the value is positive, then the point of intersection lies outside the edge, whereas if it is negative, it lies inside the edge. If, for all edges, the values of the dot products are negative, then the point lies within the polygon. A diagram for illustration is shown in Figure 3.3. One advantage of this approach is that if one dot product is found to be positive, then no further checks are required and the intersection can be declared outside. However, due to its simplicity it cannot be used for concave polygon shapes. In summary, ray tracing determines the portions of the particle that will be illuminated by an incident plane wave. In the next step, Snell's law is used to determine how the wave is reflected and transmitted at the particle surface.

3.4.3 Snell's Law

To the zeroth-order approximation, geometric optics obeys the principle of locality. This states that the reflected wave at a point on a boundary behaves as if the surface at that point was locally plane [23]. So long as the radius of curvature of the surface is larger than the wavelength, and the phase shift across any surface irregularities is much larger than one, this approximation is valid [91]. When a plane wave encounters a boundary between two dielectric media with different refractive indices, a reflected and a transmitted plane wave are produced. The angle of incidence θ_i may be introduced as the angle made between the incident propagation vector $\hat{\mathbf{K}}_\mathbf{0}$ and the surface normal $\hat{\mathbf{N}}$, where $\theta_i < 90°$. According to the boundary conditions (Eq. 2.6), the tangential component of the electric field is preserved across the boundary. Based on this, many optics texts (eg. [22, 28, 29]) show that the

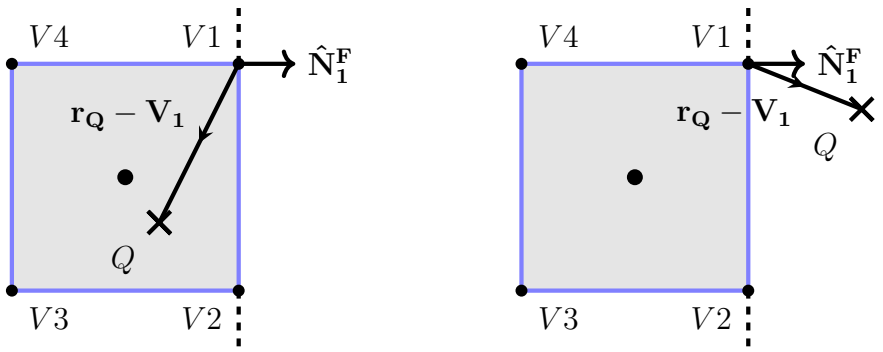

(a) Q lies towards the centroid of the polygon.

(b) Q lies away from the centroid of the polygon.

Figure 3.3: Diagram illustrating how the edge normal method is used to determine if a point-in-plane Q (marked by '$\times$' symbol) lies within a polygon. Annotations are shown for the edge from V_1 to V_2. The unbounded edge is represented by the dashed line. In (a), the dot product $(\mathbf{r_Q} - \mathbf{V_1}) \cdot \hat{\mathbf{N}}_1^{\mathbf{F}}$ is negative. This indicates that Q lies on the inner side of the unbounded edge. In (b) on the other hand, the dot product is positive, indicating that Q lies on the outer side. This check is repeated for all edges of a polygon.

reflected wave is reflected at an angle $\theta_r = \theta_i$. The refracted wave is transmitted at an angle θ_t, which is related to the incident angle θ_i by

$$n_1 \sin\theta_i = n_2 \sin\theta_t, \tag{3.30}$$

where n_1 and n_2 are the real refractive indices of the incidence and transmittance regions, respectively. The corresponding refracted and reflected propagation direction vectors are given by $\hat{\mathbf{K}}'$ and $\hat{\mathbf{K}}''$, respectively. A diagram summarising the reflection and transmission of a plane wave at an interface is shown in Figure 3.4. If $n_2 > n_1$, then there exists an angle of incidence threshold, beyond which no transmitted wave is produced. This angle is known as the critical angle θ_c, and is given by

$$\theta_c = \sin^{-1}\left(\frac{n_1}{n_2}\right). \tag{3.31}$$

The expressions for $\hat{\mathbf{K}}'$ and $\hat{\mathbf{K}}''$ can be derived using a combination of vector triangles and the sine rule as shown in Figure 3.5.

Refracted Propagation Direction

As shown in Figure 3.5b, a vector triangle can be formed such that

$$A\hat{\mathbf{K}}' = B\hat{\mathbf{K}}_\mathbf{0} - C\hat{\mathbf{N}}, \tag{3.32}$$

where A, B, and C are unknown lengths. Using the sine rule, the unknown lengths can be related to the angles of the triangle by

$$\frac{A}{\sin\theta_i'} = \frac{B}{\sin\theta_t} = \frac{C}{\sin\beta}, \tag{3.33}$$

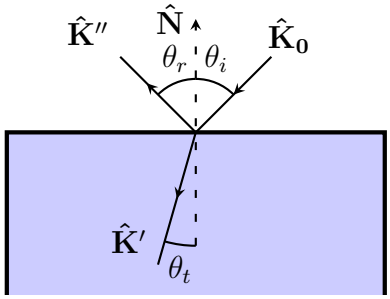

Figure 3.4: Diagram summarising the reflection and transmission of a wave at a dielectric boundary under the principles of GO. The incident wave with propagation vector $\hat{\mathbf{K}}_\mathbf{0}$ is incident at an angle θ_i made with the surface normal. The scattered field is composed of a refracted wave inside the boundary and a reflected wave outside the boundary.

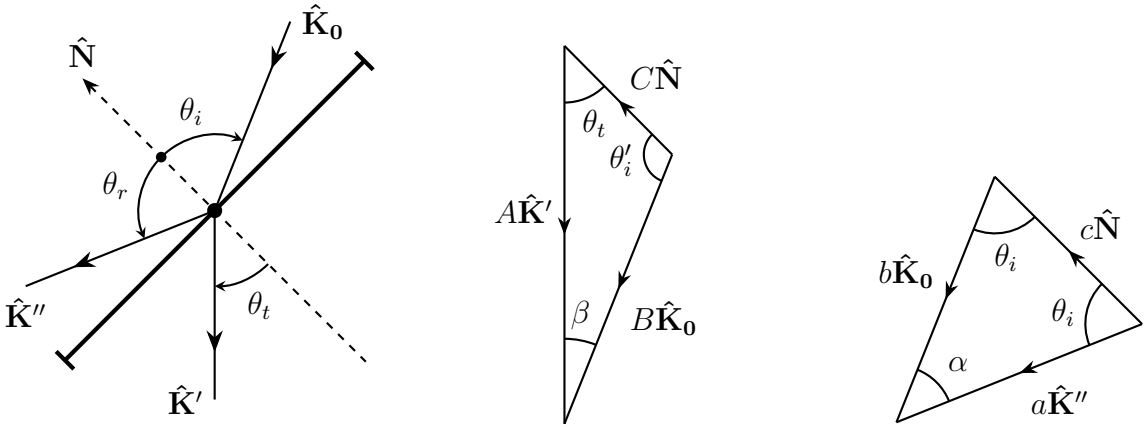

Figure 3.5: a) The geometry of the reflection and refraction at an interface. b) The vector triangle formed between the incident propagation direction, the refracted propagation direction, and the surface normal. c) The vector triangle formed between the incident propagation direction, the reflected propagation direction, and the surface normal.

where $\theta_i' = \pi - \theta_i$, and $\beta = \theta_i - \theta_t$. Substituting Eq. 3.33 into Eq. 3.32 gives

$$A\hat{\mathbf{K}}' = A\frac{\sin\theta_t}{\sin\theta_i'}\hat{\mathbf{K}}_\mathbf{0} - A\frac{\sin(\theta_i - \theta_t)}{\sin\theta_i'}\hat{\mathbf{N}}, \tag{3.34}$$

which may be rewritten as

$$\hat{\mathbf{K}}' = \frac{\sin(\theta_i - \theta_t)}{\sin\theta_i}\hat{\mathbf{N}} - \frac{\sin\theta_t}{\sin\theta_i}\hat{\mathbf{K}}_\mathbf{0}. \tag{3.35}$$

For generality, the angles of incidence and transmission may be rewritten in terms of $\hat{\mathbf{K}}_\mathbf{0}$, $\hat{\mathbf{N}}$, and the refractive indices, n_1 and n_2. The trigonometric addition formula may then be used to expand the bracketed term, which gives

$$\hat{\mathbf{K}}' = \left(\cos\theta_t - \cos\theta_i\frac{\sin\theta_t}{\sin\theta_i}\right)\hat{\mathbf{N}} - \frac{\sin\theta_t}{\sin\theta_i}\hat{\mathbf{K}}_\mathbf{0}. \tag{3.36}$$

Snell's law gives that

$$\frac{\sin\theta_t}{\sin\theta_i} = \frac{n_1}{n_2}, \quad \cos\theta_t = \sqrt{1 - \frac{n_1^2}{n_2^2}\left(1 - \cos^2\theta_i\right)}, \tag{3.37}$$

which allows Eq. 3.36 to be written as

$$\hat{\mathbf{K}}' = \sqrt{1 - \frac{n_1^2}{n_2^2}\left(1 - \cos^2\theta_i\right)}\hat{\mathbf{N}} - \frac{n_1}{n_2}\left(\cos\theta_i\hat{\mathbf{N}} + \hat{\mathbf{K}}_\mathbf{0}\right). \tag{3.38}$$

Finally, since $\cos\theta_i = -\hat{\mathbf{K}}_\mathbf{0}\cdot\hat{\mathbf{N}}$, this can be rewritten as

$$\hat{\mathbf{K}}' = \sqrt{1 - \frac{n_1^2}{n_2^2}\left[1 - (\hat{\mathbf{K}}_\mathbf{0}\cdot\hat{\mathbf{N}})^2\right]}\hat{\mathbf{N}} - \frac{n_1}{n_2}\left[\hat{\mathbf{K}}_\mathbf{0} - (\hat{\mathbf{K}}_\mathbf{0}\cdot\hat{\mathbf{N}})\hat{\mathbf{N}}\right]. \tag{3.39}$$

Reflected Propagation Direction

As shown in Figure 3.5c, a vector triangle can be formed such that

$$a\hat{\mathbf{K}}'' = b\hat{\mathbf{K}}_\mathbf{0} + c\hat{\mathbf{N}}, \tag{3.40}$$

where a, b, and c are unknown lengths. Using the sine rule, the unknown lengths can be related to the angles of the triangle by

$$\frac{a}{\sin\theta_i} = \frac{b}{\sin\theta_i} = \frac{c}{\sin\alpha}, \tag{3.41}$$

where $\alpha = \pi - 2\theta_i$. Substituting Eq. 3.41 into Eq. 3.40 gives

$$a\hat{\mathbf{K}}'' = a\hat{\mathbf{K}}_\mathbf{0} + a\frac{\sin(\pi - 2\theta_i)}{\sin\theta_i}\hat{\mathbf{N}}, \tag{3.42}$$

which may be rewritten as

$$\hat{\mathbf{K}}'' = \hat{\mathbf{K}}_\mathbf{0} + \frac{\sin(\pi - 2\theta_i)}{\sin\theta_i}\hat{\mathbf{N}}. \tag{3.43}$$

Using the trigonometric addition formula to expand the bracketed term, this simplifies to

$$\hat{\mathbf{K}}'' = \hat{\mathbf{K}}_\mathbf{0} + 2\cos\theta_i\hat{\mathbf{N}}. \tag{3.44}$$

Finally, since $\cos\theta_i = -\hat{\mathbf{K}}_\mathbf{0} \cdot \hat{\mathbf{N}}$, this may also be rewritten as

$$\hat{\mathbf{K}}'' = \hat{\mathbf{K}}_\mathbf{0} - 2(\hat{\mathbf{K}}_\mathbf{0} \cdot \hat{\mathbf{N}})\hat{\mathbf{N}}. \tag{3.45}$$

Absorbing Media

If the wave is transmitted into a conducting medium, then n_2 becomes complex. In this case, Eq. 3.30 still holds, but θ_t also becomes complex and therefore does not simply represent the angle of transmission. An inhomogeneous wave is produced [86, 100], with planes of constant phase perpendicular to $\hat{\mathbf{K}}'$, but with planes of constant amplitude perpendicular to $\hat{\mathbf{N}}$.

3.4.4 Rotation Matrices

As discussed in the previous subsection, when a plane wave encounters a boundary between two media, a reflected and a transmitted wave are produced. The propagation vectors of which, lie in the plane of incidence, which contains the incident propagation vector and the local surface normal. In general, this plane differs from the reference plane with which the components of the incident field are defined. In order to account for changes in the amplitude and phase due to reflection and transmission, the electric field must first be represented in terms of components parallel and perpendicular to the plane of incidence. Figure 3.6 shows the propagation direction of the incoming plane wave in black, with electric field components defined parallel and perpendicular to the old (i) plane (blue). The local surface normal is shown in grey. The new (s) plane of reference is shown in red; it contains the incident propagation and the local surface normal. By rotating about the incident propagation direction, the electric field components in the new plane are related to those in the old plane by

$$\begin{pmatrix} E_{||} \\ E_\perp \end{pmatrix}^s = \begin{pmatrix} \hat{\mathbf{e}}^i_\perp \cdot \hat{\mathbf{e}}^s_\perp & -\hat{\mathbf{e}}^s_\perp \cdot (\hat{\mathbf{K}}_\mathbf{0} \times \hat{\mathbf{e}}^i_\perp) \\ \hat{\mathbf{e}}^s_\perp \cdot (\hat{\mathbf{K}}_\mathbf{0} \times \hat{\mathbf{e}}^i_\perp) & \hat{\mathbf{e}}^i_\perp \cdot \hat{\mathbf{e}}^s_\perp \end{pmatrix} \begin{pmatrix} E_{||} \\ E_\perp \end{pmatrix}^i, \tag{3.46}$$

where $\hat{\mathbf{e}}^i_\perp$ and $\hat{\mathbf{e}}^s_\perp$ are unit vectors perpendicular to the old and new reference planes, respectively [87, 101]. Using the relation for a plane wave, $\hat{\mathbf{e}}^i_\perp \times \hat{\mathbf{K}}_\mathbf{0} = \hat{\mathbf{e}}^i_{||}$, this can be rewritten as

$$\begin{pmatrix} E_{||} \\ E_\perp \end{pmatrix}^s = \begin{pmatrix} \hat{\mathbf{e}}^i_\perp \cdot \hat{\mathbf{e}}^s_\perp & \hat{\mathbf{e}}^i_{||} \cdot \hat{\mathbf{e}}^s_\perp \\ -\hat{\mathbf{e}}^i_{||} \cdot \hat{\mathbf{e}}^s_\perp & \hat{\mathbf{e}}^i_\perp \cdot \hat{\mathbf{e}}^s_\perp \end{pmatrix} \begin{pmatrix} E_{||} \\ E_\perp \end{pmatrix}^i. \tag{3.47}$$

The diagonal elements in the matrix of Eq. 3.47 represent the cosines of the angle between the two planes (shown as θ in Figure 3.6), and off-diagonal elements represent the sine of the angle between the two planes, with the appropriate sign.

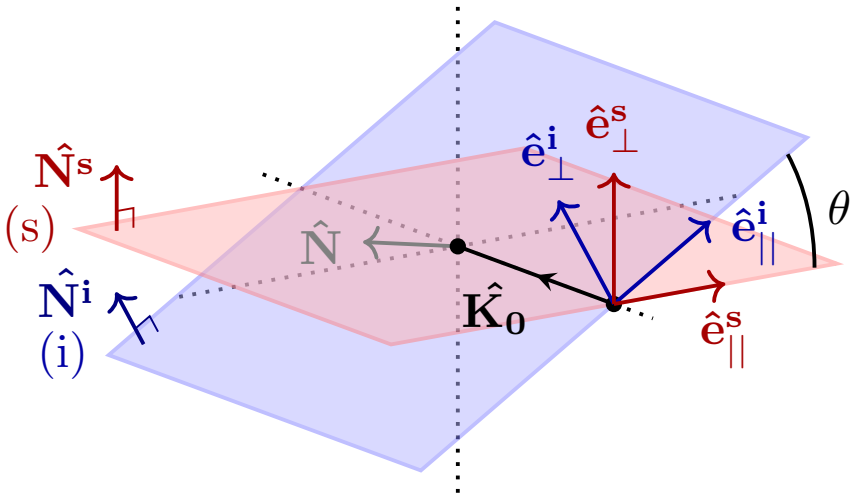

Figure 3.6: Diagram summarising the geometry of the rotation matrix, which is used to rotate the electric field components from the old (blue) to the new (red) reference plane, which contains both the incident propagation vector and the local surface normal.

3.4.5 Fresnel Coefficients of Reflection & Refraction

Once the electric field has been represented in terms of components parallel and perpendicular to the new plane of incidence, the complex amplitude of the reflected and transmitted waves can be obtained from the Fresnel coefficients of reflection and transmission. They are derived using the boundary conditions (eg. Eq. 2.6) and their derivation can be found in many optics textbooks, such as in [22]. They are given by

$$\begin{aligned} r_{||} &= \frac{n_2 \cos\theta_i - n_1 \cos\theta_t}{n_1 \cos\theta_t + n_2 \cos\theta_i}, \quad & r_{\perp} &= \frac{n_1 \cos\theta_i - n_2 \cos\theta_t}{n_1 \cos\theta_i + n_2 \cos\theta_t}, \\ t_{||} &= \frac{2n_1 \cos\theta_i}{n_1 \cos\theta_t + n_2 \cos\theta_i}, \quad & t_{\perp} &= \frac{2n_1 \cos\theta_i}{n_1 \cos\theta_i + n_2 \cos\theta_t}, \end{aligned} \tag{3.48}$$

where $r = E_0^r/E_0^i$ and $t = E_0^t/E_0^i$ are the Fresnel amplitude coefficients of reflection and transmission, respectively. They are complex, in general, which accommodates phase changes at the boundary. For example, a wave undergoing reflection in a medium $n_1 < n_2$ undergoes a phase change of π. For a linearly polarised wave incident upon an inhomogeneous medium, there may be a phase difference between $t_{||}$ and $t_{\perp}$, such that the transmitted wave becomes elliptically polarised [86].

3.4.6 External Diffraction

When a light wave encounters an obstacle with a geometric cross sectional area G, the total amount of extinction generally asymptotes towards twice this value. This is known as the extinction paradox [28]. One half of this contribution is accounted for by the rays directly incident upon the particle. The other half may be attributed to the parts of the wave which pass close to the edges of the particle. Here, the refractive index varies on a length scale smaller than the wavelength and therefore the assumptions of geometric optics

are abandoned[2]. To accommodate for the diffraction of light passing close to the edges of a particle, most classical geometric optics methods utilise some combination of Fraunhofer diffraction and Babinet's principle. A brief summary of these techniques is given below.

Fraunhofer Diffraction

The origin for the theory of Fraunhofer diffraction comes from the work of Kirchhoff, who was the first to attempt to derive the work of Huygens, Young, and Fresnel on diffraction from first principles [29]. The general approach consists of separating the optical domain into 2 regions. The first region contains all sources of radiation and the second is free of sources and bounded by a surface at infinity. The possible diffraction geometries are shown in Figure 3.7. In either case, the sources are present in region I and bounded by some surface $S1$. The point of observation is located somewhere in region II, which is between $S1$ and the surface $S2$ at infinity. The equivalence theorem then states that, the electric field at any point in the second region can be computed by an integral over the first region. In this section, the surface integral type is discussed, although the volume integral type is often used in current methods; for instance, the discrete dipole approximation is based on the volume integral method [95]. One type of surface integral that can be used is the vector Kirchhoff integral, which is given by [29]

$$\mathbf{E}(\mathbf{x}) = \frac{1}{2\pi}\nabla \times \int_{S1} (\mathbf{n} \times \mathbf{E}(\mathbf{x}'))\frac{e^{ik_0 R}}{R} da', \tag{3.49}$$

where $\mathbf{x}$ is the point of observation, $\mathbf{n}$ is the outward-facing normal on $S1$, $\mathbf{R} = \mathbf{x} - \mathbf{x}'$, and $\mathbf{E}(\mathbf{x}')$ is the electric field on $S1$. If the distance to the point of observation $r >> d$, where d is the "size" of the diffracting system, then it is useful to expand the phase exponent:

$$k_0 R = k_0 r - k_0 \frac{\mathbf{x}\cdot\mathbf{x}'}{r} + \frac{k_0}{2r}\left[r'^2 - \left(\frac{\mathbf{x}\cdot\mathbf{x}'}{r}\right)^2\right] + \dots \tag{3.50}$$

If quadratic terms and higher are neglected, the approximation is known as the Fraunhofer limit:

$$\mathbf{E}(\mathbf{x}) = \frac{ie^{ik_0 r}}{2\pi r}\mathbf{k} \times \int_{S1} \mathbf{n} \times \mathbf{E}(\mathbf{x}')e^{-i\mathbf{k}\cdot\mathbf{x}'} da', \tag{3.51}$$

where $\mathbf{k} = k_0(\mathbf{x}/r)$. Since $\mathbf{E}(\mathbf{x}')$ is usually not known beforehand, most applications impose the Kirchhoff approximation, which approximates its value as that of the incident field. For example, consider a plane wave incident at an angle α on a circular aperture of radius a in an opaque screen. The aperture is located in the xy plane, and the plane wave incident from the region $z < 0$ is located in the xz plane as shown in Figure 3.8a. If the wave is polarised parallel to the incidence plane, then the incident field is given by

$$\mathbf{E}^i = E_0(\cos\alpha\ \hat{\mathbf{x}} - \sin\alpha\ \hat{\mathbf{z}})e^{ik_0(z\cos\alpha + x\sin\alpha)}. \tag{3.52}$$

[2]Of course, this argument could be made for rays close to the edge but which lie within the geometric cross section. An extension to accommodate this effect is used in the ray tracing with diffraction on facets method [38].

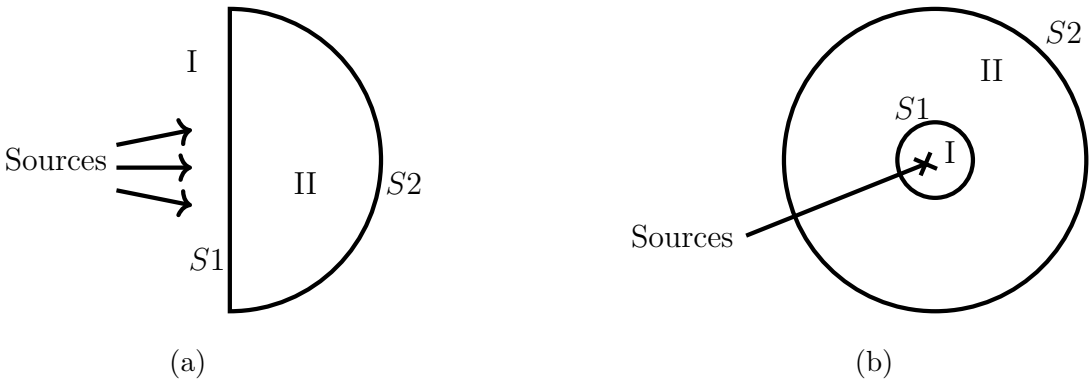

Figure 3.7: Possible geometric setups for dividing the optical domain into 2 regions.

In this case, $\mathbf{n} \times \mathbf{E}(\mathbf{x}') = E_0 \cos\alpha \; e^{ik_0 x' \sin\alpha} \; \hat{\mathbf{y}}$ on the aperture at $S1$. Substituting into Eq. 3.51, the integral can then be integrated analytically in plane polar coordinates, which gives

$$\mathbf{E}(\mathbf{x}) = \frac{ie^{ik_0 r}}{r} a^2 E_0 \cos\alpha (\mathbf{k} \times \hat{\mathbf{y}}) \frac{J_1(ka\zeta)}{ka\zeta}, \tag{3.53}$$

where J_1 is a Bessel function of the first kind and ζ is an angular function defined by

$$\zeta = \sqrt{\sin^2\theta + \sin^2\alpha - 2\sin\theta\sin\alpha\cos\phi}. \tag{3.54}$$

The total far-field intensity is shown in Figure 3.8d. The diffracted pattern is almost circularly symmetric, corresponding to the Airy disk pattern and arises mathematically from the Bessel function in Eq. 3.53. The lack of perfect symmetry arises from the fact that the incident field is x-polarised. By comparing, Figures 3.8b and 3.8c, it can be seen that the in-plane component has greater intensity than the out-of-plane component. In fact, the field component along the $\hat{\mathbf{y}}$-axis is 0 everywhere, which means that polarisation of the incident light is preserved. The S_{12} element of the Mueller matrix is therefore equal to 0 and $S_{11} = S_{22}$.

Babinet's Principle

The previous subsection discussed the effects of a plane wave diffracted through an aperture. It is common practice to combine this theory with Babinet's principle of complementary screens in order to account for the extinction of light which is not directly incident upon, but passes close by to the geometric cross section of a scattering particle. This is known as the external diffraction contribution to the scattered field. The idea of Babinet's principle can be formulated by proposing a screen S containing some apertures. The complementary screen is then defined as the same screen but with opaque sections replaced by apertures and apertures replaced by opaque sections. Babinet's principle then states that the diffracted field is the same for both the original and the complementary screen but with a phase shift of 180° [22]. A diagram illustrating this for a square aperture and its complement is shown in Figure 3.9. In the context of GO, either the up-facing facets [47], or the projected geometric cross section may be used as the opaque sections of the screen. The complementary screen

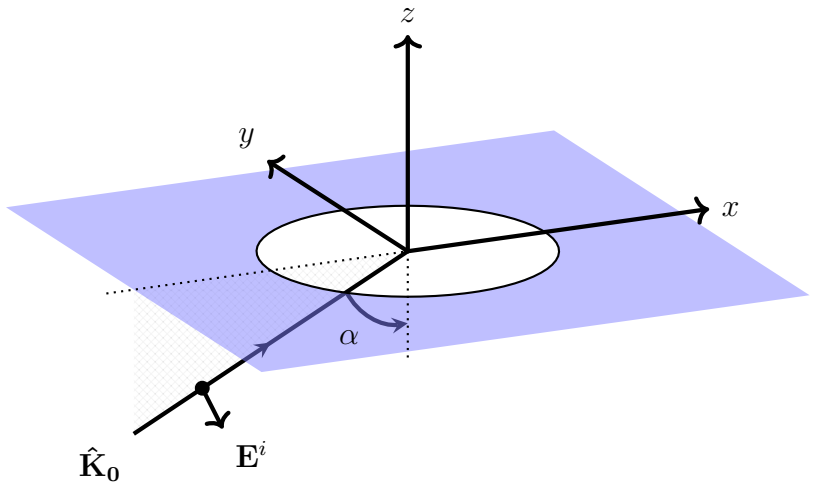

(a)

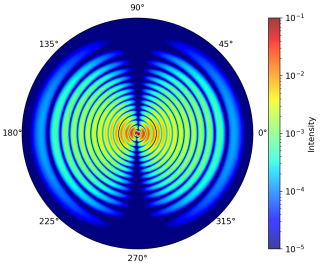

(b) Intensity due to in-plane electric field component.

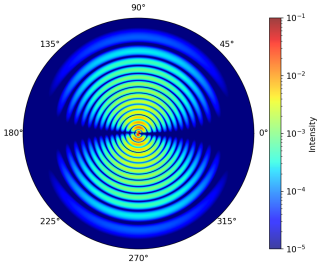

(c) Intensity due to out-of-plane electric field component.

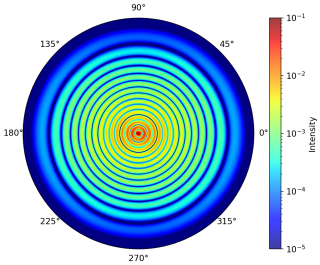

(d) Total intensity.

Figure 3.8: a) Diffraction of a parallel-polarised plane wave at a circular aperture. b-d) Forward-scattered intensity of a parallel-polarised plane wave diffracted at a circular aperture with $\alpha = 0°$, $\lambda = 0.532$, $a = 4$, $E_0 = 1$. The centre of the plot corresponds to $\theta = 0°$, $\hat{\mathbf{z}}$, with increasing values of θ moving radially outwards. The polar angle of the plot represents the azimuthal scattering angle ϕ, with $\hat{\mathbf{x}}$ and $\hat{\mathbf{y}}$ corresponding to $\phi = 0°$ and $\phi = 90°$, respectively.

replaces these sections with apertures and the external diffraction is computed by diffraction of the incident field through each aperture.

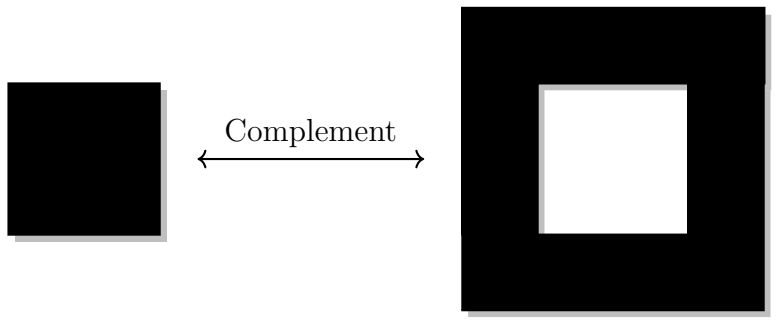

Figure 3.9: An example illustrating Babinet's principle, which states that the diffracted field between an aperture and its complement are the same, except for a phase shift of 180°.

Summary

In this chapter, a brief overview of the many current theoretical methods for light scattering has been given. This includes a detailed discussion on the principles of classical GO, which are leveraged in the novel method of this work, the Parent Beam Tracer method, in the next chapter.

Chapter 4

Parent Beam Tracer Method

4.1 Overview

The Parent Beam Tracer (PBT) method [102] is a physical-optics hybrid method for directly modelling light scattering by non-spherical, large particles with complex shapes, including those with surface roughness. The scattered field is computed in 2 main steps. First, the near-field on the particle surface is approximated using principles of GO. Improved accuracy is achieved by computing the propagation direction of waves in the near-field zone based on macroscopic features of the particle shape. A novel ray backtracing algorithm is used to attain computational stability for highly complex particle shapes. Second, a surface integral diffraction equation [103] combined with the equivalence theorem [101] is used to map from the near-field on the particle surface to the far-field, where the Mueller matrix and integrated scattering parameters are obtained.

4.2 Near-Field Computation

Macroscopic Particle Features

In a preliminary study, the internal fields of a smooth and a rough compact hexagonal column with refractive index 1.31 + 0i at fixed orientation were compared. The particles were assumed to be homogeneous, dielectric, and isotropic. The internal fields were computed using the discrete dipole approximation (DDA) [62], of which the accuracy has been well studied [104]. The columns were chosen to have hexagonal edge length 2.5 µm and prism length 5 µm, with an incident wavelength of 0.5236 µm. Gaussian random roughness was used for the rough column according to the method given by Collier et. al [74]. A correlation length of 0.25 µm and standard deviation 0.05 µm were chosen to yield a mesoscale roughness without excessive deformation of the overall particle shape. The particles were illuminated with an x-polarised plane wave at normal incidence on one of the basal facets. The computed internal field x-component is shown in Figure 4.1. A propagating mode resembling a plane wave is observed, which justifies the use of GO in the near-field zone. Upon visual inspection, it was found that the internal field behaviour was almost identical for both the smooth and rough columns. This led to the idea that, accurate results in a physical-optics hybrid

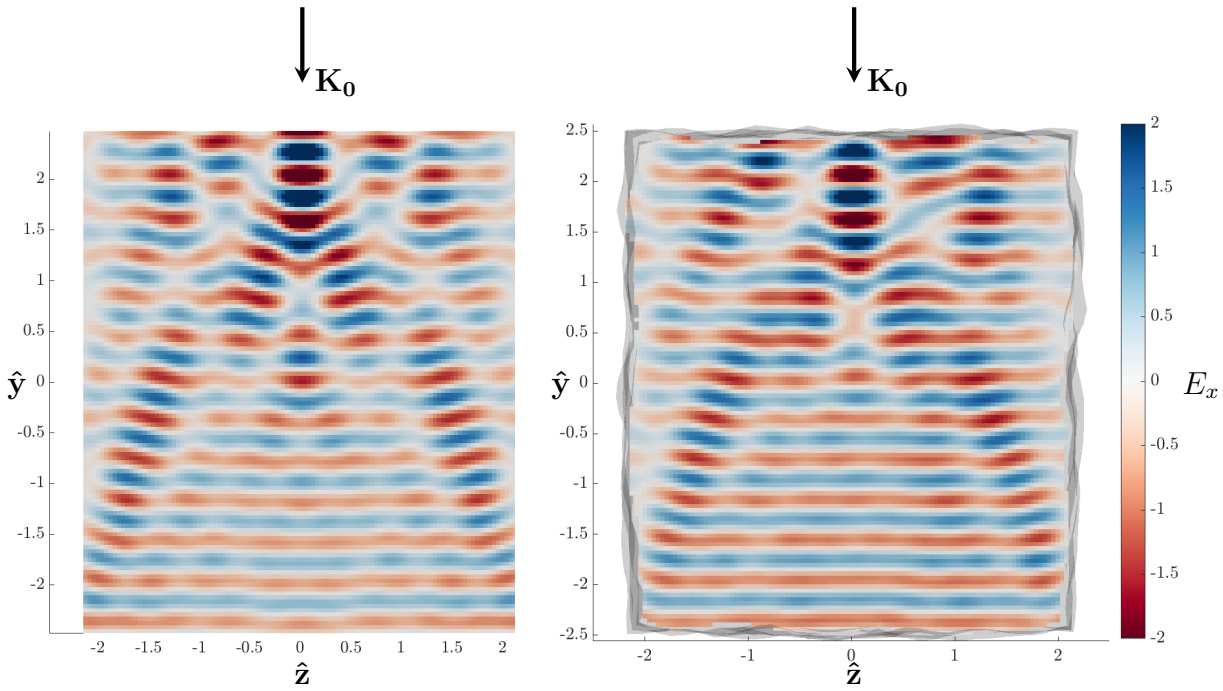

Figure 4.1: Internal field x-component for x-polarised normally incident light of wavelength 0.5236 µm for smooth (left) and rough (right) hexagonal columns with aspect ratio 1. Computed with the discrete dipole approximation [62].

method could be achieved by modelling internally propagating beams as originating from the macroscopic structures of the surface, rather than from individual facets of the mesh. To be more specific, the reflected and refracted propagation direction of beams in the near-field can be computed using macroscopic properties of the particle surface. In this way, the limitations of classical GO when applied to surfaces with features smaller than the wavelength can be mitigated. Based on this proposal, a parent structure is defined within the framework of the PBT as a collection of facets which, when illuminated by a plane wave, produce one reflected (and possibly one refracted) wave with a single propagation direction in the near-field. For the case of smooth surfaces with dimension $d >> \lambda$, this approach simplifies to methods that have already been effectively implemented in many successful physical-optics hybrid methods [101, 105, 106]. In order to define the parent structures of the surface, the following method is proposed:

1. First, a smooth particle geometry is constructed as shown in Figure 4.2a. Each of the facets represents a parent and should be of dimension much larger than the wavelength to permit the use of GO.

2. Second, each parent facet may then be subdivided into a mesh, where each element of the mesh is a facet assigned to the parent. This is shown in Figure 4.2b.

3. Third, the vertices of the mesh may be displaced according to the desired surface texture, as shown in Figure 4.2c.

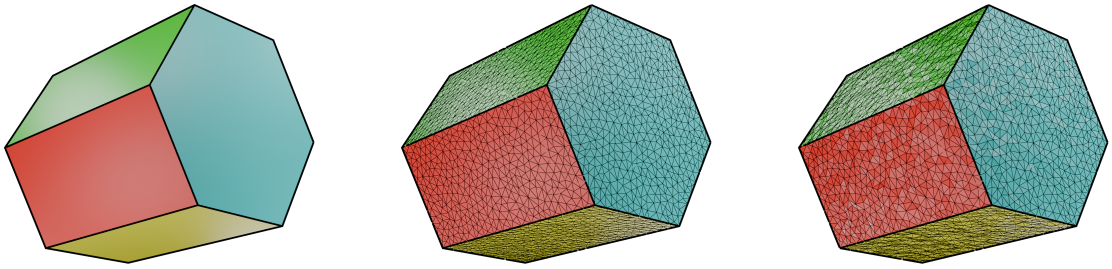

(a) Original, smooth. (b) Meshed, smooth. (c) Meshed, with surface roughness.

Figure 4.2: Sequence of steps showing the proposed method for constructing the parent structures, which are represented by different colours.

It may also be possible to define the parent structures in the opposite direction by starting with a complex-shaped particle mesh and using a mesh simplification algorithm, such as described in [107], to arrive at a simplified mesh representing the parents. However, this approach has not yet been investigated. The surface normal of a parent $\hat{\mathbf{N}}$ is computed as the normalised average of all facet normals $\hat{\mathbf{n}}$ that belong to it. The angle of incidence θ_i between $\hat{\mathbf{N}}$ and the incident propagation direction $\hat{\mathbf{K}}_\mathbf{0}$ is combined with Snell's law to calculate a refracted propagation vector $\hat{\mathbf{K}}'$ at a transmitted angle θ_t and a reflected propagation vector $\hat{\mathbf{K}}''$, which is illustrated in Figure 4.3a. In essence, mesoscopic features of the particle surface are designed to have little effect on the propagation direction of waves in the near-field. However, they have a significant effect on the phase during the near-field beam tracing (Section 4.2), and the far-field mapping (Section 4.3).

Beam Tracing

A novel beam tracing algorithm is employed in order to attain stability and computational efficiency during the near-field computation for highly complex particle surfaces that can exceed 10^4 facets. In the following method, the notation f^i is used to represent the i^{th} facet of the surface mesh, with $i = \{1, 2, \ldots, N_f\}$, where N_f represents the total number of facets. The amplitude matrix of near-field beams as a function of position are represented by an amplitude matrix at each of the illuminated facets on the particle surface. The amplitude scattering matrix at f^i is denoted by $\mathbf{S^i}$. When a part of the particle surface is illuminated by an incident wave, the amplitude matrix at each facet of the surface is computed. For each illuminated parent structure, a new reflected and refracted beam is produced. In general, this leads to several beams which are propagated in a recursive process. Apart from the initial illumination by an external plane wave, the propagation of a beam can be represented by a list of *source* facets from which the beam originates, and a list of *sink* facets where the beam terminates. The notation ${}^{l}_{m}f^{j}$ is used to represent the j^{th} sink facet in the particle mesh illuminated by a source facet f^k in the l^{th} beam of the m^{th} recursion. A visual representation of this is shown in Figure 4.3b. For clarity, the prescript notation will be temporarily omitted but reintroduced later for completeness. The general goal here is to determine a mapping which connects the amplitude matrix at each of the source facets to each of the

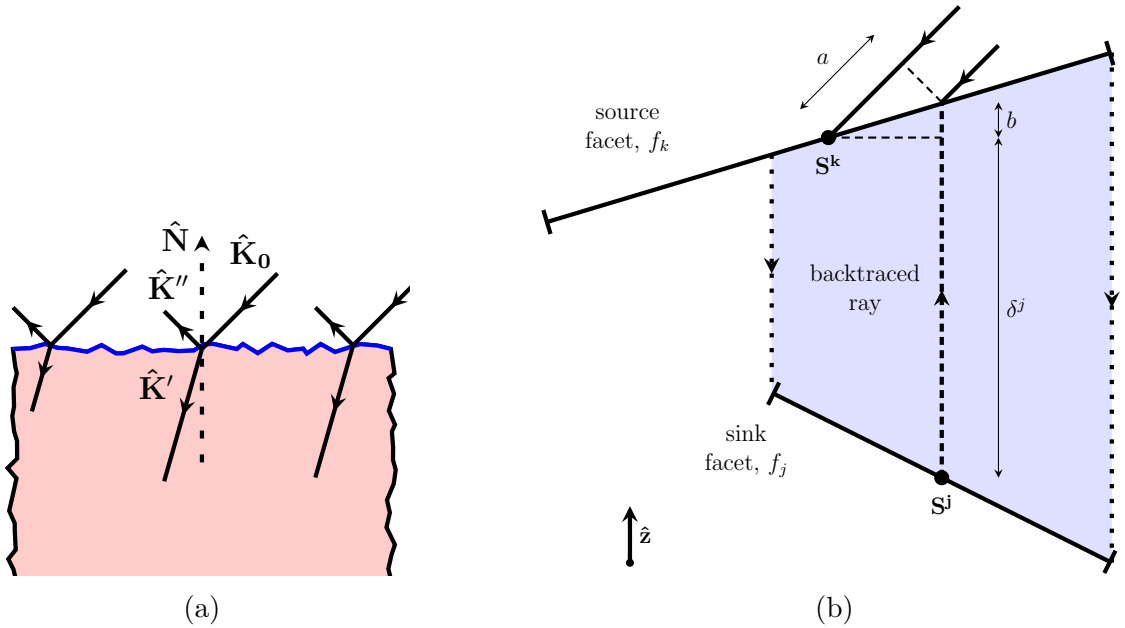

Figure 4.3: a) The average normal of a parent structure (blue) is used to compute a reflected and refracted direction of propagation for rays incident the facets assigned to it. Hence, all the reflected and refracted rays from this surface remain parallel. b) Beam propagation from a source facet f^k to a sink facet f^j. Facet centroids are represented by black dots. A ray is backtraced from the centroid of f^j and is found to intersect within the bounded cross section of f^k. Edges of the beam are represented by dotted lines. It can be shown that $n_1 a = n_2 b$, and therefore δ^j describes the path length between the centroid of f^k and f^j. The corresponding phase difference relates $\mathbf{S^k}$ to $\mathbf{S^j}$.

sink facets. To obtain the mapping, a novel ray backtracing algorithm is used in this work for maintaining stability when working with geometries with large numbers of facets. For each beam emitted from a parent structure, the coordinate system is rotated such that the propagation direction lies along the $-\hat{\mathbf{z}}$ axis. Since there is only one propagation direction, rays may be "backtraced" as an auxiliary measure from the centroid of each facet f^i along the reversed direction, which in this case is the $+\hat{\mathbf{z}}$ axis. If the backtraced ray intersects within the bounded cross section of a facet that was not part the source (ie. not in the set of values f^k), then f^i is determined to be not illuminated. If the backtraced ray intersects within the bounded cross section of a source facet, then f^i is appended to the list of sink facets. The process is shown in Figure 4.4, whereby rays are backtraced upwards to determine if they intersect with the illuminating parent. A flow diagram summary of the algorithm is shown in Figure 4.5. It should be noted that the particle mesh should be sufficiently discretised in order to conserve energy. For particles with surface roughness, oblique incidence can be difficult to model with GO. In this scenario, the effect of small bumps in the surface geometry is magnified, which can cause small peaks in the surface geometry to produce large occluded shadow regions. This is problematic because GO assumes a coherent plane wave, which is no longer satisfied. Furthermore, GO predicts total internal reflection for very oblique incidence and therefore careful modelling of these cases is important for maintaining conservation of energy. To circumvent this, some rays are allowed to artificially pass through facets which belong to the same parent. In this way, beams at oblique incidence are allowed to glide over the bumps of a rough surface. An example of this is shown in the upper left of Figure 4.4.

As described in Section 3.4.3, for incidence $\hat{\mathbf{K}}_\mathbf{0}$ in a medium with refractive index n_1, the refracted beam propagation direction $\hat{\mathbf{K}}'$ in a medium with refractive index n_2 is given by

$$\hat{\mathbf{K}}' = \frac{\sin(\theta_i - \theta_t)}{\sin\theta_i}\hat{\mathbf{N}} - \frac{\sin\theta_t}{\sin\theta_i}\hat{\mathbf{K}}_\mathbf{0}, \tag{4.1}$$

and the reflected beam propagation direction $\hat{\mathbf{K}}''$ is given by

$$\hat{\mathbf{K}}'' = \hat{\mathbf{K}}_\mathbf{0} + 2\cos\theta_i\hat{\mathbf{N}}, \tag{4.2}$$

where $\hat{\mathbf{N}}$ is assumed to point towards $\hat{\mathbf{K}}_\mathbf{0}$. If the angle of incidence is greater than the critical angle, no refracted beam is produced. At each recursion, a beam is propagated in the $-\hat{\mathbf{z}}$ direction from the source along the path of each backtraced ray. For each reflection and refraction process, the amplitude matrix at f^j is computed in a 3-step process:

1. First, for each sink facet f^j, the distance along the $\hat{\mathbf{z}}-$axis from its centroid to the centroid of the corresponding source facet f^k is used as the path length δ^j of the backtraced ray. Only this distance and the amplitude matrix at the source facet is needed to compute the amplitude matrix at the sink facet, which is a corollary of Snell's law (Appendix B). The amplitude matrices are simply related by a phase factor $\exp(ik_0 n\delta^j)$.

2. Second, for each beam, the angle of incidence θ_i^j and refractive indices are used to compute the Fresnel matrix. At f^j, the Fresnel reflection matrix $\mathbf{F}_\mathbf{R}^\mathbf{j}$ and Fresnel

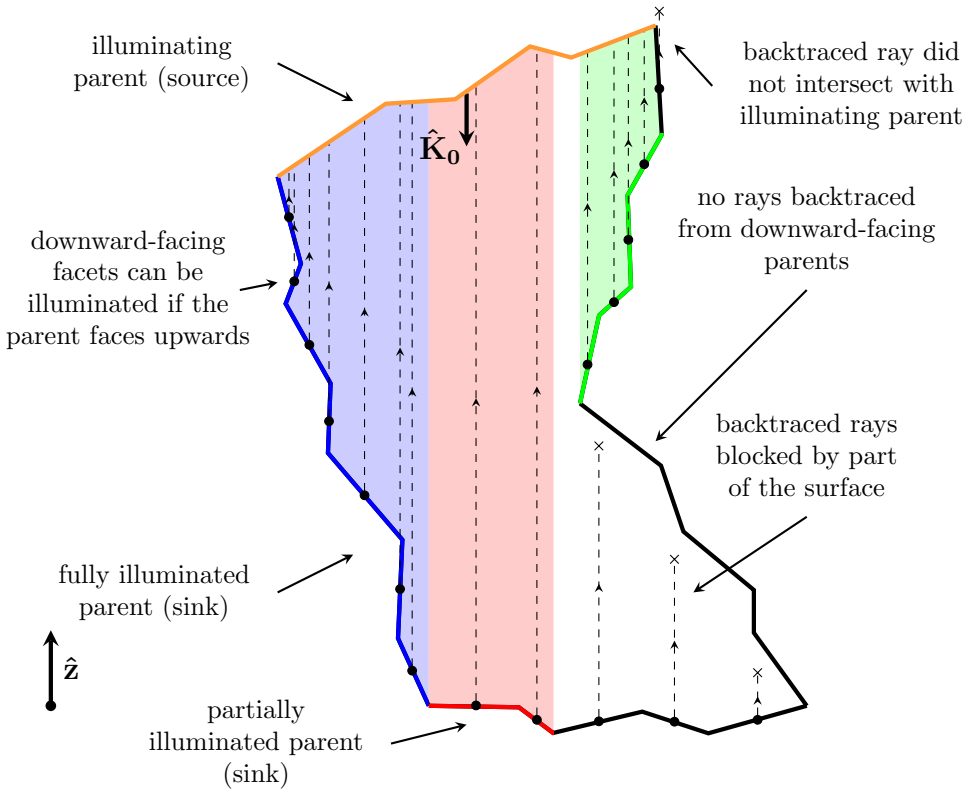

Figure 4.4: Visual representation of the ray backtracing algorithm. A beam is emitted along the $-\hat{\mathbf{z}}$ direction from the source facets f^k in the illuminating parent. Rays are then backtraced along the $\hat{\mathbf{z}}$ direction from the centroids of all other facets f^i that belong to upward-facing parents. Unobstructed rays that successfully intersect with the illuminating parent determine the paths along which the beam should propagate. Rays are deliberately allowed to pass through facets of the same parent from which the ray was emitted, which improves accuracy for oblique reflection. Different colours represent collections of rays associated with a particular parent. The scale of surface roughness is exaggerated for clarity.

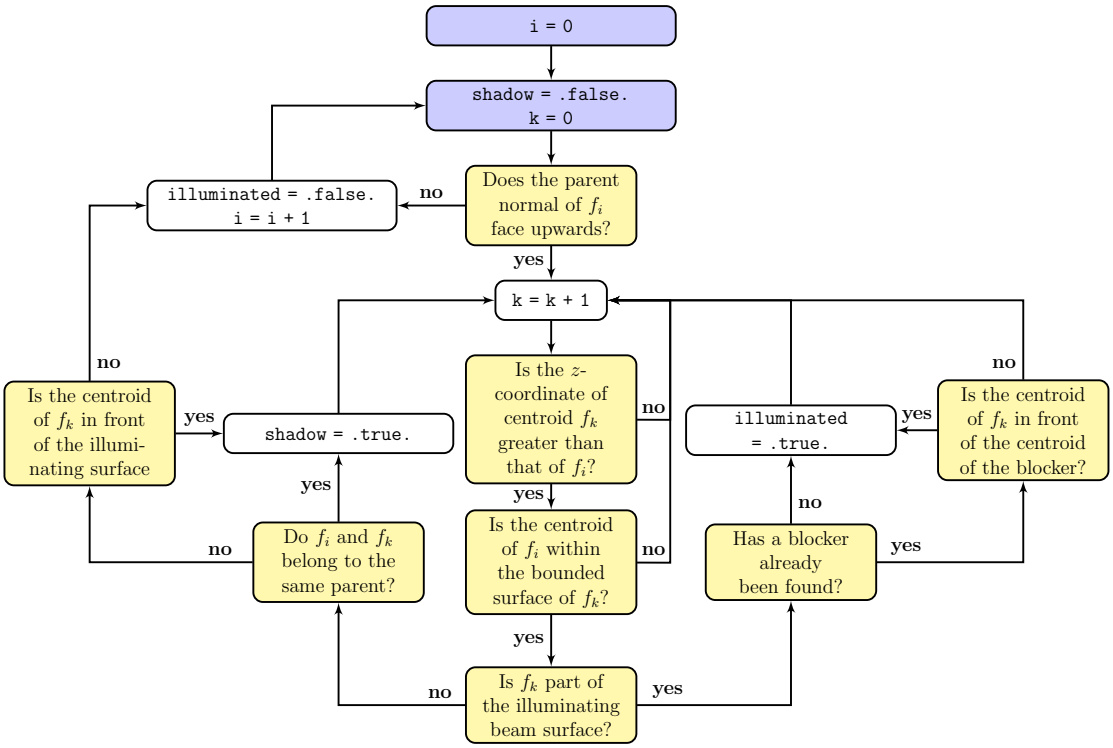

Figure 4.5: Diagram summarising the ray backtracing algorithm. The algorithm determines if the centroid of f^i is within the bounded cross section of a source beam facet f^k when projected along the beam propagation direction.

transmission matrix $\mathbf{F_T^j}$ are given by

$$\mathbf{F_R^j} = \begin{pmatrix} r_{||}^j & 0 \\ 0 & r_{\perp}^j \end{pmatrix}, \quad \mathbf{F_T^j} = \begin{pmatrix} t_{||}^j & 0 \\ 0 & t_{\perp}^j \end{pmatrix}, \tag{4.3}$$

where $r_{||}^j$, $r_{\perp}^j$, $t_{||}^j$, and $t_{\perp}^j$ are the Fresnel amplitude coefficients of reflection and transmission as described in Section 3.4.5. In contrast to the propagation direction of each beam, the Fresnel amplitude coefficients are calculated using the angle of incidence between the incident propagation vector and the local surface normal $\hat{\mathbf{n}}^\mathbf{j}$. The angle of incidence θ_i^j, angle of transmission θ_t^j, and refractive indices n_1 and n_2 are related via Snell's law. The amplitude matrices of the reflected and transmitted beams are computed by multiplying the incident amplitude matrices with the corresponding Fresnel matrices.

3. Third, the amplitude matrices of each beam are rotated into the new plane of incidence. The new plane contains the incident propagation vector $\hat{\mathbf{K}}_\mathbf{0}$ and the normal to the surface at the point of intersection $\hat{\mathbf{n}}$. The amplitude matrix is rotated about the incident propagation vector by the angle made between the old and new incidence planes. For an incident propagation vector $\hat{\mathbf{K}}_\mathbf{0}$, and unit vectors perpendicular to the old and new planes given by $\hat{\mathbf{e}}_\perp^\mathbf{i}$ and $\hat{\mathbf{e}}_\perp^\mathbf{s}$, respectively, the new amplitude matrix is found by applying a rotation matrix $\mathbf{R^j}$, which was described in Section 3.4.4,

$$\mathbf{R^j} = \begin{pmatrix} \hat{\mathbf{e}}_\perp^\mathbf{i} \cdot \hat{\mathbf{e}}_\perp^\mathbf{s} & -\hat{\mathbf{e}}_\perp^\mathbf{s} \cdot (\hat{\mathbf{K}}_\mathbf{0} \times \hat{\mathbf{e}}_\perp^\mathbf{i}) \\ \hat{\mathbf{e}}_\perp^\mathbf{s} \cdot (\hat{\mathbf{K}}_\mathbf{0} \times \hat{\mathbf{e}}_\perp^\mathbf{i}) & \hat{\mathbf{e}}_\perp^\mathbf{i} \cdot \hat{\mathbf{e}}_\perp^\mathbf{s} \end{pmatrix}. \tag{4.4}$$

Therefore, the reflected and transmitted amplitude matrices at f^j are given by

$$\mathbf{S_R^j} = \mathbf{R^j} \cdot \mathbf{F_R^j} \cdot \exp\left(ik_0 n \delta^j\right) \cdot \mathbf{S^k}, \tag{4.5}$$

and

$$\mathbf{S_T^j} = \mathbf{R^j} \cdot \mathbf{F_T^j} \cdot \exp\left(ik_0 n \delta^j\right) \cdot \mathbf{S^k}, \tag{4.6}$$

respectively, where $\mathbf{S^k}$ is the amplitude matrix at the source facet. A flow diagram summarising the near-field computation is shown in Figure 4.6. In the next step, the surface near-field is mapped to the far-field using a diffraction integral equation.

4.3 Far-Field Mapping

During the far-field mapping process, the near-field on the particle surface is integrated to calculate the electric field at a position in the far-field. The diffracted field is assumed to obey the Sommerfeld radiation condition [108]. There exist both volume and surface integral equations for computing the diffracted far-fields. The surface integral method is used here for its superior computationally efficiency and will be discussed in greater detail below. This section is based on theories described by Macke [35] and Karczewski [103] for

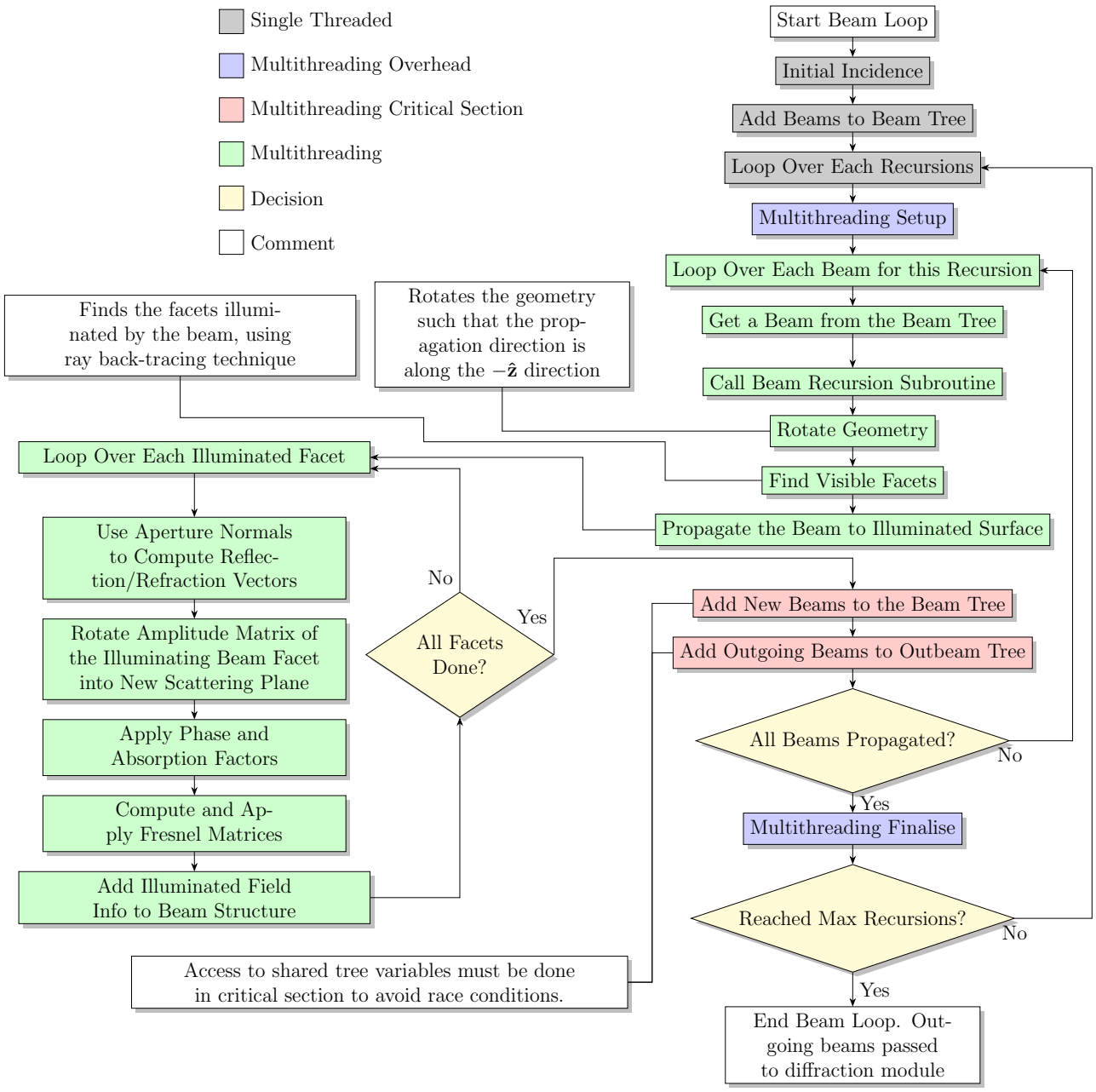

Figure 4.6: Schematic view of the beam loop.

electromagnetic diffraction at an aperture for an incident monochromatic plane wave. In this case, the incident electric field is described by

$$\begin{aligned}\mathbf{E}^{(i)}(\mathbf{r}) &= \mathbf{A}e^{ik_0(\hat{\mathbf{K}}\cdot\mathbf{r})},\\ \mathbf{H}^{(i)}(\mathbf{r}) &= \mathbf{B}e^{ik_0(\hat{\mathbf{K}}\cdot\mathbf{r})},\end{aligned} \tag{4.7}$$

where $\mathbf{E}^{(i)}$ and $\mathbf{H}^{(i)}$ are the incident electric and magnetic fields at position $\mathbf{r}$, $\mathbf{A}$ and $\mathbf{B}$ are complex vector amplitudes, and $\hat{\mathbf{K}} = (K_x, K_y, K_z)$ is the propagation vector. For a plane wave, $\mathbf{A}$ and $\mathbf{B}$ are related by $\mathbf{B} = \hat{\mathbf{K}} \times \mathbf{A}$. Imposing the Kirchhoff boundary conditions on the aperture, which approximates the diffracted field on the aperture as that of the incident field, gives that

$$\begin{aligned}\mathbf{n} \times \mathbf{E} &= \mathbf{n} \times \mathbf{E}^{(i)},\\ \mathbf{n} \times \mathbf{H} &= \mathbf{n} \times \mathbf{H}^{(i)}.\end{aligned} \tag{4.8}$$

In this case, the diffracted electric field due to an illuminated aperture S at a point $\mathcal{P}$ can be given by

$$\mathbf{E}(\mathcal{P}) = \nabla \times \mathbf{\Pi}_{\mathbf{m}}^{(\mathbf{i})} - 1/k_0 \nabla \times \nabla \times \mathbf{\Pi}_{\mathbf{e}}^{(\mathbf{i})}, \tag{4.9}$$

with

$$\begin{aligned}\mathbf{\Pi}_{\mathbf{m}}^{(\mathbf{i})} &= \frac{1}{4\pi}\iint_S \mathbf{n} \times \mathbf{E}^{(i)}(\mathcal{Q})\frac{e^{ik_0 r}}{r}dS,\\ \mathbf{\Pi}_{\mathbf{e}}^{(\mathbf{i})} &= \frac{1}{4\pi}\iint_S \mathbf{n} \times \mathbf{H}^{(i)}(\mathcal{Q})\frac{e^{ik_0 r}}{r}dS,\end{aligned} \tag{4.10}$$

where r is the distance from a point on the aperture $\mathcal{Q}$ to the point $\mathcal{P}$, $\mathbf{\Pi}_{\mathbf{e}}^{(\mathbf{i})}$ is the electric Hertz potential, and $\mathbf{\Pi}_{\mathbf{m}}^{(\mathbf{i})}$ is the magnetic Hertz potential. For the case of an incident plane wave, Eq. 4.9 can be simplified in the far-field limit ($r >> d, \lambda$) to [103]

$$\mathbf{E}(\mathcal{P}) = \hat{\mathbf{k}} \times (\mathbf{F} \times \mathbf{A}) + (\mathbf{F} \times \mathbf{B}) - \hat{\mathbf{k}} \cdot (\mathbf{F} \times \mathbf{B})\hat{\mathbf{k}}, \tag{4.11}$$

where

$$\mathbf{F} = C\mathbf{n}\iint_S e^{ik_0(\hat{\mathbf{K}}-\hat{\mathbf{k}})\cdot\mathbf{R}}dS, \quad C = \frac{ik_0 e^{ik_0 r_0}}{4\pi r_0}. \tag{4.12}$$

Here, $\hat{\mathbf{k}} = (k_x, k_y, k_z)$ is the unit vector from the point of integration over the aperture to the point of observation. It varies for each point of observation and as a function of position over the aperture. $\mathbf{R} = (R_x, R_y, R_z)$ is the position vector of each area element and r_0 is the distance from the centre of the aperture to the point of observation. A subtle point of interest here is that the distance r from $\mathcal{Q}$ to $\mathcal{P}$ has been removed and substituted for the distance r_0. By separating the components of the bracketed term in the integrand exponent, the physical representation of each term can be identified. Firstly, $\exp(ik_0\hat{\mathbf{K}} \cdot \mathbf{R})$ describes how the phase of the incoming plane wave varies across the aperture. Secondly, if the exponential term in C is included, $\exp(ik_0 r_0\hat{\mathbf{k}} \cdot \mathbf{R})$ describes (to a first-order approximation) the phase

change of the diffracted wavelet from point $\mathcal{Q}$ to point $\mathcal{P}$. If the aperture is planar, the coordinate system may be rotated about the centre of the aperture so that the aperture lies in the xy plane. In this case, $R_z = 0$. Furthermore, if the incident wave can be assumed as a plane wave, it will be shown that the integral in Eq. 4.12 can be converted to a summation around the contour of the aperture [35, 109]. This provides a computationally cheap method for mapping from the near to the far-fields. Under these constraints, Eq. 4.12 simplifies to

$$\mathbf{F} = C\mathbf{n} \iint_S e^{ik_0[(K_x - k_x)x' + (K_y - k_y)y']} dS. \tag{4.13}$$

Defining new constants $k'_x = k_0(K_x - k_x)$ and $k'_y = k_0(K_y - k_y)$, Eq. 4.13 becomes

$$\mathbf{F} = C\mathbf{n} \iint_S e^{i(k'_x x' + k'_y y')} dS. \tag{4.14}$$

Now, with the introduction of two new variables, P and Q, Green's theorem will be applied to convert Eq. 4.14 to a line integral around the contour of the aperture. Choosing

$$Q = \frac{e^{i(k'_x x' + k'_y y')}}{2ik'_y}, \quad P = \frac{e^{i(k'_x x' + k'_y y')}}{2ik'_x}, \tag{4.15}$$

the integral $\mathbf{F}$ can be rewritten as

$$\mathbf{F} = C\mathbf{n} \iint_S \left(\frac{\partial Q}{\partial y'} + \frac{\partial P}{\partial x'} \right) dS = \oint_S \Big(Q dx' - P dy' \Big), \tag{4.16}$$

where $dS = dx'dy'$, since the aperture is planar and located in the xy plane. For polygonal apertures with N vertices, Eq. 4.16 can be written as a summation over the contributions from each edge:

$$\mathbf{F} = C\mathbf{n} \sum_{j=1}^{N} \int_j^{j+1} \Big(Q dx' - P dy' \Big), \tag{4.17}$$

where the integration limits indicate that the integral should be evaluated for the edge between vertices j and $j+1$. Next, expressions for x' and y' along the edge between the two vertices will be derived. The gradient and reciprocal gradient between the two vertices are

$$m_j = \frac{y_{j+1} - y_j}{x_{j+1} - x_j}, \quad n_j = \frac{x_{j+1} - x_j}{y_{j+1} - y_j}, \tag{4.18}$$

respectively. Using these expressions, the y' dependence in Q can be rewritten in terms of x' and vice versa for P. Eq. 4.17 then becomes

$$\mathbf{F} = C\mathbf{n} \sum_{j=1}^{N} \int_j^{j+1} \left(\frac{e^{i\{k'_y[y_j + (x' - x_j)m_j] + k'_x x'\}}}{2ik'_y} dx' - \frac{e^{i\{k'_x[x_j + (y' - y_j)n_j] + k'_y y'\}}}{2ik'_x} dy' \right). \tag{4.19}$$

After integration and some rearranging, the final expression is given by

$$\mathbf{F} = C\mathbf{n} \sum_{j=1}^{N} \alpha[e^{i\delta} - e^{i(\delta + \omega_1)}] - \beta[e^{i\delta} - e^{i(\delta + \omega_2)}], \tag{4.20}$$

with, $\alpha = \frac{1}{2k'_y(k'_y m_j + k'_x)}$, $\beta = \frac{1}{2k'_x(k'_x n_j + k'_y)}$, $\delta = k'_x x_j + k'_y y_j$, $\omega_1 = (x_{j+1} - x_j)(k'_y m_j + k'_x)$, and $\omega_2 = (y_{j+1} - y_j)(k'_x n_j + k'_y)$. With this formulation, the integral in Eq. 4.12 representing the scalar Fraunhofer pattern can be readily evaluated to yield $\mathbf{F}$.

To determine $\mathbf{E}(\mathcal{P})$ from Eq. 4.11, further work must be done to account for the vector nature of the scattered light. For this, the coordinate system is rotated about the $\hat{\mathbf{z}}$-axis such that $\hat{\mathbf{e}}_{||}$ lies in the xz plane. By using the unitary property and relation between the incident propagation vector and the electric field component vectors:

$$\hat{\mathbf{K}}^2 = \hat{\mathbf{e}}_{||}^2 = \hat{\mathbf{e}}_{\perp}^2 = 1, \quad \hat{\mathbf{K}} \times \hat{\mathbf{e}}_{||} = \hat{\mathbf{e}}_{\perp}, \tag{4.21}$$

the x, y, and z components of the electric field components can be expressed in terms of $\hat{\mathbf{K}}$ by

$$\hat{\mathbf{e}}_{||} = \frac{1}{\eta}\begin{pmatrix} K_z \\ 0 \\ -K_x \end{pmatrix}, \quad \hat{\mathbf{e}}_{\perp} = \frac{1}{\eta}\begin{pmatrix} -K_x K_y \\ \eta^2 \\ -K_y K_z \end{pmatrix}, \quad \eta = \sqrt{1 - K_y^2}. \tag{4.22}$$

For each point of observation in the far-field, two more unit vectors $\hat{\mathbf{l}}$ and $\hat{\mathbf{m}}$ are introduced to define the reference plane for which the electric field components will be calculated. If $\hat{\mathbf{k}}$, $\hat{\mathbf{l}}$, and $\hat{\mathbf{m}}$ are chosen as a triad of mutually orthogonal unit vectors, and $\hat{\mathbf{l}}$ is again chosen to lie in the xz plane, the components of $\hat{\mathbf{l}}$ and $\hat{\mathbf{m}}$ can be expressed in a similar manner in terms of $\hat{\mathbf{k}}$ by

$$\hat{\mathbf{l}} = \frac{1}{\zeta}\begin{pmatrix} k_z \\ 0 \\ -k_x \end{pmatrix}, \quad \hat{\mathbf{m}} = \frac{1}{\zeta}\begin{pmatrix} -k_x k_y \\ \zeta^2 \\ -k_y k_z \end{pmatrix}, \quad \zeta = \sqrt{1 - k_y^2}. \tag{4.23}$$

A diagram illustrating the arrangement is shown in Figure 4.7. In this way, it may be shown that [103], the far-field amplitude matrix defined with respect to the directions $\hat{\mathbf{l}}$ and $\hat{\mathbf{m}}$ is given by

$$\mathbf{S_{far}} = 2F\begin{pmatrix} a & b \\ -b & a \end{pmatrix}\mathbf{S_{inc}}, \tag{4.24}$$

$$a = \frac{1}{2}\left(-k_z\sqrt{\eta/\zeta} - K_z\sqrt{\zeta/\eta}\,\right), \quad b = \frac{1}{2}\left(-k_x k_y\sqrt{\eta/\zeta} + K_x K_y\sqrt{\zeta/\eta}\,\right). \tag{4.25}$$

In the application considered here, the incident electric field is replaced by the amplitude matrix of a transmitted beam. Finally, 2 more rotation matrices are applied to obtain the electric field components with respect to static scattering planes in the original coordinate system.

1. First, for an incidence direction along the $-\hat{\mathbf{z}}$-axis, and scattering direction $\hat{\mathbf{k}}$ pointing from the particle centre of mass to the observation point, the scattering plane containing both these vectors has a normal given by $\hat{\mathbf{M}} = -\hat{\mathbf{z}} \times \hat{\mathbf{k}}$. To rotate the far-field components defined by Eq. 4.24 into this plane, the rotation matrix $\mathbf{R_1}$ is applied to rotate the electric field components about the direction $\hat{\mathbf{k}}$ from the plane perpendicular to $\hat{\mathbf{m}}$ to the plane perpendicular to $\hat{\mathbf{M}}$ [101], with

$$\mathbf{R_1} = \begin{pmatrix} \hat{\mathbf{m}} \cdot \hat{\mathbf{M}} & -\hat{\mathbf{M}} \cdot (\hat{\mathbf{k}} \times \hat{\mathbf{m}}) \\ \hat{\mathbf{M}} \cdot (\hat{\mathbf{k}} \times \hat{\mathbf{m}}) & \hat{\mathbf{m}} \cdot \hat{\mathbf{M}} \end{pmatrix}. \tag{4.26}$$

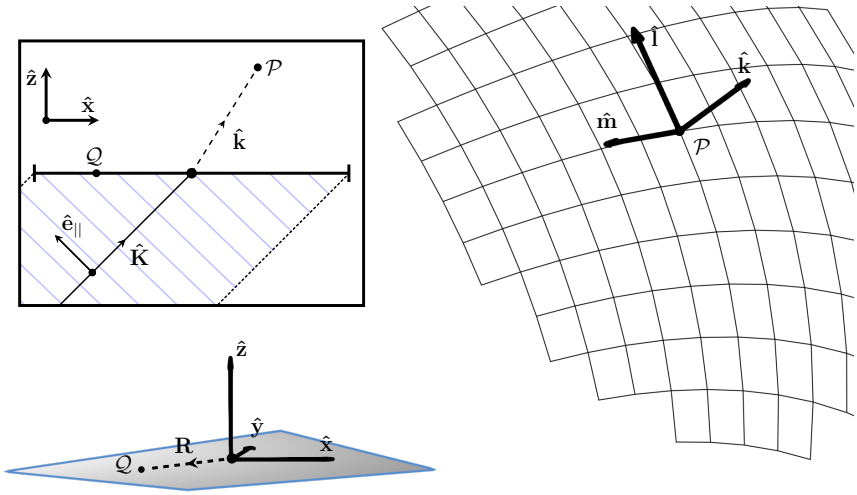

Figure 4.7: The diffraction geometry. An incident beam is diffracted by a planar, polygonal aperture. The coordinate system has been rotated such that the aperture lies in the xy plane and the incident beam propagation vector $\hat{\mathbf{K}}$ and parallel field component $\hat{\mathbf{e}}_{||}$ are aligned with the xz plane. The point of observation in the far-field is denoted by $\mathcal{P}$, and is located in the direction $\hat{\mathbf{k}}$ from the centre of the aperture. A grid structure is shown as an example of the different angular positions at which the far-field may be evaluated.

2. Second, the initial incident amplitude matrix is pre-rotated about the **z**-axis from the yz plane into the scattering plane, which allows for a direct comparison between the scattered and incident fields. For each azimuthal scattering direction, each transmitted beam is premultiplied by the rotation matrix $\mathbf{R_0}$:

$$\mathbf{R_0} = \begin{pmatrix} -\sin\phi & -\cos\phi \\ \cos\phi & -\sin\phi \end{pmatrix}, \tag{4.27}$$

where ϕ is measured as shown in Figure 2.2. Close to the direct forwards and backwards directions, ϕ and thus $\mathbf{R_0}$ are not well defined. Therefore, in these cases the PBT obtains $\mathbf{R_0}$ from the values of ϕ at $\theta = 1°$. The final expression for the diffracted far field components is given by

$$\mathbf{S_{far}} = \mathbf{R_1} \cdot 2F \begin{pmatrix} a & b \\ -b & a \end{pmatrix} \mathbf{S_T} \cdot \mathbf{R_0}. \tag{4.28}$$

To summarise, Eq. 4.24 relates the parallel and perpendicular diffracted far-field components from a planar aperture for an incident plane wave, with the scalar Fraunhofer pattern F obtainable from Eq. 4.20. By a summation over all diffracted beams, a complete description for the electric field in the far-field is obtained as an amplitude matrix as a function of observation position, which can be written mathematically as

$$\mathbf{S_{far}} = \sum_{m=0}^{M} \sum_{l=1}^{L(m)} \sum_{j(l)} {}_{\mathbf{m}}^{\mathbf{l}}\mathbf{S}_{\mathbf{far}}^{\mathbf{j}}, \tag{4.29}$$

where M is the total number of recursions, $L(m)$ is the total number of beams at the m^{th} recursion, $j(l)$ are the indices of facets illuminated by the l^{th} beam of the m^{th} recursion, and $\mathbf{{}_{m}^{l}S_{far}^{j}}$ are the far field amplitude matrices for each transmitted amplitude matrix $\mathbf{{}_{m}^{l}S_{T}^{j}}$. Babinet's principle is used to account for the scattering of light which is not directly incident upon the particle geometric cross section. The externally diffracted field is computed from the amplitude matrix at facets illuminated by the initial incident wave as described in Section 4.2 but without applying the Fresnel matrices. The total scattered field is obtained by a summation of the diffraction of surface fields due to transmission and reflection with external diffraction. Finally, the Mueller matrix can be determined from the total amplitude matrix by well-known relations (Appendix A).

4.4 Code Overview and Architecture

In this section, the PBT code is described in more detail. The code is written in Modern Fortran; a fast low-level coding language with many similarities to C. It contains implementations of parallel computing techniques, including multithreading via OpenMP [110] and message-parsing-interface via OpenMPI [111]. The main program is available in both sequential and MPI versions and can be found on Github [102]. The sequential version is designed to run on a single shared memory processor, whereas the MPI version is designed to be run across several distributed memory processors. The source code is divided into several key modules:

1. Types module: Contains definitions of several derived types, constants, and format specifiers. Derived types act in a similar way to structures in C, or classes in Python. A single variable of derived type can have many components, each with a different type or attributes.

2. Input module: Responsible for initialising the code. This includes parsing the command line, reading input files, initialising the job settings and the particle geometry.

3. Beam loop module: Receives the particle geometry and an incident beam as an input, and computes the amplitude matrix on the particle surface as an output. This section of the code traces the reflection and refraction of beams of light between the parent structures of the geometry.

4. Diffraction module: Responsible for computing the far-field mapping. It takes the amplitude matrix on the surface of the particle as an input, and computes the amplitude matrix in the far-field as an output. For most jobs, this section is responsible for the majority of computation time.

5. Outputs module: Converts the far-field amplitude matrix to a Mueller matrix, and also computes several integrated scattering parameters.

6. Misc. module: Contains various subroutines that are used across the other modules.

7. CC hex module: Contains a single subroutine for generating Gaussian random hexagonal prisms.

8. MPI module: Contains subroutines which are used by the MPI version of the PBT code. These are mainly MPI send and receive commands, which are used to communicate data between different distributed memory processes.

A diagram summarising the flow of operations is shown in Figure 4.8.

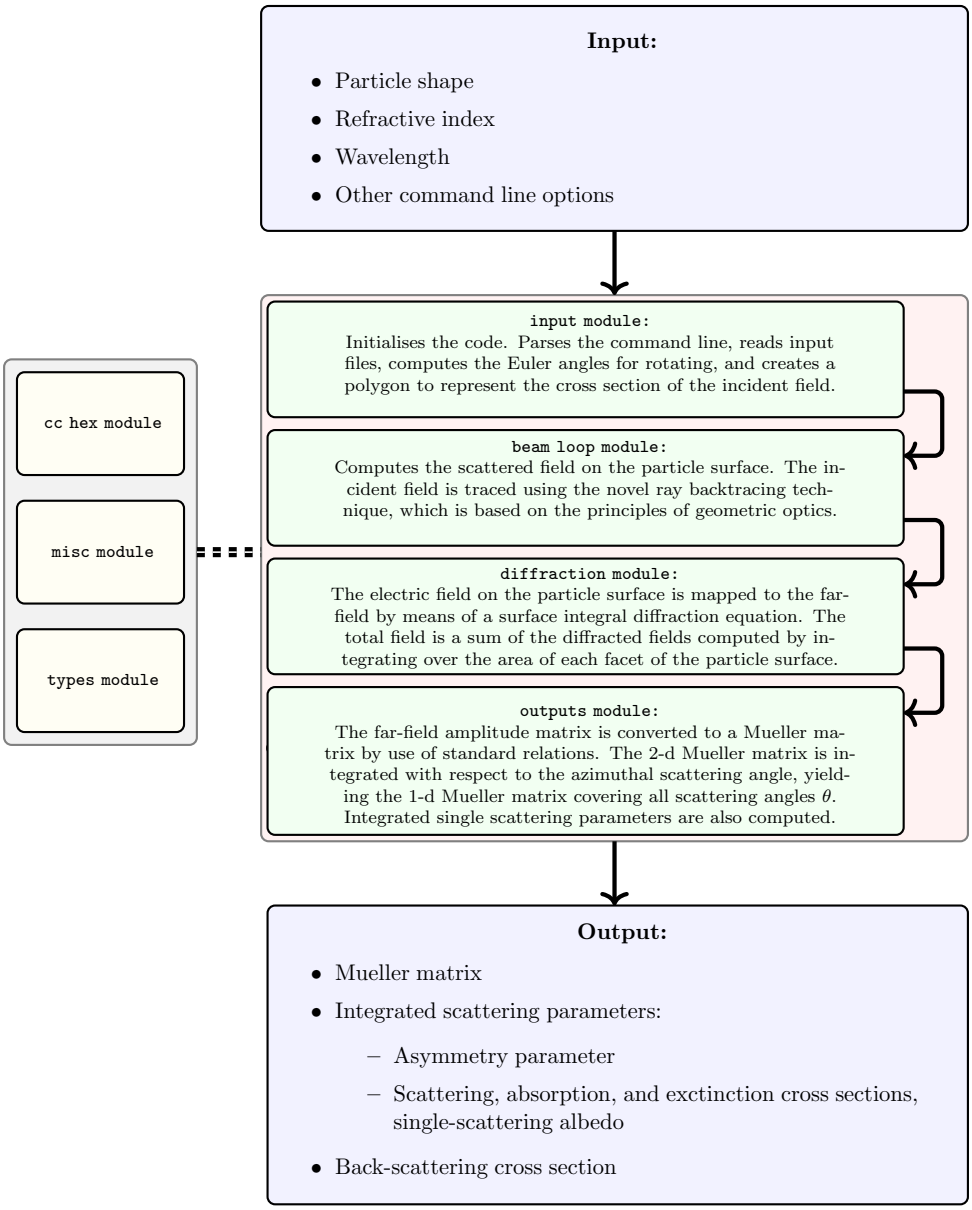

Figure 4.8: Code layout.

Types Module

The types module contains definitions for derived type variables, constants, and format specifiers that are used throughout the code. As such, this module is included in the preamble

for almost all other modules and is therefore often compiled first. Below, a list of derived type variables, an overview of their use, and their components are given:

1. `outbeam_type`: Contains information about the external electric field at a facet of the particle surface.

2. `cc_hex_params_type`: Contains the parameters which define the geometrical shape of Gaussian random hexagonal prisms [74].

3. `geometry_type`: Contains information about the particle geometry. This includes the vertices, facets, normals, and parent structures, which play a fundamental role in determining how the light interacts with the particle.

4. `facet_type`: Contains information about a facet, which is defined by a list of vertices, ordered anti-clockwise as viewed from outside.

5. `parent_type`: Contains information about the macroscopic features of the particle shape, known as parents. This includes the average normal, midpoint, total surface area, and the number of facets assigned to it.

6. `output_parameters_type`: Contains a variety of output parameters with physical importance: absorption, scattering, and extinction cross sections and efficiencies, asymmetry parameter, illuminated geometric cross section, back-scattering cross section.

7. `job_parameters_type`: Contains a a large set of parameters which allow for a high level of job customisation. The settings of the job are usually set through the use of command line arguments (see Appendix C).

8. `beam_type`: Contains all the information about a single propagating beam in the near-field. Each beam propagates along a single direction from a collection of facets. The amplitude matrix is stored at the centroid of each facet. The beam is formed from a section of the particle surface where it originates, and a section of the particle surface where it terminates. The information about the electric field stored in the `field_in_type` and `field_out_type` variables, respectively:

   (a) `field_in_type`: Contains information such as the perpendicular field vector and amplitude matrix at a facet, from which part of a beam is propagating.

   (b) `field_out_type`: Contains information such as the perpendicular field vector, whether or not total internal reflection occurred, and reflected and refracted propagation directions at facet, at which part of a beam terminates.

Input Module

The input module is responsible for managing the code initialisation. The first subroutine, `parse_command_line`, reads input arguments from the command line. A `select case` statement filters command line arguments and sets specific variables in the job parameters data structure. A detailed explanation of the command line arguments is given in Appendix C, along with the default values. The subroutine `PDAL2` is responsible for reading the particle

geometry from a file. It is a modified version of the subroutine found in the ray tracing code by Macke [35], which is extended to accommodate particles files written in wavefront format (`.obj` file extension). It reads the parent structures from a file, computes the midpoints, areas, normals of each facet, the vectors of all edges in each facet, and translates the centre of mass of the particle to the origin. The subroutine `init_loop` is responsible for setting the Euler angles used during the orientation averaging loop. Any symmetries in β and γ specified restricts the range of Euler angles. If the `-intellirot` command line argument is specified, the angles are chosen from a grid of uniformly spaced values of β and γ; otherwise, they are chosen at random. The numbers for each Euler angle are initialised as a value in the range $[0, 1]$. They are then remapped onto the appropriate ranges for each Euler angle during the `PROT_MPI` subroutine. The `PROT_MPI` subroutine rotates the particle into the corresponding orientation. If using the Euler angle rotation method, the α and γ angles are distributed in the range $[0, 360°]$, whereas the β angle is distributed according to the function $\arccos(1 - 2x)$, where x is a value between 0 and 1. This gives rise to β values in the range $[0, 180°]$, with more angles concentrated towards the equator (90°) and less towards the poles (0 and 180°). In spherical polar coordinates, the solid angle element $d\Omega = \sin\theta d\theta d\phi \propto \sin\theta$, indicating that contours of constant θ are more closely spaced towards the poles than at the equator. The chosen mappings for β and γ ensure that the particle orientations are uniformly distributed over the solid angle Ω. The `make_incident_beam` subroutine sets up a simple square polygon to represent the incident plane wavefront. The dimensions of the square are set so that the particle is fully illuminated by the incident beam, although it is straightforward to modify this to partially illuminate the particle. The z position is set to 1000, which is intended to be always above the particle. In this subroutine, the incident propagation direction is set as along the $-\hat{\mathbf{z}}$-axis and the $\hat{\mathbf{e}}_\perp$ direction is defined along the $+\hat{\mathbf{x}}$-axis.

Beam Loop Module

The beam loop module is responsible for taking the incident field as an input and computing the near-field as a sum of amplitude matrices over the particle surface as an output (Eqs. 4.5 and 4.6). The beam loop either takes place in `beam_loop_for_speed` or `beam_loop_for_memory` (depending on whether the user specified the command line arguments `-speed` or `-memory`). Both versions essentially perform the same computation, but in the version for optimum speed, all beams are traced first and then all beams are diffracted second. In the version for optimum memory use, beams are traced and then diffracted in a recursion by recursion manner. In the version for optimum speed, the first step is to call subroutine `recursion_inc`, which has the following sequence of operations:

1. Incident illumination: The initial illuminating beam defined in subroutine `make_incident_beam` is propagated. To propagate the beam, the following sequence is undertaken:
   (a) Find the illuminating facets: Subroutine `find_vis_inc` is called to determine the facets of the geometry illuminated by the incident beam.
   (b) Allocate space in the beam data structure: One entry in the beam structure is

allocated to store information about the electric field at each of the illuminated facets.

(c) Computing the electric field: Computing the electric field at the illuminated facets requires several steps:

i. The reflected propagation vector is computed using the parent normal.

ii. The new perpendicular field vector is computed using the cross product of the facet normal and the reflected propagation vector.

iii. The rotation matrix is computed, which is used to rotate about the incident propagation direction from the old to the new reference plane.

iv. The distance δ to each facet is used to apply the phase factor $\exp(ik\delta)$ and the incident amplitude matrix is multiplied by the rotation matrix to rotate it into the new reference plane.

v. External diffraction (incident illumination only): A copy of the amplitude matrix for each facet at this point is saved to the external diffraction outbeam structure, which is used to compute the external diffraction.

vi. The Fresnel coefficients of reflection and transmission are calculated based on the angles of incidence and transmission made at the parent. The coefficients are then used to construct the Fresnel matrices. The amplitude matrix is multiplied by the Fresnel matrices to obtain the external reflected amplitude matrix, and the internal transmitted amplitude matrix.

vii. Finally, information about the reflected and transmitted fields are added to the beam data structure, where they may be either used to propagate beams in the next recursion or to compute the diffracted far-field.

2. Adding to the beam tree: The beam tree acts as a parent structure for holding information about all the beams propagated in the near-field, excluding the initial illumination. Any beams which are reflected or transmitted from the particle surface are added to the beam tree for later use.

Any remaining beams in the beam tree are then traced if the energy and cross sectional area are above their minimum values, and at least one of the following conditions are satisfied:

1. The maximum number of recursions has not been reached.

2. The beam is a total internal reflection event, and the maximum number of total internal reflections has not been reached.

The code contains two variants of the recursion subroutine, namely `recursion_int` and `recursion_ext`, which are called depending on whether the beam is propagating internally or externally, respectively. They differ from `recursion_inc` only in the fact that instead of propagating the beam from polygon defining the incident illumination, the beam is propagated from a portion of the particle surface. In addition, small changes are made depending on whether the beam is internally or externally propagating, to account for the fact that the surface normals face outwards from the particle and therefore the direction of some cross products are inverted. In addition, any externally propagated beams which do not reenter

the particle are marked as outgoing beams, and are then added to the diffraction tree for later use. Finally, the beam loop finalises with some checks based on the conservation of energy and, if enabled, parts of the beam may be exported in `.json` format to an output file.

Diffraction Module

The diffraction module is responsible for computing the near to far-field mapping. For each facet through which a beam is transmitted and does not reenter the particle, Eq. 4.24 is computed for each of the far-field bins. The main procedure for this is contained in subroutine `diff_main`, which takes the outgoing beam tree as an input, and returns the far-field amplitude matrix as an output. The procedure is described by the following steps:

1. First, the vector position of each far-field bin is computed based on the scattering angles θ and ϕ. This is computed in subroutine `make_far_field_bins` according to Eq. 2.3, with a distance to the far-field set to $R = 1 \times 10^6$.

2. Second, the diffraction integral is computed. This is usually the most computationally intensive section of code. This is because the number of floating-point operations (also known as *flops*) scales approximately with the product of the number of facets in the mesh and the number of far-field bins. Therefore to reduce the time taken, this section of code is multi-threaded and heavily vectorised. The multi-threading aspect allows the code to take advantage of modern central processing unit (CPU) architectures, which often have more logical threads of operation than CPU cores. In most cases, this gives at least a 2x speedup for the diffraction computation. The vectorisation is achieved by avoiding conditional statements in loops so that the same instructions can be sent to the arithmetic logic unit in the CPU. Code written in this way is often referred to as *single instruction, multiple data* (SIMD), and graphics processing units (GPUs) are designed to perform such tasks efficiently. According to the OpenMP documentation, only the innermost loops are vectorised [110] and therefore any nested loops should be reordered so that the largest loops have the innermost position. Furthermore, elements of multidimensional arrays in Fortran are stored in memory according to the first index, which makes it faster to loop over the first dimension of array than the other dimensions. Hence, arrays in this module are defined in such a way that innermost nested loops always tend to loop over the first dimension of multidimensional arrays. The diffraction is computed in the `diffraction` subroutine via the following key steps:

   (a) First, a facet of the mesh and the amplitude matrix at its centroid is taken as an input. Since each mesh element has an arbitrary location and orientation, it is first rotated into the xy plane and translated to the origin. The vertices of the facet have now been transformed into a new coordinate system. A check is performed to ensure that the facet normal faces along the positive z-axis. The positions of the far-field bins relative to the facet must be accounted for with care. This is because even small errors in the distances can lead to significant errors in computing the phase of the electric field as it is mapped from the facet to the far-field. Therefore, the far-field bins are rotated and translated using the same transformations as is used for the facet.

(b) Second, for each far-field bin, the polarisation of the scattered field is computed in subroutine `karczewski` according to the theory described by Eq. 4.25.

(c) Third, the appropriate rotation matrices are applied to the amplitude matrix. The first, defined by Eq. 4.26, rotates the far-field amplitude matrix from a plane defined with respect the rotated coordinate system into the scattering plane defined with respect to the unrotated coordinate system. The second, defined by Eq. 4.27, is the pre-rotation matrix, which effectively rotates the incident amplitude matrix into the scattering plane.

(d) Finally, the contour integral defined by Eq. 4.20 is computed in subroutine `contour_integral`. This is usually the most time consuming part of the computation. Physically, the contour integral represents the Fraunhofer (scalar) diffraction pattern. A scalar value is computed at each far-field bin, which is then used to multiply the far-field amplitude matrix to arrive at the final value for the diffracted field.

The `diffraction` subroutine is called for each facet of each outgoing beam and the total far-field is computed as the sum.

3. Third, the `diffraction` subroutine is called for the computation of the external diffraction. For this, the facets illuminated by the incident field are used, with the Fresnel coefficients of reflection and refraction omitted. The external diffraction is added to the field computed in the previous step. The diffracted amplitude matrix computed at each far-field bin is then passed to the outputs module for finalisation.

Outputs Module

The outputs module is a relatively simple section of the code. It is responsible for converting the far-field amplitude matrix to a Mueller matrix. This is performed in subroutine `ampl_to_mueller` according to the definitions given by Hovenier and Mee (Appendix A) [87]. Subroutine `get_1d_mueller` uses a 3-point Lagrange polynomial interpolation method [112] to integrate over ϕ and compute the 1D Mueller matrix. The module also contains a subroutine called `writeup`, which outputs various information of use, including integrated scattering parameters, to different files. Subroutines `cache_job` and `cache_remaining_orientations` are used to save a temporary state of the code, in the event that the walltime limit is exceeded.

Misc. Module

The miscellaneous module contains a large number of utility functions that are used throughout the code. For sake of brevity, a few of the most important ones are described below.

1. `resume_job`: Initialises the resuming of a previously cached job. This is done by reading from a cache directory containing the parameters of the cached job, as well as the completed orientations and the far-field Mueller matrix.

2. `Qsort_real`: An implementation of the quicksort algorithm [113]. It is used for sorting large arrays.

3. `triangulate`: Takes a 3D surface as an input geometry, triangulates it using the Triangle program [114], and then returns the triangulated 3D surface. The Triangle program is designed to work in 2D, so each facet of the geometry is first prerotated into the xy plane and written to a temporary file. The filename is passed as an input to the Triangle program. The output is then read back in and rotated back into its original orientation. This is repeated for all facets of the original geometry.

4. `PDAS`: Outputs the 3D crystal to files in Wavefront format (`.obj`) and Macke ray-tracing format (`.cry`).

CC Hex Module

The CC Hex Module generates hexagonal prism geometries with gaussian random roughness according to that described in [74].

MPI Module

The MPI module contains a few subroutines that are used by the MPI version of the code. Since MPI is an implementation of distributed memory processing, information must be explicitly communicated between different computing processes by use of calls to `MPI_SEND`, `MPI_RECV`, or `MPI_REDUCE` commands. This is mostly limited to summations of the Mueller matrix and integrated scattering parameters across different processes.

Summary

In this chapter, the PBT method has been described. It is the novel method of this work and is a physical-optics hybrid light scattering method for large, non-spherical particles, including those with surface roughness. In the next chapter, the accuracy of the PBT method is tested against the DDA method in two benchmark studies. This is followed by an application: the computation of single-scattering parameters of smooth hexagonal ice plates.

Chapter 5

Application & Results

Introduction

5.1 Hexagonal Columns with Gaussian Random Surface Benchmark

5.1.1 Method

In this section, the results from the PBT for smooth and rough hexagonal columns with length $l = 10$ µm, and hexagonal edge length $r = 5$ µm are presented. Rough particles are generated using Gaussian random roughness with correlation length 0.5 µm and standard deviation 0.1 µm as described by Collier et. al [74]. The accuracy of the results is measured by comparison with the ADDA code [62], which is an implementation of the DDA method. The accuracy of ADDA has been reported several times in the literature and here the results are considered as a benchmark for comparison [62, 96, 115, 116]. While the formulation of the DDA method is a direct implication of the Maxwell equations, an exact solution is derived according to the set of dipoles rather than the original scatterer. Therefore, in this study two main criteria are considered to accurately represent the particle by an array of dipoles. Firstly, the number of dipoles per wavelength d is chosen in accordance with the ADDA 'rule-of-thumb' which requires that $d \leq 10/(\lambda|n|)$. Secondly, d is required to be smaller than any characteristic sizes of the particle. For particles with Gaussian roughness, d is chosen such that at least 10 dipoles per correlation length are present.

5.1.2 Results & Discussion

The logarithms of the 2D phase functions for non-absorbing smooth and rough hexagonal columns in a fixed orientation with refractive index n =1.31+0i are shown in Figure 5.2. The results for other elements of the Mueller matrix for the smooth and rough particles in the same orientation with refractive index n =1.31+0i are shown in Figure 5.4. The particle orientation is produced by first aligning the prism axis with the z-axis, then by rotating with Euler angles $\alpha = 0°$, $\beta = 30°$, $\gamma = 20°$ according to the "zyz-notation" as given in [71]. The azimuthal and polar scattering angles may be inferred from the diagram shown

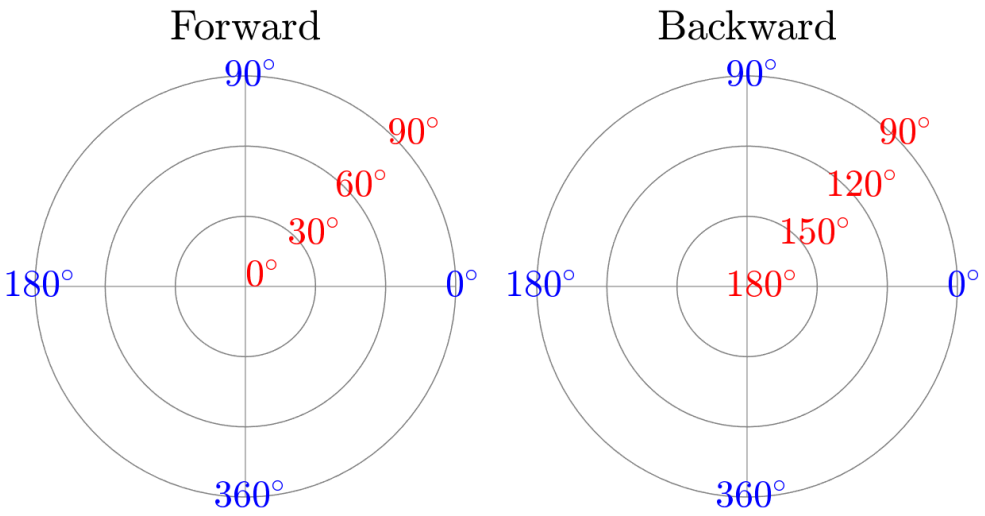

Figure 5.1: Diagram depicting the azimuthal (blue) and scattering (red) angles for 2D polar plots in the forwards (left) and backwards (right) directions.

in Figure 5.1. The PBT method produces results in $\sim 1/1000^{\text{th}}$ of the computation time required for the DDA computations. The 1D phase function is computed by integration over phi using a 3-point Lagrange polynomial interpolation method [112]. Table 5.1 summarises the values for various integrated scattering parameters of interest. By computing the mean values averaged over the smooth and rough particle configurations, the errors in the asymmetry parameter, and scattering and extinction efficiencies are -1.0%, -1.4%, -1.2%, respectively. For the smooth, non-absorbing (n =1.31+0i) particle, the PBT patterns in Figure 5.2 closely resemble those computed with DDA. In the direct forwards scattering, a strong peak is observed, corresponding to external diffraction combined a beam entering and being transmitted through a pair of parallel surfaces. At approximately 60° scattering angles, several regions of high scattering intensity are observed, which correspond to

	n	$g^{(dda)}$	$g^{(pbt)}$	$\frac{g^{(pbt)}-g^{(dda)}}{g^{(dda)}}$ [%]	$Q_{sca}^{(dda)}$	$Q_{sca}^{(pbt)}$	$\frac{Q_{sca}^{(pbt)}-Q_{sca}^{(dda)}}{Q_{sca}^{(dda)}}$ [%]	$Q_{ext}^{(dda)}$	$Q_{ext}^{(pbt)}$	$\frac{Q_{ext}^{(pbt)}-Q_{ext}^{(dda)}}{Q_{ext}^{(dda)}}$ [%]
Smooth	1.31 + 0i	0.807	0.820	+1.6	2.580	2.537	-1.7	2.580	2.537	-1.7
	1.31 + 0.01i	0.941	0.937	-0.4	1.363	1.407	+3.2	2.251	2.154	-4.3
	1.31 + 0.1i	0.967	0.966	-0.1	1.112	1.057	-4.9	2.111	2.090	-1.0
Rough	1.31 + 0i	0.769	0.762	-0.9	2.183	2.142	-1.9	2.183	2.142	-1.9
	1.31 + 0.01i	0.941	0.906	-3.7	1.278	1.285	+0.5	2.236	2.251	+0.7
	1.31 + 0.1i	0.969	0.945	-2.5	1.177	1.135	-3.6	2.244	2.266	+1.0

Table 5.1: Summary of the asymmetry parameter g, scattering efficiency Q_{sca}, and extinction efficiency Q_{ext} computed with the DDA and PBT methods for the smooth and rough particles in the orientation as shown in Figure 5.2.

transmitted beams undergoing 1 or 2 internal reflections. In the backscattering hemisphere, external reflection combined with a transmitted beam undergoing total internal reflection is observed at approximately 120°. In general, PBT computations are able to reproduce

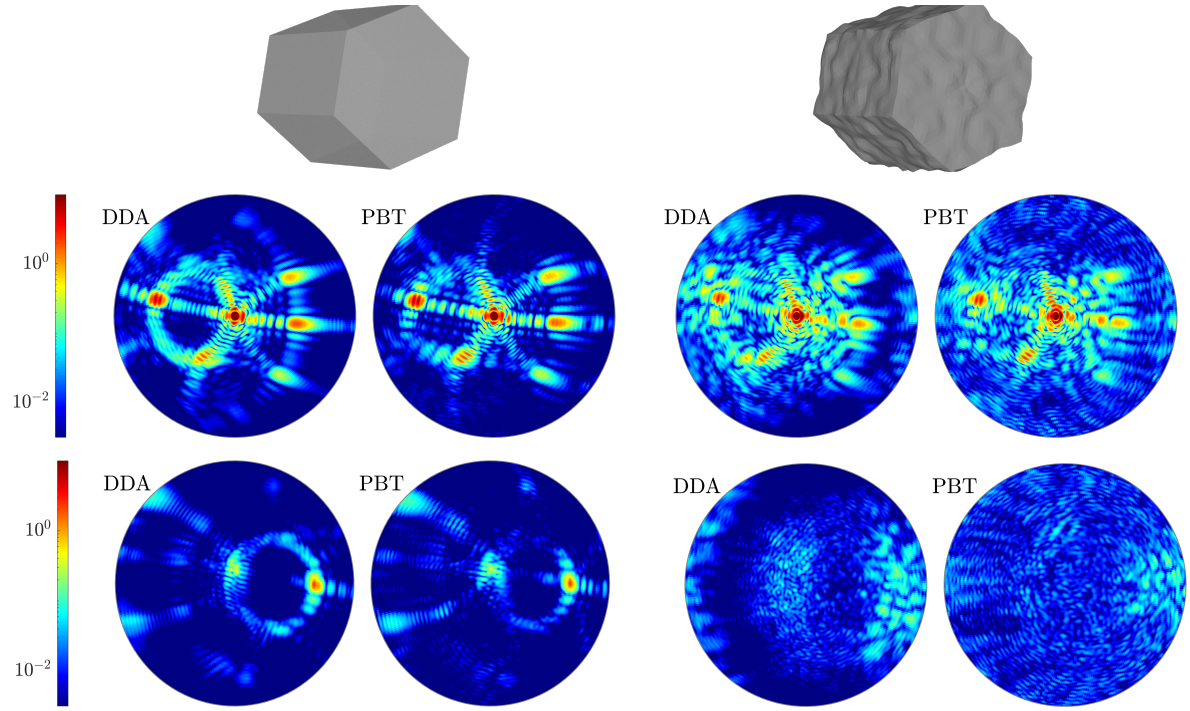

Figure 5.2: The logarithms of the 2D phase functions for smooth (left and middle-left) and rough (middle-right and right) compact columns with refractive index 1.31 + 0i. The upper and lower rows of polar plots correspond to the forwards and backwards scattering, respectively, as depicted in the schematic of Figure 5.1. The particles and their orientations as viewed along the direction of incidence are shown for reference.

many of the key features seen in the DDA results. However, the accuracy decreases towards the backscattering, which indicates room for improvement in the near-field computation for non-absorbing particles as seen here.

The 1D phase function results for 3 sets of refractive indices in the same orientation are shown in Figure 5.3. The phase function for absorbing particles are shown in the 2$^{\text{nd}}$ and 3$^{\text{rd}}$ rows of Figure 5.3. For the roughened particle geometries, a comparison with GO is included. The residual σ is computed using $\sigma = (S_{ij}^{(pbt)} - S_{ij}^{(dda)})$, and the normalised residual $\overline{\sigma}$ is given by $\overline{\sigma} = \sigma / S_{ij}^{(dda)}$, where S_{ij} corresponds to an element of the Mueller matrix. For the smooth, non-absorbing particle, the PBT results show exceptional agreement in the forward scattering, with a mean normalised residual of 2% for $\theta < 60°$. For the rough, non-absorbing particle (upper-right in Figure 5.3), the PBT method shows a particular improvement over GO in the region $\theta \approx 60°$, which increases the accuracy of the asymmetry parameter. For the weakly (n =1.31+0.01i) and strongly absorbing (n =1.31+0.1i) particles, the PBT overestimates the side-scattered intensity at $\theta \approx 90°$, which could be a limitation of the surface integral diffraction method employed. Nonetheless, the effect of this on the

asymmetry parameter should be small, and therefore the impact on application should be limited. For the weakly absorbing particles, the PBT shows an overestimation in the back-scattered intensity, which is likely due to an oversimplification of the propagation of light as a coherent plane wave in lossy media. In fact, the light is known to propagate as an incoherent plane wave in this case [40, 100], which is not fully accounted for in this model; as discussed in Section 3.4.3, the incoherent plane wave propagates with planes of constant phase perpendicular to the propagation direction (as is done in the PBT method), but with planes of constant amplitude perpendicular to the surface normal, which is not accounted for [86]. For the strongly absorbing particles, the scattering is dominated by external diffraction combined with external reflection. The PBT overestimates the side-scattering for rough absorbing particles. It is thought that a more accurate results could be achieved by improving the near-field approximation, particularly at areas of the surface occluded by the roughness.

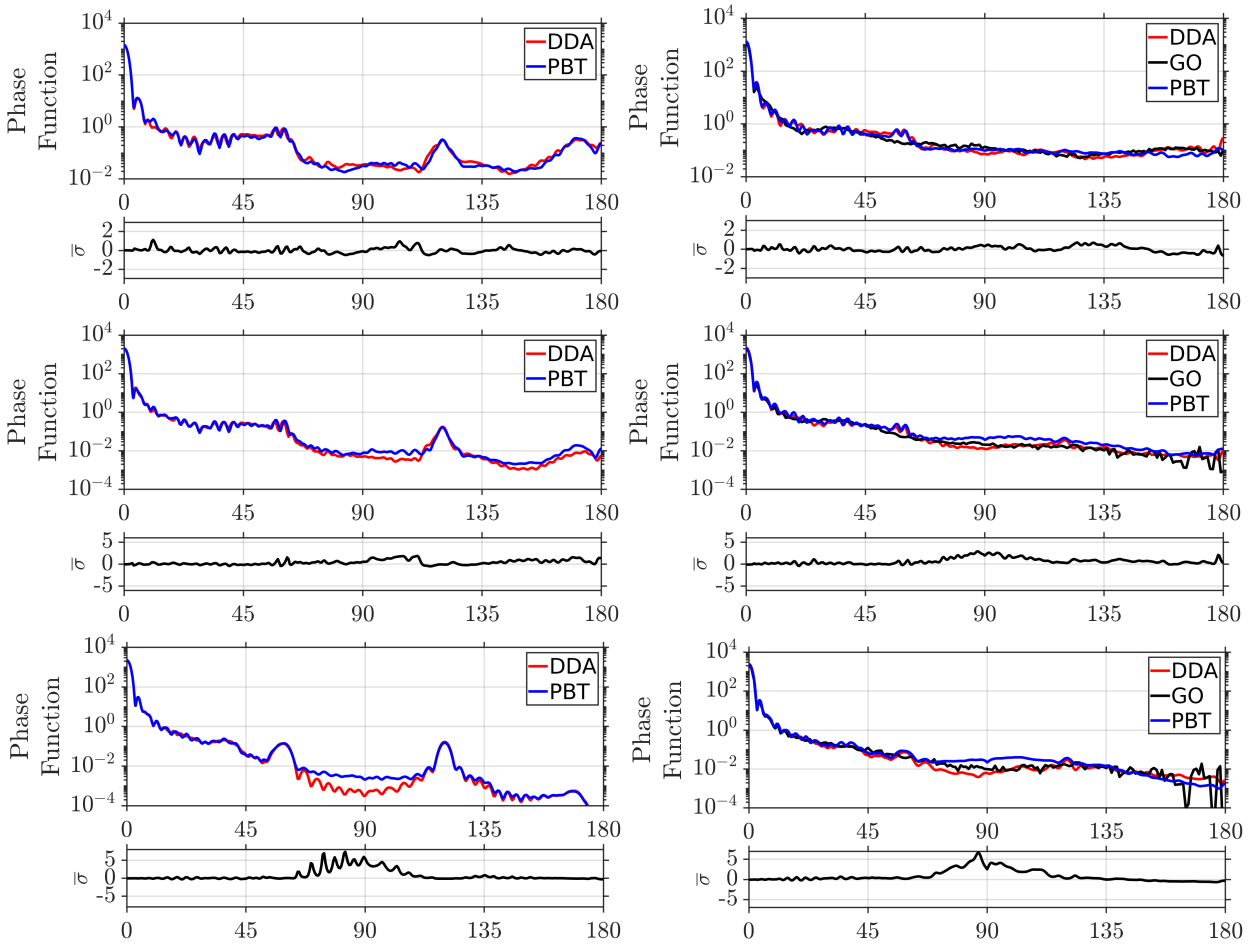

Figure 5.3: The 1D phase function for smooth (left) and rough (right) compact columns. Rows correspond to refractive indices 1.31 + 0i, 1.31 + 0.01i, and 1.31 + 0.1i, respectively. The particle orientation is the same as shown in Figure 5.2.

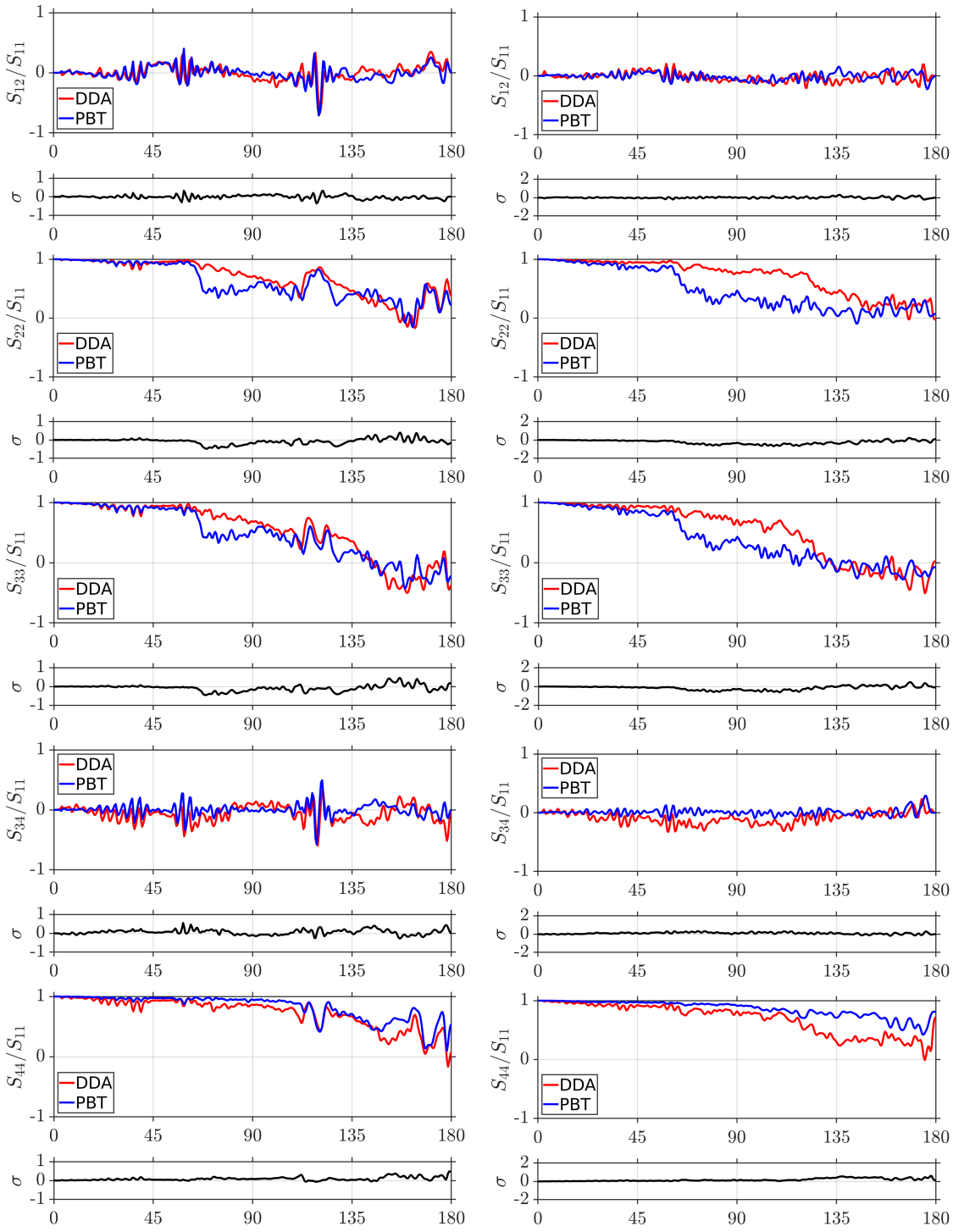

Figure 5.4: Other elements of the Mueller matrix for smooth (left) and rough (right) compact columns with refractive index 1.31 + 0i in the same orientation as shown in Figure 5.2.

5.2 Hexagonal Ice Plates with Stochastic Surface Roughness Benchmark

One of the difficulties encountered in quantifying the radiative effect of cirrus is due to the diverse variety of geometries of ice crystals found in cirrus. Of these, the hexagonal ice plate and its aggregates are known as a dominant species and therefore has a significant effect on the cloud bulk scattering properties [12]. In recent years, extensive work has been undertaken to compute the single scattering parameters of pristine and distorted ice plates at a wide range of size parameters. However, the role of surface roughness and how it affects the scattering as opposed to smooth surface particles remains relatively poorly understood.

The work described in this section aims to advance current understanding by investigating the scattering properties of ice plates with surface roughness. A versatile implementation of surface roughness designed for application to faceted particle geometries is introduced in Section 5.2.1. The roughness is defined by a characteristic length scale and an amplitude, which is used to produce a variety of hexagonal ice plates with aspect ratio 10. The quasi-orientation averaged scattering parameters are obtained by rotating the particles into 96 carefully selected orientations and is described in Section 5.2.1. The ice plates are chosen with a size larger than the wavelength, which permits the use of the DDA method, as well as the PBT method. Finally, the results are discussed in Section 5.2.3.

5.2.1 A Simple Implementation of Surface Roughness

A simple yet versatile implementation of surface roughness is used, which allows both the length scale and amplitude of the roughness to be varied. This method was briefly discussed in Section 4.2. The particle is initially constructed as a hexagonal prism, comprised of 8 facets (2 basal and 6 prism facets). The plate has an aspect ratio of 10, with a plate radius 10.186 µm and thickness 2.037 µm, which gives a volume-equivalent size parameter $2\pi r/\lambda = 60$, where r is the radius of the volume-equivalent sphere. The ice material is defined through the refractive index $n = 1.31 + 0i$ for a wavelength of light $\lambda = 0.532$ µm. Each facet is then subdivided using a Delaunay triangulation technique [114]. After triangulation, the vertices of the mesh are displaced by some random value along the axis of the facet normal. The process is illustrated in Figure 5.5. The triangulation method allows the maximum edge length L to be enforced, which provides a way of setting an approximate length scale of the roughness. Larger values of maximum edge length generally give rise to coarser meshes, and smaller values give rise finer meshes. Since this approach merely sets some maximum value on the edge length, it cannot be ensured that this length scale remains constant across the entire geometry. The approach is a compromise between improved versatility but reduced uniformity. It can be applied to almost any surface mesh represented by planar faces with reasonable stability. However, if the particle contains facets with length dimensions smaller than the chosen maximum edge length, then the edges of the resulting mesh can be smaller than intended. The displacement of each vertex is capped by some maximum value σ, which determines the effective amplitude of the roughness. A value of 0 applies no displacement, which preserves the smooth surface, whereas larger maximum values increase the roughness amplitude. In this study, L is varied in steps of $\lambda/2$ from $\lambda, \frac{3\lambda}{2}, \cdots, 3\lambda$. Maximum edge

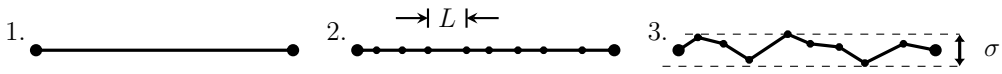

Figure 5.5: Simplified schematic showing the sequence of steps taken to create the surface roughness. 1) A surface before triangulation. 2) A surface after triangulation with maximum edge length L. 3) A triangulated surface after displacement, capped by the roughness amplitude σ in either direction normal to the original surface.

lengths smaller than the wavelength are excluded, since the number of dipoles needed to sufficiently resolve features at this length scale rapidly increases the computational demand of the DDA method. The value of σ is varied in steps of $\lambda/5$ from $0, \frac{\lambda}{5}, \cdots, \lambda$. Example particle geometries for roughness amplitude $\lambda/5$ with different maximum edge lengths are shown in Figure 5.6, and example particle geometries for maximum edge length λ with different roughness amplitudes are shown in Figure 5.7.

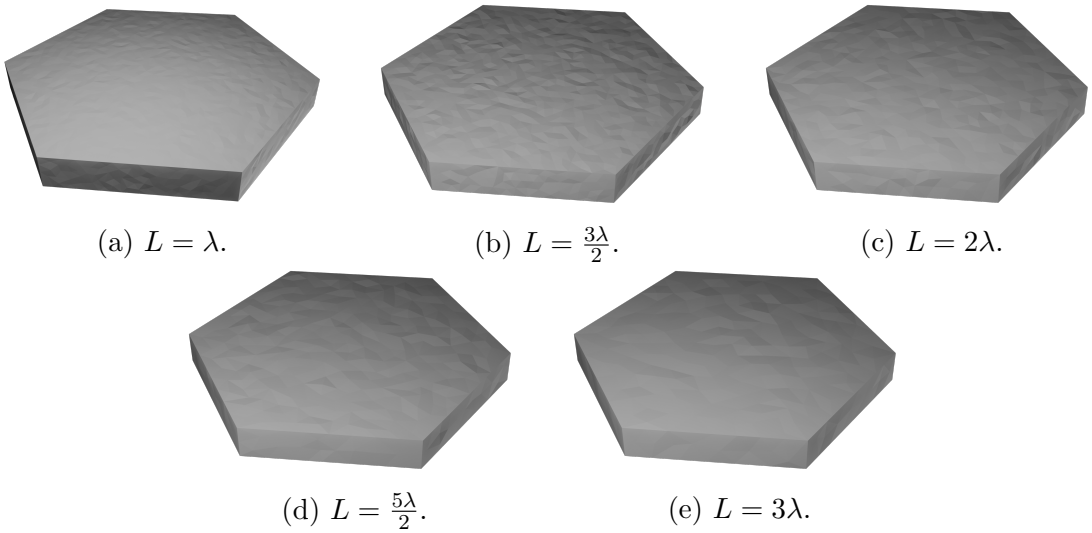

(a) $L = \lambda$. (b) $L = \frac{3\lambda}{2}$. (c) $L = 2\lambda$.

(d) $L = \frac{5\lambda}{2}$. (e) $L = 3\lambda$.

Figure 5.6: Examples of different plate geometries with varying maximum edge lengths, $\sigma = \lambda/5$.

Particle Orientations

Since DDA computations at this size parameter are time consuming, it is not possible to average over large numbers of particle orientations. Therefore, a compromise is made whereby the scattering is averaged over a small number of uniformly distributed orientations. The "zyz" rotation convention as described in [117] is used here, which means that the first Euler angle α determines the initial rotation about an axis aligned with the incidence direction. In this case, α has no effect on the θ-dependence of the scattering and can be set to 0° if only the 1D scattering is important. Typically, the Euler angles are computed in radians using $\beta = \arccos(1 - 2X)$, and $\gamma = 2\pi X$, where X is a number in the range $0 \leq X < 1$. For hexagonal prism-shaped particles, the range of the β and γ Euler angles can be reduced due to the symmetry of the particle geometry. This allows the orientation averaged scatter-

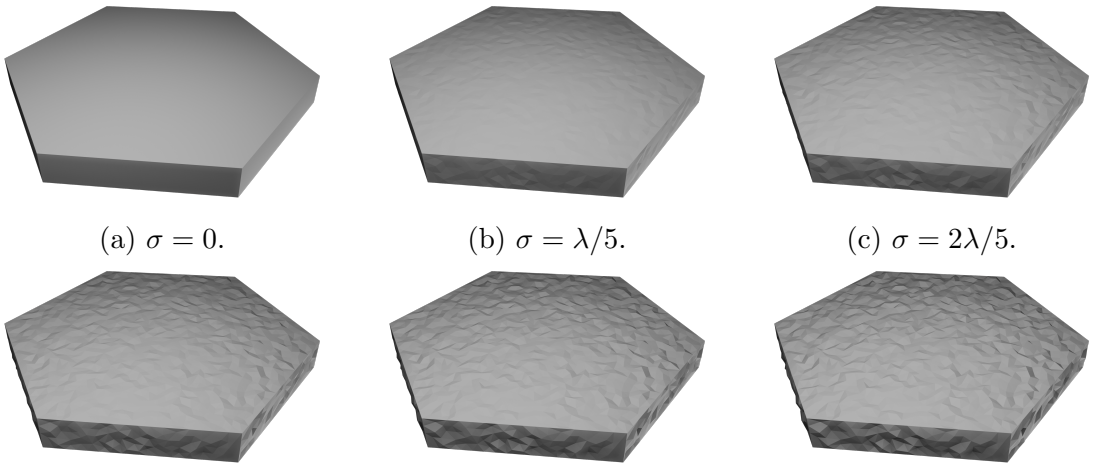

(a) $\sigma = 0$. (b) $\sigma = \lambda/5$. (c) $\sigma = 2\lambda/5$.

(d) $\sigma = 3\lambda/5$. (e) $\sigma = 4\lambda/5$. (f) $\sigma = \lambda$.

Figure 5.7: Examples of different plate geometries with varying roughness amplitudes, $L = \lambda$.

ing to be more quickly approximated compared to a Monte Carlo-based approach. For this rotation convention, with the hexagonal plate initially aligned with the prism axis along the incidence direction, the geometry is symmetric about $\beta = 90°$ and repeats every 60° in γ. The angles are therefore determined by confining X to the range $0 \leq X < 0.5$ for β and $0 \leq X < 1/6$ for γ. A diagram showing how the angles β and γ determine the orientation of the plate is shown in Figure 5.8. The chosen implementation of surface roughness means that the particle is no longer perfectly symmetric in γ. This falls within ensemble variation, which could be accounted for by additionally averaging over several random realisations of the surface roughness. In this study, it is assumed that the maximum edge length is small enough so that enough mesh elements are present to remove any significant asymmetry without considering ensemble averaging. In summary, the following limits and values for Euler

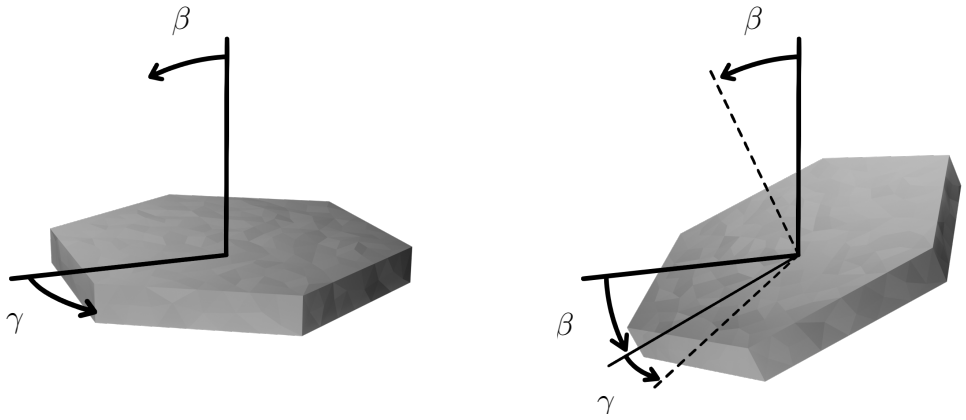

(a) Particle before rotation. (b) Particle with rotation $\beta = 25°$, $\gamma = 25°$.

Figure 5.8: Diagram showing how the hexagonal plate particle is oriented according to the chosen Euler angles.

angles are used to reduce the number of orientations:

1. $\boldsymbol{\alpha = 0°}$.
2. $\mathbf{0° < \beta < 90°}$, β = 10.1°, 22.8°, 30.8°, 37.2°, 42.8°, 47.8°, 52.5°, 56.9°, 61.0°, 65.1°, 68.9°, 72.7°, 76.5°, 80.1°, 83.7°, 87.3°.
3. $\mathbf{0° < \gamma < 60°}$, $\gamma = 0°$, 10°, 20°, 30°, 40°, 50°.

5.2.2 Numerical Methods

Two different numerical methods are used to compute the scattered field from the hexagonal ice plates. These are the DDA (Section 3.3) and PBT (Section 4) methods. The accuracy of the DDA method has been well studied, and the error in fulfillment of reciprocity in some tests has been shown to be less than 10^{-5}% [96]. In this work, the ADDA code is used [62], which recommends as a rule-of-thumb that the spacing between dipoles d should satisfy $d < \lambda/10m$, where λ is wavelength, and n is the particle refractive index. For this study, $\lambda = 0.532$ µm and $n = 1.31 + 0i$, so it is chosen that $d = 0.0406$ µm. Furthermore, users of the ADDA code are recommended to ensure at least 10 dipoles are present per characteristic length of the particle geometry [118]. Therefore, the minimum value for maximum edge length is set to $L = \lambda$ so that, in most cases, a sufficient number of dipoles are used to accurately represent the surface roughness. A mesh conversion code which uses a quick sort algorithm is used to construct the dipole arrays for these complex particle geometries [113]. The results from the DDA method here are generally considered as the numerical reference data against which the accuracy of the PBT method is measured. The ADDA code is run with numerical solver `-iter bcgs2` as described in the ADDA user manual [118].

5.2.3 Results & Discussion

Discrete Dipole Approximation

First, the results from the DDA method for variation in roughness are discussed. The phase functions normalised to 1 for $L = 1$ and $L = 3$ are shown in Figures 5.9a and 5.9b, respectively. The reader should refer to Figure 5.7 for the particle geometries. In general, it can be seen that averaging over the 96 orientations removes most of the fixed-orientation features that might be expected due to specific beam paths. The remaining features include the forward scattering peak discussed in Section 5.1.2, a broad halo peak at $\sim 22°$, and a backscattering peak. Several sharp peaks across the scattering angle range can be seen, which can be attributed to the finite number of chosen β angles and an interference effect similar to that observed in thin films. The interference occurs when an externally reflected beam interferes with an internally reflected one, as shown in Figure 5.11a. The angular position of each peak is simply related to β by the law of reflection. For example, the first value of $\beta = 10.1°$ corresponds to the first interference peak at $180 - 2(10.1) = 159.8°$. In general, the relative heights of each peak depend on the phase difference between the two beam paths, the Fresnel equations of reflection and transmission, and the projected cross sectional area. The phase difference is a function of the dimensions of the plate, as well as the wavelength of incident light.

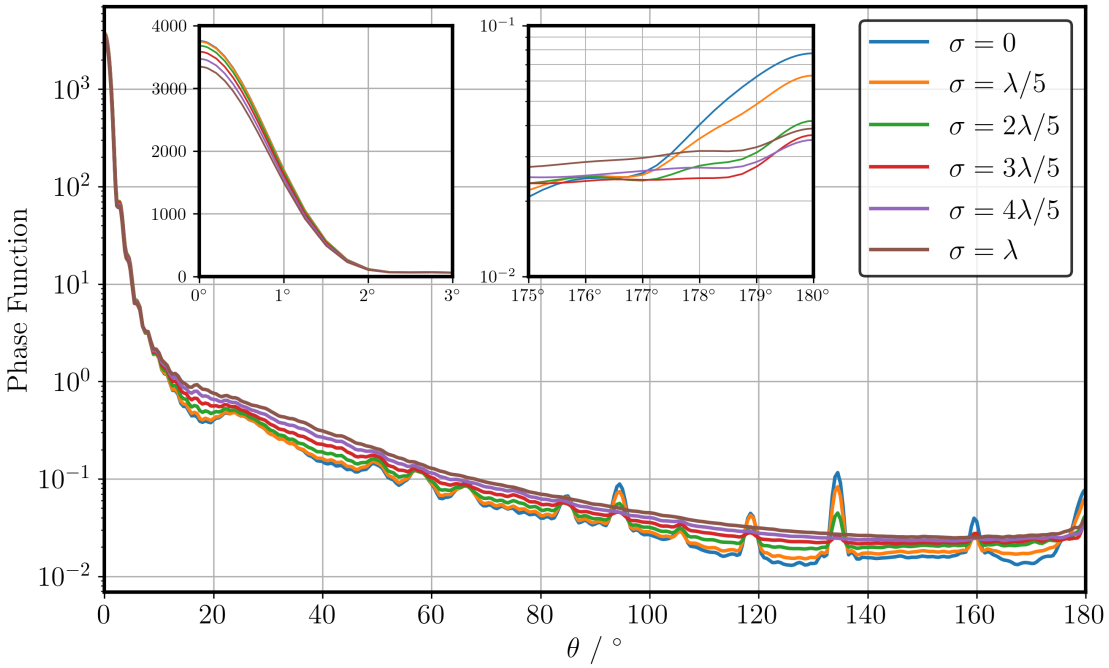

(a) Maximum edge length $L = \lambda$.

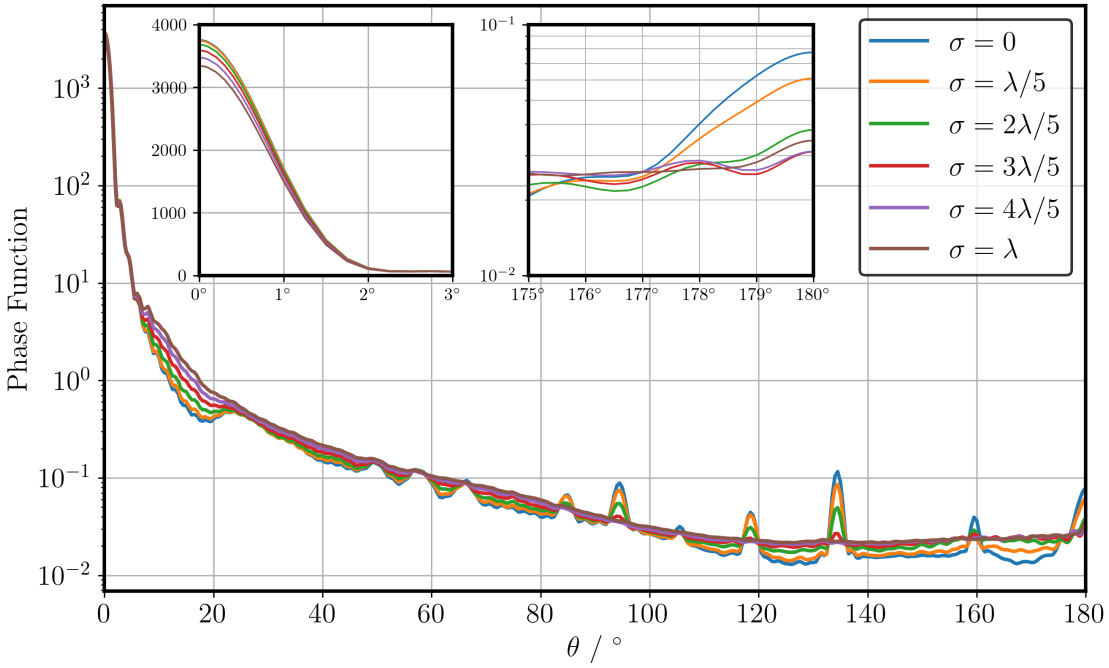

(b) Maximum edge length $L = 3\lambda$.

Figure 5.9: Normalised phase function for hexagonal ice plates with varying amplitudes of surface roughness. Results are computed with the DDA method. Close to the direct forwards scattering on a linear scale is shown in the upper left inset. The backscattering region is shown in the upper right inset. Parametric sweeps at $L = \lambda$ and $L = 3\lambda$ are shown in 5.9a and 5.9b, respectively.

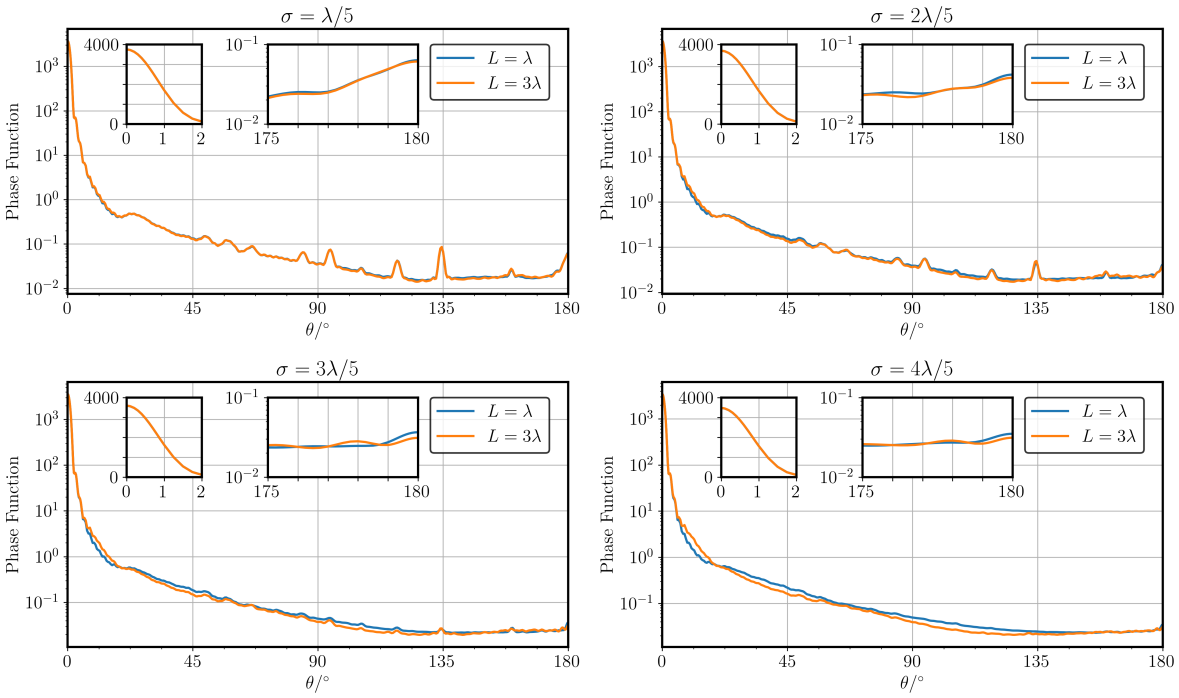

Figure 5.10: Comparisons of the normalised phase function for hexagonal ice plates with varying amplitudes at different roughness amplitudes. Results are computed with the DDA method. Close to the direct forwards scattering on a linear scale is shown in the upper left inset. The backscattering region is shown in the upper right inset.

1. **Close to Direct Forward Scattering:** The scattered intensity close to $\theta = 0°$ is shown in the upper left inset of the figure. A linear scale is used in the upper left insets here, since small fractional differences have a significant effect on the asymmetry parameter. It is found that, at this size parameter, the smooth plate $\sigma = 0$ has the strongest forward scattered intensity, while increasing values of σ result in smaller amplitudes. Interestingly, the data shows that scattering by particles with $\sigma = 0$ is almost indistinguishable to those with $\sigma = \lambda/5$. In summary, the data suggests that surface roughness has almost no effect on the forward scattering if $\sigma << \lambda$.

2. **Halo Region:** The broad halo peak centered at $\sim 22°$ can be attributed to the angle of minimum deviation associated with light passing between 2 non-adjacent rectangular facets of the plate [28]. The relative height of this peak, known as the halo ratio, can be defined as $p_{11}(\theta = 23°)/p_{11}(\theta = 20°)$. The value of the halo ratio has been proposed as a quantitative measure for identifying the presence of cirrus [119]. Compared to computations with geometric optics (eg. [35, 89]), the 22° halo observed here is broader and relatively weak. The height of this peak can be explained by the large aspect ratio of the plate. More columnar type ice particles have larger rectangular facets, which in turn leads to a larger fraction of the incident energy being scattered into the halo region. The broadness of the peak is due to the fact that the prism facets have dimensions comparable to the wavelength. This leads to a significant broadening of scattering due to diffractive effects, which cannot be accounted for with classical geometric optics. Similar to the findings of the direct forwards scattering, the halo region is almost unaffected by the presence of surface roughness with amplitude much smaller than the wavelength. The halo peak diminishes as the roughness increases up until $\sigma \approx \lambda$, wherein the peak is no longer distinguishable, which agrees with the findings of other studies [65, 120, 121]. This finding has implications for practical applications which use the halo region as a means of identifying the presence of ice particles. The results show that the absence of a distinguishable halo peak does not necessarily mean that there is an absence of hexagonal ice plates in the sample. Rather, it merely indicates the absence of pristine hexagonal prisms. This agrees with other studies, which have found that classical geometric optics overestimates the intensity of the 22° halo peak [38, 79]. Further incorporation of the halo ratio in measuring techniques could provide as a useful method of estimating surface roughness and irregularity, especially when combined with analysis of other experimental evidence such as scattering pattern symmetry and particle imaging.

3. **Backscattering:** The backscattering in the region $\theta = 175$-$180°$ is shown in the upper right insets of Figure 5.9. Unlike for the forward scattering and 22° halo regions, even small scale roughness appears to have an effect on the backscattering. As may be expected, the smooth hexagonal plate ($\sigma = 0$) shows the strongest backscattering peak. Due to the normalisation of each phase function and the difference in scattering cross sections between datasets, comparing the values at $\theta = 180°$ does not provide a very useful insight. Instead, the backscattering ratio is introduced, which is defined here as $p_{11}(180°)/p_{11}(175°)$. The backscattering ratios for increasing values of σ at $L = \lambda$ are found to be 3.74, 2.86, 1.76, 1.56, 1.41, 1.42. Increasing the amplitude of

surface roughness decreases the backscattering ratio until a value of ~ 1.4, where it appears to asymptote. Recent studies indicate that two main factors contribute to the backscattering ratio: corner retro-reflection events [39] and coherent backscattering [122]. A retro-reflection can occur when a particle with multiple right-angled facets is illuminated at certain ranges of orientations. Under these conditions, there exist bundles of parallel ray paths which can be shown using geometric optics to scatter into the direct backscattering direction. One possible explanation for the decreasing backscattering ratio is that, as the roughness amplitude increases, the effect of retro-reflection events is reduced, and therefore the backscattering ratio becomes primarily due to coherent backscattering. The effect of coherent backscattering is a well known wave phenomenon that leads to constructive interference in and close to $\theta = 180°$. The effect can be explained by studying a pair of reciprocal ray paths as shown in Figure 5.11b. If an incident ray undergoes multiple scattering events and is scattered back along the direction of incidence, then there exists a reciprocal ray which travels along the exact same path but in the opposite direction. This follows as a result of the time-reversal symmetry of Maxwell's equations. Consequently, the 2 rays travel the same distance and therefore always interfere constructively in the direct backscattering, which leads to a peak in the backscattered intensity. Even without consideration of the phase of the electric field, classical geometric optics often overestimates the backscattering ratio for pristine hexagonal prisms due to the omission of diffraction of outgoing bundles of rays.

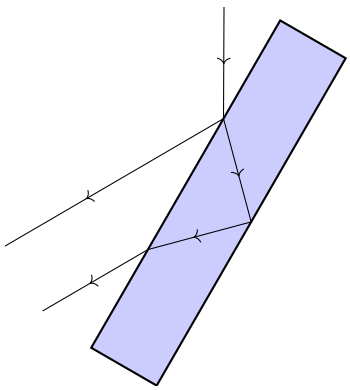

(a) Plate interference effect, whereby the interference between external reflection and an internally reflected beam path gives rise to the varying peaks across the phase function for orientation averaged hexagonal ice plates.

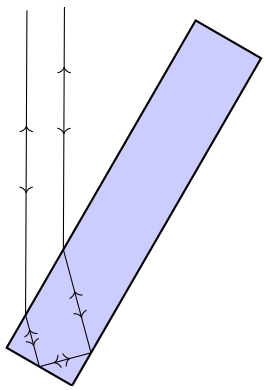

(b) An example of a reciprocal ray pair, which traverse the same path in opposite directions. This example shows a corner retro-reflection, which provide a large contribution to the backscattering of particles with prism [123] geometries.

Figure 5.11: Important ray paths in scattering by hexagonal ice plates.

As σ increases to values comparable with λ, the transition region between forward scattering and the halo region is affected and a secondary maximum in the backscattering (at $\theta \approx 178°$) becomes more prominent. The DDA results for variation of the maximum edge length at roughness amplitude $\sigma = \lambda/5$ are shown in Figure 5.12. The reader should refer to

Figure 5.6 for the corresponding particles geometries. The DDA results show almost no

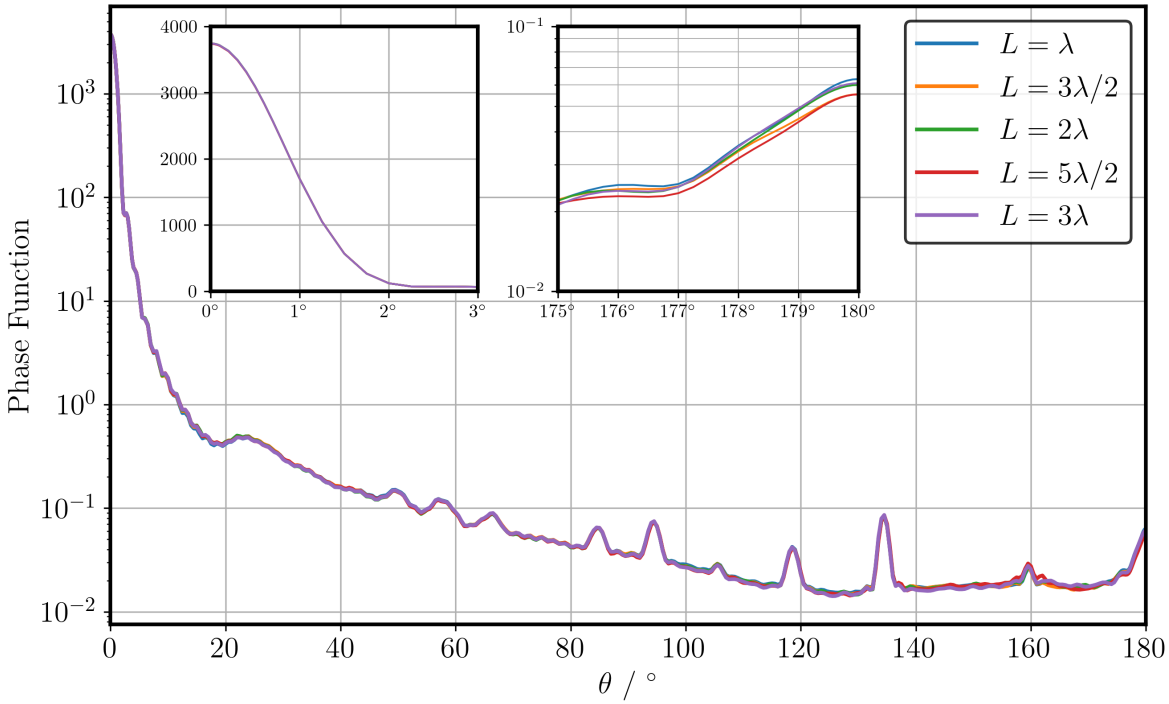

Figure 5.12: Normalised phase function for hexagonal ice plates with varying maximum edge length of surface roughness and roughness amplitude $\sigma = \lambda/5$. Close to the direct forwards scattering on a linear scale is shown in the upper left inset. The backscattering region is shown in the upper right inset.

effect on the orientation averaged scattering due to variation in maximum edge length. The only discernible differences arise towards the backscattering, when $\theta > 150°$. There are small differences in the shape of the peak at $\theta = 160°$, and the upper right inset of Figure 5.12 highlights minor differences in the direct backscattering. The backscattering ratios as defined previously for increasing maximum edge length are 2.86, 2.50, 2.74, 2.58, and 2.88. Therefore, it is concluded that changing the maximum edge length has almost no effect on the scattering when the amplitude of roughness is much smaller than the wavelength. By combining the plots in Figures 5.9a and 5.9b, direct comparisons showing the effect of increasing the maximum edge length at different roughness amplitudes can be made. The comparisons are shown in Figure 5.10. The upper left and right subplots show that almost identical orientation averaged scattering is predicted by the DDA method for $\sigma = \lambda/5$ and $\sigma = 2\lambda/5$ at each of the maximum edge lengths. The phase function is practically invariant with respect to L for $\sigma < \lambda/2$, and even for larger values of σ the effect of L can be considered minor. Therefore, it can be said with some certainty that the characterisation of surface roughness of ice plates can be based solely on the amplitude of the roughness, so long as the amplitude is smaller than the wavelength. Another study found an effective equivalence between surface roughness and irregular geometries by relating the surface tilt angle to a distortion factor [42]. The findings of this work do not fully agree with this equivalence because varying the maximum edge length while keeping the roughness amplitude constant

is equivalent to decreasing the surface tilt angles. The results presented here suggest that this should not significantly affect the orientation averaged scattering. Further work is needed to incorporate the resolution of the mesh into the equivalence between tilt angle and particle distortion. Furthermore, work is needed to determine if the length-scale invariance found in this study can be extended all the way to distorted, smooth geometries.

PBT Results vs DDA

Second, the results for the PBT against the DDA method for each particle are shown in Figure 5.13. Overall, the accuracy of the PBT is best when the particle is smooth and decreases

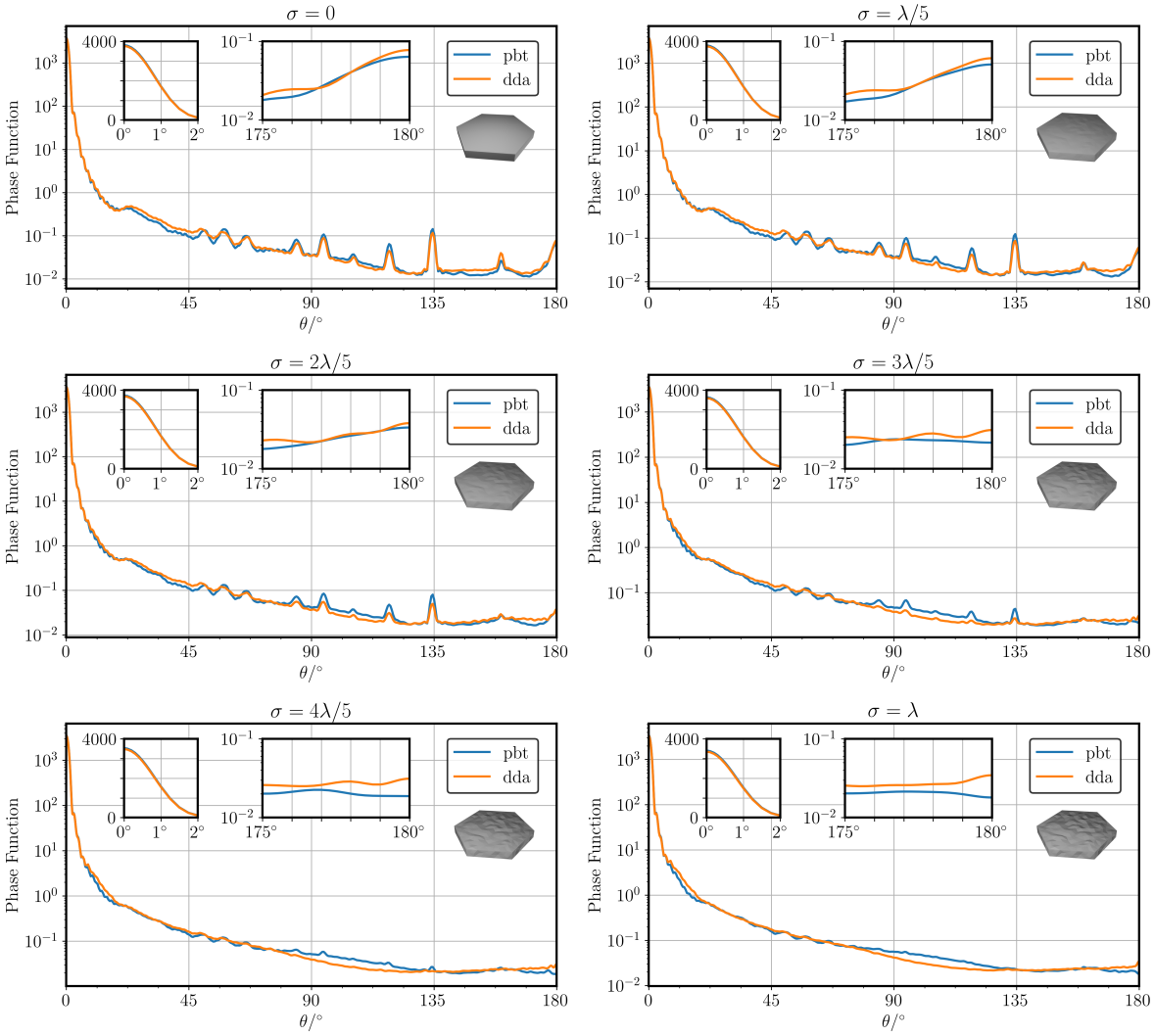

Figure 5.13: Comparisons of the normalised phase function for hexagonal ice plates with varying amplitudes of surface roughness and maximum edge length $L = 3\lambda$. Close to the direct forwards scattering on a linear scale is shown in the upper left inset. The backscattering region is shown in the upper center inset. For reference, each particle is shown as an inset.

with the amplitude of the roughness. This is to be expected, since geometric optics is less accurate in regions where the characteristic length scale is comparable to, or smaller than the wavelength. It has been pointed out that, the geometric optics field is overly sensitive with respect to perturbations in the parameters of the medium [23], which in this case correspond to the fluctuations in the surface topology. For the smooth particle ($\sigma = 0$), the PBT method shows generally good accuracy at all scattering angles. The error in the direct forwards ($\theta = 0°$) scattering is +1.23% and in the direct backscattering ($\theta = 180°$) is -18%. One explanation for the underestimation in the backscattering is that this region is highly sensitive to the effects of coherent backscattering. Since the hexagonal plates used here have only a size parameter of 60, the contribution from the edge and corner effects may be significant. The sharp right-angled edges used for the hexagonal plates effectively have an infinitely small radius of curvature. Therefore, traditional GO cannot be expected to capture the physics of field propagation in these regions and extensions to geometrical theory of diffraction are needed [36, 124]. Of course, it is generally assumed that neglecting such contributions becomes more acceptable with increasing size parameter. For light roughness ($\sigma = \lambda/5$), the PBT maintains a reasonable accuracy compared with the DDA. The prediction of the forward scattering peak has an error of -2.57%, the halo region closely resembles the DDA method, and a peak in the direct backscattering is well predicted. Errors in the side scattering ($\theta \sim 90°$) start to become prevalent, which is believed to be a sensitivity of the surface integral method for diffraction and has been recognised in the literature [125]. The PBT accuracy decreases significantly for $\sigma > 2\lambda/5$. For example, as shown in the upper right insets of Figure 5.13, the DDA predicts a small peak with backscattering ratio ~ 1.4, but the PBT method shows almost no backscattering peak in this region. Nonetheless, the PBT method shows a promising ability to reproduce the main features of the phase function, even with increasing roughness. The time taken to compute the scattering in each orientation is ~ 500 CPU hours for the DDA method, versus ~ 1 CPU hour for the PBT method. It should be noted that the relative computational speedup is expected to increase rapidly with size parameter (the plates were scaled to a volume-equivalent size parameter of 100, but in this case the DDA method failed to reach convergence).

Next, PBT results compared with those of the DDA method for variation in maximum edge length for $\sigma = \lambda/5$ are shown in Figure 5.14. Overall, the agreement between the PBT and the DDA methods is good across all the length scales tested, although the accuracy improves as the maximum edge length increases beyond the wavelength. For smaller values of L, the PBT tends to overestimate side scattering, which can be seen in the upper left of the Figure 5.14. The computed values for asymmetry parameter g are summarised in Figure 5.15. DDA results indicate a weak decrease in asymmetry parameter with increasing roughness amplitude. The effect of maximum edge length is small for small roughness amplitudes but becomes more significant as the roughness amplitude becomes comparable to the wavelength. In any case, surface roughness with scale comparable to the wavelength only appears to affect the asymmetry parameter by at most, a few %. The figure shows that the PBT method is most accurate for longer maximum edge lengths. Since the DDA method predicts that the scattering is mostly insensitive to the maximum edge length, it can be concluded that the PBT can accurately model surface roughness by setting the maximum edge length to several times the wavelength. Based on these conclusions, it is proposed that the best approach to modelling surface roughness with the PBT method may be to first, quantify the

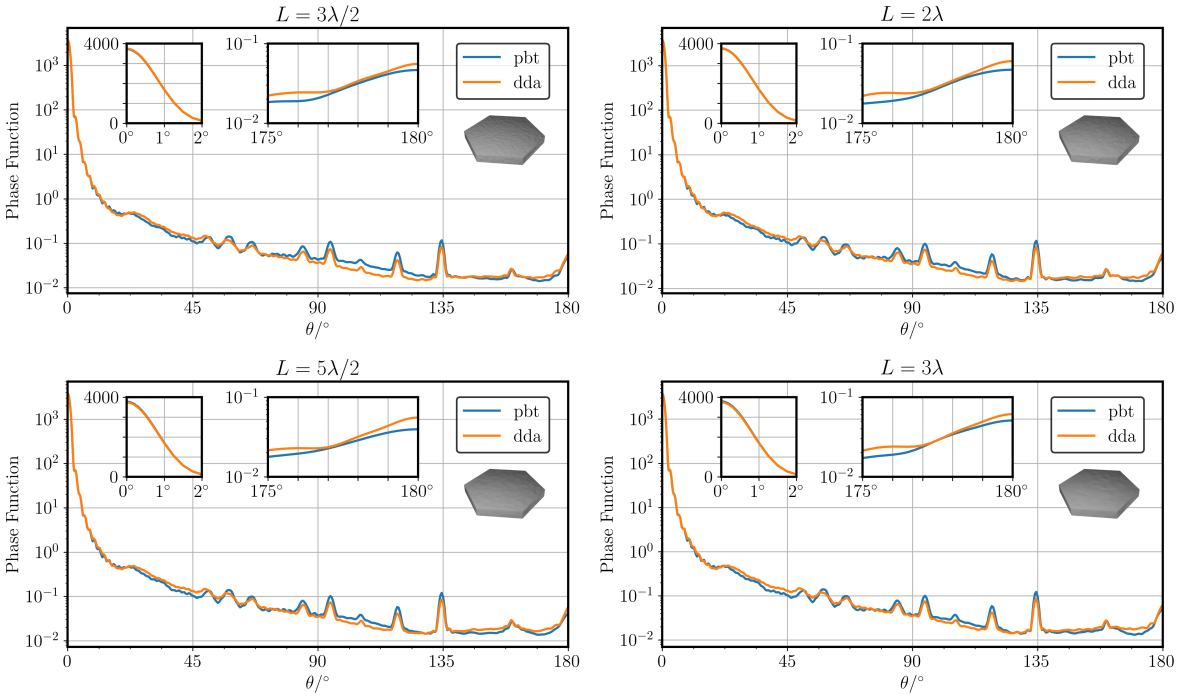

Figure 5.14: Comparisons of the normalised phase function for hexagonal ice plates with varying maximum edge lengths of surface roughness with amplitude $\sigma = \lambda/5$. Close to the direct forwards scattering on a linear scale is shown in the upper left inset. The backscattering region is shown in the upper center inset. For reference, each particle is shown as an inset. For the case of $L = \lambda$, the reader is referred to the upper right subplot of Figure 5.14.

amplitude of the roughness, and then second, choose a suitable maximum edge length that is several times larger than the wavelength. Then, based on the finding that the scattering is mostly invariant with respect to maximum edge length, the PBT method should be a valuable tool capable of predicting various integrated scattering parameters in a relatively small amount of required computation. The computed values for scattering cross section

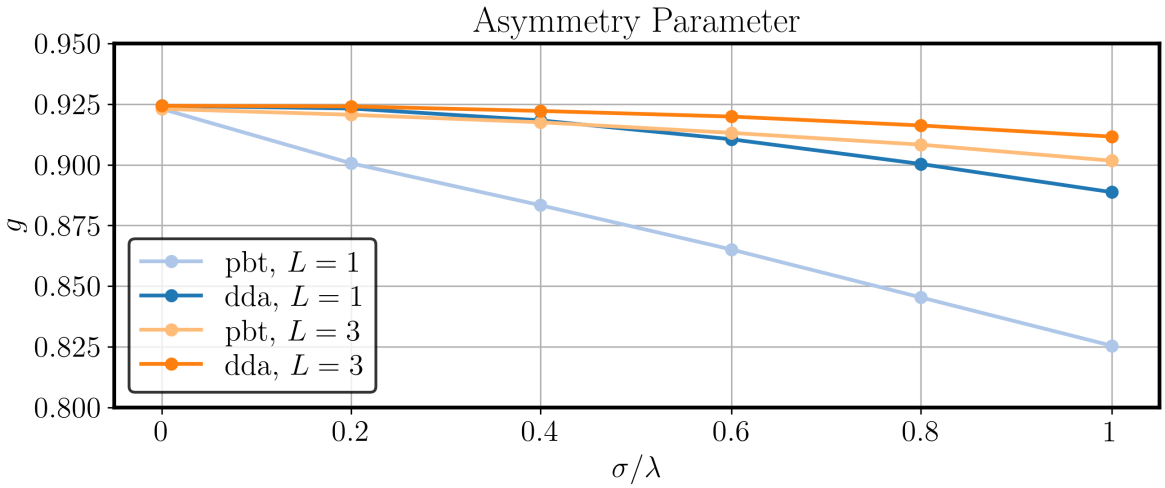

Figure 5.15: Comparison of the asymmetry parameter at each maximum edge length and roughness amplitude for the PBT and DDA methods.

σ_{scat} are summarised in Figure 5.16. As previously discussed, the DDA method predicts that the variation of scattering cross section with increasing roughness amplitude is mostly invariant with respect to the maximum edge length. The PBT method shows poor accuracy for non-smooth surface at $L = 1$, but follows the trend of the DDA method at $L = 3$. At $L = 3$, the PBT method is accurate to within $\sim 3\%$.

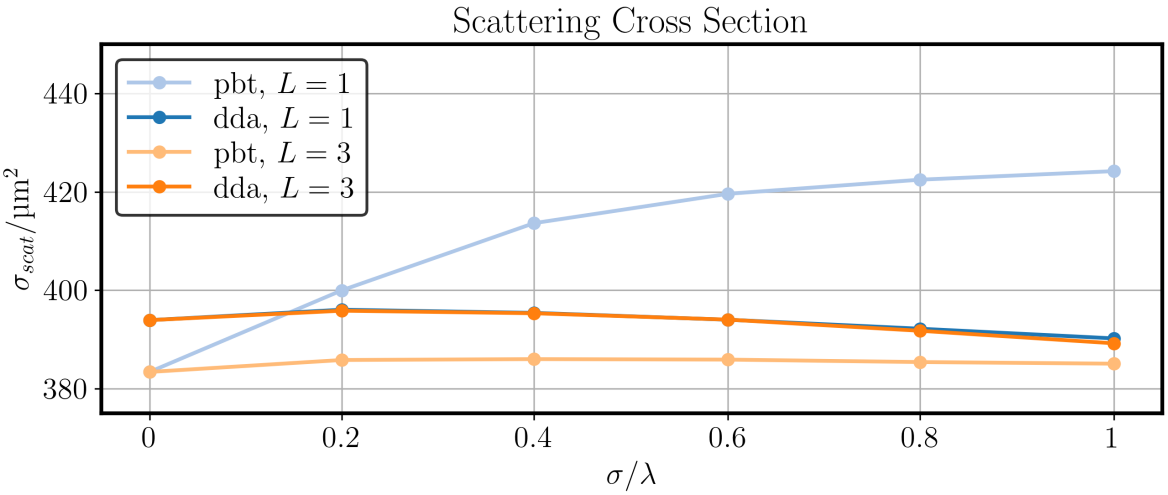

Figure 5.16: Comparison of the scattering cross section at each maximum edge length and roughness amplitude for the PBT and DDA methods.

5.3 Scattering Parameters of Hexagonal Ice Plates

In this section, the results of an investigation into the single scattering properties of hexagonal ice plates are discussed. The plate aspect ratio defined by the ratio of thickness to diameter is $5/80 = 0.0625$. The plate diameter is varied from 55 to 95 µm in steps of 10 µm. For each plate size, light scattering is computed for 30 wavelengths in the range 0.2 to 5 µm. This wavelength range is required for ice optical parametrisations of cirrus clouds for radiative transfer computations. The wavelength-dependent refractive index of ice has been well studied [126] and is shown for this wavelength range in Figure 5.17. An ensemble of experimental procedures were used to measure the imaginary part, and the regions of minimum absorption were then used alongside Kramers-Kronig relations to infer the real part. In the visible region, absorption is low and the real part is ~ 1.31, whereas for the infrared region, absorption is much higher and there is an inflection in the real part around 3.1 µm (see Figure 5.17). The PBT method was used to compute the single-scattering for each particle

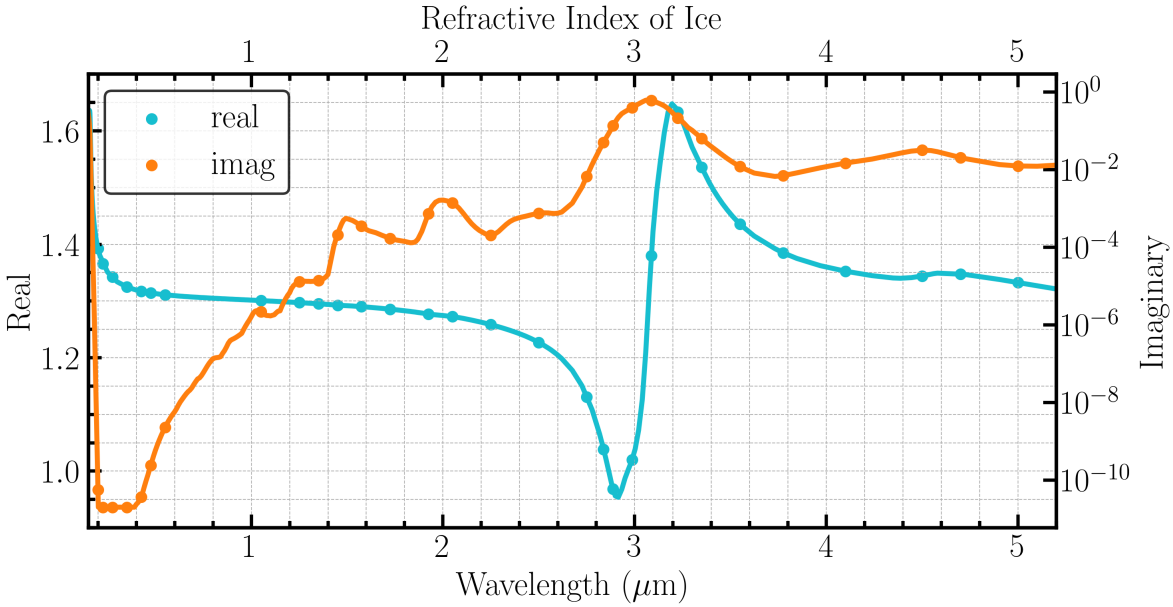

Figure 5.17: Refractive index of ice [126]. Real part is on the left axis and imaginary part is on the right axis.

size and wavelength combination. The results are shown in Figure 5.18. The upper portion of Figure 5.18 shows that the single scattering albedo is largely dependent on the refractive index, particularly for wavelengths smaller than 3 µm. By referring to Figure 5.17 (note the logarithmic scale), it can be seen that when the imaginary component is low, absorption is low and hence ω values are close to 1. The peak in absorption is at $\lambda = 3.088$ µm. As particle size increases, the internal path length traversed by transmitted beams increases. This causes an increase in absorption, leading to increased values of σ_{abs}, and therefore decreasing values of ω. The dominating factor in ω, however, is the refractive index. Extinction efficiency is shown in the middle section of Figure 5.18. It follows an oscillatory pattern asymptotic to a value of 2, which is in accordance with the well known extinction paradox. Diagonal bands

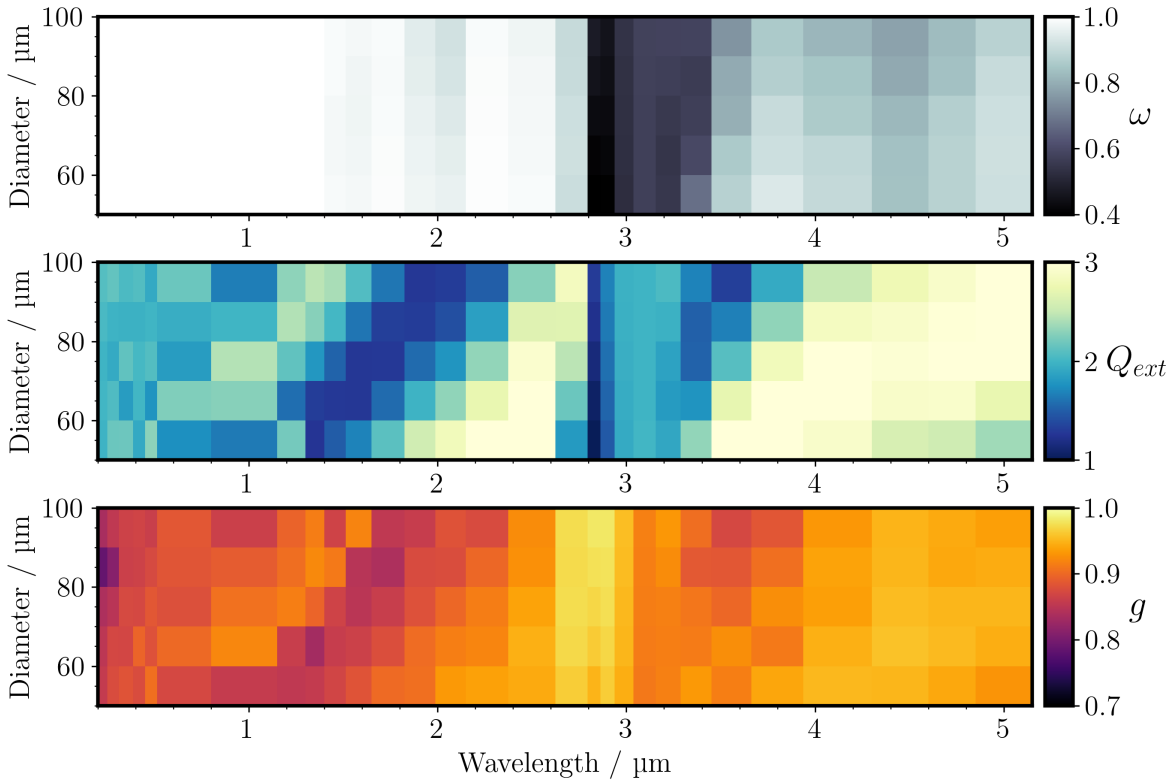

Figure 5.18: Thin plate single scattering parameters.

can be seen from lower left to upper right, which conform to the scale invariance rule [127]. In other words, the simulations show that extinction efficiency oscillates with size parameter. At the peak of absorption at $\lambda = 3.088$ ($n = 1.38005 + 0.606245i$), Q_{ext} takes values close to 2, since absorption and external diffraction remove approximately equal amounts of the incident light. It is interesting to observe a band of $Q_{ext} \sim 1$ for $\lambda = 2.838$ µm. At this wavelength, the refractive index is $n = 1.04 + 0.05i$. Further investigation into this finds that $\sim 60\%$ of light incident on the geometric cross section is removed due to absorption. The remaining scattered light is then scattered with an efficiency of $\sim 50\%$. This can be explained by the real part of the refractive index being ≈ 1. In this case, the particle is behaves indiscernibly from the surrounding medium, and hence scatters only very little light away from the forwards direction. The results for asymmetry parameter are shown in the lower section of Figure 5.18. Generally, values for g are consistently above 0.8, which is mainly dependent on the geometry. This is because the ice plate consists of 2 large, plane parallel basal facets, which allow a large fraction of the incident light to pass through the particle and be transmitted into the direct forwards direction. In the absorbing band at $\lambda \approx 3.1$ µm, g approaches values close to 1, since the scattering is dominated by external diffraction and external reflection. External diffraction is highly peaked in the forwards direction, and external reflection usually has much lower intensity in comparison. Comparison of g against Q_{ext} shows a positive correlation between the two parameters. For refractive indices with small imaginary components, the extinction is dominated by scattering. In this case, the asymmetry parameter is influenced by whether the external diffraction and trans-

mitted beams in or close to the forwards direction interfere constructively (increasing g) or destructively (decreasing g). However, when integrated over a particle size distribution, this effect is likely to have only a small effect.

Summary

In this section, the PBT method has been compared against the DDA method in 2 benchmark comparisons. In the first, the scattering for smooth and roughened hexagonal columns in fixed orientations at 3 different values for refractive index was computed. In the second, the orientation averaged scattering from hexagonal ice plates with varying surface roughness properties was compared. Interestingly, the DDA method showed that the scattering was largely independent of the correlation length of the roughness. The PBT method showed close agreement to the DDA when the roughness correlation length was several times the wavelength. The PBT method was then used to compute the orientation averaged scattering parameters for hexagonal ice plates across a range of particle sizes and wavelengths. In summary, this section provided an insight into the accuracy of the PBT method, as well as showing how it can be used as a valuable tool for bridging the gap between theoretical studies, experiment, and observational data. In the next chapter, a summary is given, which concludes this report.

Chapter 6

Summary

The main goal of this work has been to determine if a light scattering model based on GO could be devised, for the rapid accurate and rapid simulation of light scattering from particles with overall size much larger than the wavelength, but with physical roughness of length scale comparable to the wavelength.

In order to achieve this, Section 2 introduced the basic framework for electromagnetic theory, which describes how an incident plane wave interacts with a scatterer, leading to a redistribution of the wave's energy into multiple directions. The scattered field is represented by an outgoing spherical wave in the far-field, and its intensity and polarisation depend on the direction of observation. The Stokes parameters and Mueller matrices can be used to describe the state of the scattered field (at a given scattering angle) and the transformation from the incident to scattered field, respectively. Key integrated scattering parameters, such as asymmetry parameter, cross sections, and single scattering albedo, are defined, which are important for a broad range of applications.

In Section 3, just a few of the many current theoretical methods for light scattering were introduced. First, a brief theoretical derivation of the Lorenz-Mie theory for light scattering by spherical particles was given, which solves the vector wave equation by expanding the scattered field into a series of spherical harmonics. Second, a short overview of the T-Matrix method was described, which merits mentioning here owing to its widespread use in the literature. Third, the discrete dipole approximation was introduced. It is a versatile method that can be used for scatterers much larger than the wavelength of light, albeit with rapidly increasing computational demands. It is regarded as a numerically-exact method, with an accuracy that increases with increasing discretisation of the scatterer. For these reasons, it is a popular method, and it was used in this work as a numerical benchmark. The principles of classical GO were introduced, which provide a computationally inexpensive way of predicting how light scatters from particles with size much larger than the wavelength of light. Light propagation is modelled by the use of rays, which take straight-line paths undergoing reflection and refraction described by Snell's law and the Fresnel coefficients. A combination of Fraunhofer diffraction theory and Babinet's principle can be used to account for the effects of external diffraction, which is responsible for approximately one half of the scattered intensity.

In Section 4, the PBT method was described. It is the novel method presented in this work and is a physical-optics hybrid light scattering method for large, non-spherical particles,

including those with surface roughness. It is an approximate method based on the principles of GO, which leads to an accuracy that increases with the size of the particle. The particle is represented by a surface mesh, where each of the facets is grouped according to the macroscopic features of the particle. Each group forms a parent structure, and reflected and refracted beams are produced when a parent structure is illuminated by an incident wave. By use of Snell's law and the Fresnel equations of reflection and transmission, the beams can be traced in the near-field to arrive at an approximation for the electric field on the surface of the particle. A surface integral diffraction equation is used to map from the near to the far field and the scattered far field can then be used to compute scattering parameters of interest.

In Section 5, the accuracy of the PBT method was tested against the DDA method in two benchmarking studies. The PBT method was also used in a microphysics application to compute single scattering parameters for thin hexagonal ice plates.

In the first benchmark, the results of the two methods were compared for smooth and rough hexagonal columns of length 10 µm and radius 5 µm. Gaussian random roughness was used to create the surface texture, and results of various Mueller matrix elements were presented. The refractive index was varied from non-absorbing to strongly absorbing particles, and the PBT method demonstrated a significant computational efficiency, computing results in approximately 1/1000th of the time required by the DDA. For non-absorbing particles ($n = 1.31 + 0i$), both methods showed close agreement, especially in the forward regions, which (in the framework of GO) was dominated by external diffraction and transmission through pairs of parallel facets. Discrepancies can be observed in the backscattering, where the PBT method accuracy decreased, which was suspected to arise from the near-field calculation. The general agreement for weakly and strongly absorbing particles ($n = 1.31 + 0.01i$ and $n = 1.31 + 0.1i$) was good, although the PBT method overestimated the intensity in the side scattering. The asymmetry parameter, scattering and extinction efficiency errors between the methods were within 5%. The PBT method demonstrated a good overall performance, including the ability to predict 2D scattering patterns, although the accuracy in the backscattering decreased for the roughened particle investigated here.

In the second benchmark, scattering properties of hexagonal ice plates with surface roughness at a wavelength $\lambda = 0.532$ µm were investigated. The plates had an aspect ratio 10 and volume-equivalent size parameter 60. The scattering was averaged over 96 orientations so as to obtain an approximate solution to the orientation-averaged scattering. The DDA method was first used to investigate the effect of roughness on different scattering regions and integrated parameters. Secondly, it was used as a reference to measure the accuracy of the PBT computations. The surface roughness was varied with respect to both a characteristic length scale and a roughness amplitude. The DDA results showed that the scattering properties were mostly independent of the roughness length scale, and that roughness had almost no effect on the scattering when the roughness amplitude was much smaller than the wavelength. One exception to this rule was the direct backscattering, which showed a higher degree of sensitivity and decreased with the presence of surface roughness. For the particle geometries studied here, asymmetry parameters decreased by $\sim 2\%$ as the roughness amplitude increased from $\sigma = 0$ to $\sigma = \lambda$. Furthermore, it was found that the scattering from hexagonal ice plates with strong roughness amplitude ($\sigma \approx \lambda$) showed an absence of a halo peak. This suggested that the use of measuring techniques, such as that of the halo

ratio, may not necessarily be able to determine that there is an absence of ice particles with hexagonal symmetry. However, further incorporation of the halo ratio in measuring techniques could provide as a useful method of estimating surface roughness and irregularity, especially when combined with analysis of other experimental evidence such as scattering pattern symmetry and particle imaging. For the PBT method, the results showed best accuracy for roughness amplitudes in the range $\sigma \leq 2\lambda/5$ and a maximum edge length $L = 3\lambda$. In these cases, the asymmetry parameter and scattering cross sections can be computed to within 1% and 3% accuracy, respectively.

Finally, the PBT method was applied to compute the single-scattering properties of hexagonal ice plates over a wavelength range of 0.2 to 5 µm. The aspect ratio of the plates was fixed, while the diameter was varied from 55 to 95 µm in 10 µm increments. The refractive index, which varied with wavelength, was a key factor in the scattering behaviour, particularly in the transition from low to high absorption at $\lambda \approx 3$ µm. The single scattering albedo was computed, showing a strong correlation with the refractive index. When absorption is low, ω approaches 1, whereas at the peak value of absorption ($\lambda = 3.088$ µm), ω values decreased significantly to values of ≈ 0.4. The extinction efficiency was observed to follow an oscillatory pattern, with an asymptote value of 2, which is consistent with the extinction paradox. One interesting scattering feature was that $Q_{ext} \sim 1$ at $\lambda = 2.838$ µm, because the particle refractive index approaches that of the surrounding medium, reducing the scattering efficiency. The asymmetry parameter was primarily influenced by the ice plate geometry, with values consistently above 0.8. At the absorbing band $\lambda \approx 3.1$ µm, g approaches 1 due to the scattering being dominated by external diffraction and reflection.

In summary, this work details a successful endeavour to devise a physical-optics method for the computation of light scattering from large particles, with a computation speed reduced by several orders of magnitude compared to the discrete dipole approximation. The PBT method, based on a surface integral equation and a novel geometric optics ray backtracing technique, stands as a valuable tool for a wide range of applications. With further application, it has the potential to improve our understanding of light scattering from large particles, and to strengthen the relationship between theory, experiment, observational data, and prediction.

A Mueller Matrix Relations

The following section lists the relationships between elements of the Mueller matrix and elements of the amplitude scattering matrix [87]:

$$S_{11} = \frac{1}{2}\big(|S_1|^2 + |S_2|^2 + |S_3|^2 + |S_4|^2\big), \tag{A.1}$$

$$S_{12} = \frac{1}{2}\big(|S_2|^2 - |S_1|^2 + |S_4|^2 - |S_3|^2\big), \tag{A.2}$$

$$S_{13} = \mathrm{Re}\big(S_2 S_3^* + S_1 S_4^*\big), \tag{A.3}$$

$$S_{14} = \mathrm{Im}\big(S_2 S_3^* - S_1 S_4^*\big), \tag{A.4}$$

$$S_{21} = \frac{1}{2}\big(|S_2|^2 + |S_1|^2 + |S_4|^2 + |S_3|^2\big), \tag{A.5}$$

$$S_{22} = \frac{1}{2}\big(|S_2|^2 + |S_1|^2 - |S_4|^2 - |S_3|^2\big), \tag{A.6}$$

$$S_{23} = \mathrm{Re}\big(S_2 S_3^* - S_1 S_4^*\big), \tag{A.7}$$

$$S_{24} = \mathrm{Im}\big(S_2 S_3^* + S_1 S_4^*\big), \tag{A.8}$$

$$S_{31} = \mathrm{Re}\big(S_2 S_4^* + S_1 S_3^*\big), \tag{A.9}$$

$$S_{32} = \mathrm{Re}\big(S_2 S_4^* - S_1 S_3^*\big), \tag{A.10}$$

$$S_{33} = \mathrm{Re}\big(S_1 S_2^* + S_3 S_4^*\big), \tag{A.11}$$

$$S_{34} = \mathrm{Im}\big(S_2 S_1^* + S_4 S_3^*\big), \tag{A.12}$$

$$S_{41} = \mathrm{Im}\big(S_2^* S_4 + S_3^* S_1\big), \tag{A.13}$$

$$S_{42} = \mathrm{Im}\big(S_2^* S_4 - S_3^* S_1\big), \tag{A.14}$$

$$S_{43} = \mathrm{Im}\big(S_1 S_2^* - S_3 S_4^*\big), \tag{A.15}$$

$$S_{44} = \mathrm{Re}\big(S_1 S_2^* - S_3 S_4^*\big). \tag{A.16}$$

B Snell's Law Corollary

Theorem 1. *The path difference δ between the field of an sink facet and that of a source facet depends only on the z distance δ^j between the centroids of each facet.*

Proof. The geometry of the problem is comprised of 2 facets of the particle surface mesh. The first facet is assumed to have been illuminated by an external plane wave, and has led to a refracted wave inside the particle. A ray has been backtraced from the second facet and has intersected within the bounded surface of the first facet. This means that the second facet will be illuminated by the first facet and therefore the beam is to be propagated in the $-\hat{\mathbf{z}}$ direction along the path of the backtraced ray. Assuming knowledge of the amplitude matrix at the centroid of the source facet $\mathbf{S_k}$, the goal is to find the amplitude matrix at the centroid of the sink facet $\mathbf{S_j}$. The geometry of the problem is shown in Figure B.1 (which is a copy of Figure 3.4). Initially, there are two incident rays of interest. The first ray intersects

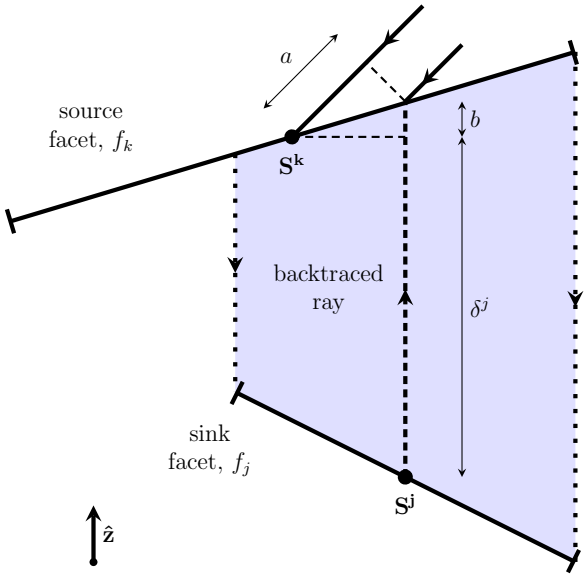

Figure B.1: Beam propagation from a source facet f^k to a sink facet f^j. Facet centroids are represented by black dots. A ray is backtraced from the centroid of f^j and is found to intersect within the bounded cross section of f^k. Edges of the beam are represented by dotted lines. It can be shown that $n_1 a = n_2 b$, and therefore δ^j describes the path length between the centroid of f^k and f^j. The corresponding phase difference relates $\mathbf{S^k}$ to $\mathbf{S^j}$.

with the centroid of the sink facet. The second ray has an intersection with f_k that coincides with that of the backtraced ray from f_j. If the transmitted field is also a plane wave, then the path difference δ between $\mathbf{S_k}$ and $\mathbf{S_j}$ is given by

$$\delta = -a + n(b + \delta^j), \tag{B.1}$$

where n is refractive index. Using the geometry of the problem gives that

$$\frac{a}{\sin\theta_i} = \frac{b}{\sin\theta_t}, \tag{B.2}$$

where θ_i and θ_t are the angles of incidence and transmission, respectively. Applying Snell's law, $\sin\theta_i = n\sin\theta_t$, gives $a = nb$. Substituting this into Eq. B.1 gives that $\delta = \delta^j$, which completes the proof. A similar theorem can be derived for the case of internal reflection, which allows this method to also be used for internal beam reflections. □

C PBT Command Line Arguments

The PBT code reads input parameters from the command line. Each input parameter is defined by a keyphrase, with arguments following a space delimiter. The ordering of most arguments in the command line is not important and the PBT will search through lines from left to right in an attempt to find each argument. A summary of command line arguments is given below:

- `-lambda <value>` - Defines the wavelength of incident light. If omitted, the default value is `0.532`.
- `-rbi <value>` - Defines the real component of the particle refractive index. If omitted, the default value is `1.31`.
- `-ibi <value>` - Defines the imaginary component of the particle refractive index. If omitted, the default value is `0`.
- `-cmethod <string>` - Defines the method of particle input. If omitted, the PBT will use the `cc_hex` method to make a hexagonal prism with radius 5 and prism length 10. Current supported methods are:
  - `read` - Attempts to read the particle from the current directory. If `read` is specified, the following arguments may also be specified:
    - `-cft <string>` - Defines the particle input filetype. The supported particle file input types are:
      - `obj` - Wavefront style geometry file
      - `mrt` - Macke ray-tracing type

      If `-cfn` is omitted, the PBT will attempt to guess the particle filetype based on the file extension. Macke ray-tracing style is assumed for file extensions `.cry` and `.crystal`, and wavefront style is assumed for file extension `.obj`.
    - `-cfn <string>` - Defines the particle filename. To ensure that the particle file is sufficiently discretised (ie. at least 4 elements per wavelength), see information on the `-tri` flag for triangulation. If the mesh consists only of triangles, the PBT will assume it is sufficiently discretised and automatic triangulation will be disabled. If the mesh contains a facet with more than 3 vertices, the PBT will enable triangulation by default because the code does not currently directly support this.
    - `-afn <string>` - Defines the apertures filename. The apertures file contains a single column defining which aperture each face belongs to. The number of lines in the apertures file must match the total number of faces in the particle file.
  - `cc_hex` - Attempts to make a Gaussian rough hexagonal column/plate. Uses method developed by C. Collier [74], based on Muinonen & Saarinen 2000 [128]. If this flag is used, several other flags may also be specified:

    * `-cc_hex_l <value>` - L from Muinonen & Saarinen 2000. Should be large compared to the correlation length (see below). If omitted, the default value is `20`.
    * `-cc_hex_hr` - Hexagonal edge length. If omitted, the default value is `5`.
    * `-cc_hex_nfhr` - Number of subdivisions along each hexagonal edge. If omitted, the default value is `6`.
    * `-cc_hex_pfl` - Prism edge length. If omitted, the default value is `10`.
    * `-cc_hex_nfpl` - Number of subdivisions along each prism edge. If omitted, the default value is `12`.
    * `-cc_hex_pher` - Number of rotations to perform at prism facet-basal facet edges (10% of no. of subfacets along prism edge). If omitted, the default value is `1`.
    * `-cc_hex_pper` - Number of rotations to perform at prism facet-prism facet edges (10% of subfacets along hexagon edge). If omitted, the default value is `1`.
    * `-cc_hex_nscales` - Number of roughness scales. If omitted, the default value is `1`.
    * `-cc_hex_cls` - Correlation lengths for each roughness scale, separated by spaces. If omitted, the default value is `1`.
    * `-cc_hex_sds` - Standard deviations for each roughness scale, separated by spaces. If omitted, the default value is `0`.
- `-rec <value>` - Defines the total number of beam recursions per orientation. If omitted, the default value is `8`.
- `-refl <value>` - Defines the max number of beam total internal reflection events per orientation. If omitted, the default value is `10`.
- `-rot <args>` - Defines the orientation of the particle. It is optional. If omitted, the PBT will not rotate the input particle. The `<args>` parameter is used to define the method of rotation, or to define random orientation. Current supported methods are:
    * `euler <alpha> <beta> <gamma>` - Choose to rotate the particle according to the 3 Euler angles, given in degrees. There are several ways to rotate via Euler angles; the PBT follows the method of Mishchenko.
        · Example: `-rot euler 11 25 32`
    * `off 30 0,10,20,30` - Choose to rotate the particle according to the "off" convention. Only 4 different values are currently supported for this method. Input particle should be oriented lengthways, with prism axis lying in the xy plane.
        · Example: `-rot off 30 20`
    * `none` - Choose to not rotate the particle.
        · Example: `rot none`

    * `multi <value>` - Choose to randomly orient the particle. `<value>` defines the number of orientations. For reproducibility, the random_seed subroutine can be used to set the random seed to a specified value, which will cause the random orientations to be reproducible. Since the Euler α angle has no effect on the 1-d scattering, it is set to 0 for orientation averaging.
        · Example: `-rot multi 1000`

- `-mt <value>` - Defines whether the code should attempt to use multithreading, where appropriate. The value may be `0` for no multithreading, or `1` for multithreading. If omitted, multithreading is enabled by default. If enabled, the user should ensure that the relevant `omp` environment variables are set up for their system, e.g., `OMP_STACKSIZE`, `OMP_NUM_THREADS`, etc. If the code throws a segmentation fault at the diffraction subroutine, the user will likely need to increase the `OMP_STACKSIZE`.
- `-jobname <string>` - Specifies the name of the directory within which the output files should be placed. It is optional. If omitted, `"my_job#"` is used, where # is an integer. If the directory already exists, an integer is appended to the directory name so that no files are overwritten.
- `-theta values` - Specifies the polar angles at which the far-field should be evaluated. See below for example usage:
    * `-theta 0 1 180` - Evaluate the far-field from 0 in 1 degree steps to 180. If omitted, this is the default behaviour.
    * `-theta 6 0.1 25 150 175 0.25 180` - Evaluate the far-field from 6 in 0.1 degree steps to 25, then step to 175, then in 0.25 degree steps to 180.
- `-phi values` - Specifies the azimuthal angles at which the far-field should be evaluated. See below for example usage:
    * `-phi 0 1 360` - Evaluate the far-field from 0 in 1 degree steps to 360. If omitted, this is the default behaviour.
- `-no2d` - Suppresses the output of the 2D Mueller matrix, which can be a large file if many far-field evaluation angles are specified.
- `-tri` - Enables automatic Delaunay triangulation. Note that use of this flag requires compiling the triangle code in `./src/tri/`.
- `-tri_edge <value>` - Sets the maximum edge length for triangulation. If omitted, the default value is `1`.
- `-tri_rough <value>` - Sets the standard deviation for roughness derived from the triangulation. If omitted, the default value is `0`.
- `-tri_div <value>` - Sets the minimum divides per average parent length dimension from the triangulation. If omitted, the default value is `1`.
- `-time_limit <value>` - Sets a time limit (in hours). The PBT will save at an intermediate point if this time is surpassed. Use `-resume <value>` to resume the job (see below).

- `-resume <value>` - Resumes a previous job that was saved at an intermediate point. `value` must be the number of the cache ID. This option overrides most input parameters with those read from the cached job.
- `-scaling` - Forces the diffracted energy in the far-field to be conserved with respect to the near-field energy.
- `-timing` - Enables more detailed output of the timing of different parts of the code.
- `-debug <value>` - Controls the level of debugging output:
  - `0` - Minimal output
  - `1` - Some output (default)
  - `2` - Large output
  - `3` - Extreme output
- `-export_beam <args>` - Exports information about the beams to a file
  - `num <value> [<value>]` - Exports by beam number. If 1 value is given, the beam tree is exported from the first beam index to the index specified by the value. If 2 values are given, the beam tree is exported from the beam index specified by the first value to the beam index specified by the second value.
  - `rec <value> [<value>]` - Exports by recursion number. If 1 value is given, the beam tree is exported from the first recursion to the recursion specified by the value. If 2 values are given, the beam tree is exported from the recursion specified by the first value to the recursion specified by the second value.
- `-fast_diff` - Enables an approximate but faster diffraction method. According to Jackson, Classical Electrodynamics Sec 10.5 [29], most of the diffracted energy is confined within the angle λ/d, where d is a linear dimension of the aperture. If this flag is enabled, any far-field bins outside an angle of $8\lambda/d$ are excluded from the diffraction calculation, for a given outgoing beam. This flag also restricts the external diffraction to the forward scattering.
- `intellirot` - Sets the Euler angles for orientation averaging to be uniformly distributed, instead of randomly distributed.
- `beta_min <value>` - Sets the minimum beta angle for orientation averaging, which can be used to take advantage of particle symmetry. Must be in the range `0` to `180`.
- `beta_max <value>` - Sets the maximum beta angle for orientation averaging, which can be used to take advantage of particle symmetry. Must be in the range `0` to `180`.
- `gamma_min <value>` - Sets the minimum gamma angle for orientation averaging, which can be used to take advantage of particle symmetry. Must be in the range `0` to `360`.
- `gamma_max <value>` - Sets the maximum gamma angle for orientation averaging, which can be used to take advantage of particle symmetry. Must be in the range `0` to `360`.

– `-output_eulers` - Outputs the Euler angles used for orientation averaging to a file.

– `-speed` - Prioritises speed over memory use. This flag is enabled by default.

– `-memory` - Prioritises memory use over speed.

Bibliography

[1] Márquez-Islas R. et al. Visual Assessment of Blood Plasma versus Optical Transmittance and Refractive Index Measurements for Quantifying Lipemia. Diagnostics Feb. 2022;12. https://doi.org/10.3390/diagnostics12020510.

[2] Gienger J. et al. Assessment of deformation of human red blood cells in flow cytometry: measurement and simulation of bimodal forward scatter distributions. Biomedical Optics Express Sept. 2019;10:4531. https://doi.org/10.1364/boe.10.004531.

[3] Masilamani V. et al. Smoking induced hemolysis: spectral and microscopic investigations. Scientific Reports 2016;6:21095. https://doi.org/10.1038/srep21095.

[4] McKinnon K. M. Flow cytometry: an overview. Current protocols in immunology 2018;120:5–1. https://doi.org/10.1002/cpim.40.

[5] Barone T. et al. Calibration of the cloud and aerosol spectrometer for coal dust composition and morphology. Advanced Powder Technology 2019;30:1805–1814. https://doi.org/10.1016/j.apt.2019.05.023.

[6] Stopford C. et al. Real-time detection of airborne asbestos by light scattering from magnetically re-aligned fibers. Opt. Express 2013;21:11356–11367. https://doi.org/10.1364/OE.21.011356.

[7] Ruiter S. et al. Exposure Monitoring Strategies for Applying Low-Cost PM Sensors to Assess Flour Dust in Industrial Bakeries. Annals of Work Exposures and Health Jan. 2023;67:379–391. https://doi.org/10.1093/annweh/wxac088.

[8] Liati A. et al. Investigation of diesel ash particulate matter: A scanning electron microscope and transmission electron microscope study. Atmospheric Environment 2012;49:391–402. https://doi.org/10.1016/j.atmosenv.2011.10.035.

[9] Polle J., Tran D., and Ben-Amotz A. History, distribution, and habitats of algae of the genus *Dunaliella* Teodoresco (Chlorophyceae). *The Alga Dunaliella*. CRC Press; New York, NY, USA: 2009, 1–14. https://doi.org/10.1201/9780429061639-1.

[10] McLeod G. C. The Effect of Circularly Polarized Light on the Photosynthesis and Chlorophyll a Synthesis of Certain Marine Algae. Limnology and Oceanography 1957; 2:360–362. https://doi.org/10.1002/lno.1957.2.4.0360.

[11] Powers J. G. et al. The weather research and forecasting model: Overview, system efforts, and future directions. Bulletin of the American Meteorological Society Aug. 2017;98:1717–1737. https://doi.org/10.1175/BAMS-D-15-00308.1.

[12] Baran A. J. A review of the light scattering properties of cirrus. Journal of Quantitative Spectroscopy and Radiative Transfer. XI Conference on Electromagnetic and Light Scattering by Non-Spherical Particles: 2008 2009;110:1239–1260. https://doi.org/10.1016/j.jqsrt.2009.02.026.

[13] Heymsfield A. J. et al. Cirrus Clouds. Meteorological Monographs 2017;58:2.1–2.26. https://doi.org/10.1175/AMSMONOGRAPHS-D-16-0010.1.

[14] Mishchenko M. I., Hovenier J. W., and Travis L. D. Light Scattering by Nonspherical Particles. Academic Press; San Diego, CA, USA: 1999.

[15] Hahn C. J. and Warren S. G. A Gridded Climatology of Clouds over Land (1971-96) and Ocean (1954-97) from Surface Observations Worldwide. Data set. Dec. 2007. https://doi.org/10.3334/cdiac/cli.ndp026e.

[16] Kaye P. H. et al. Classifying atmospheric ice crystals by spatial light scattering. Opt. Lett. 2008;33:1545–1547. https://doi.org/10.1364/OL.33.001545.

[17] Giri R. et al. Generation of aerosol-particle light-scattering patterns from digital holograms. Optics Letters Feb. 2019;44:819. https://doi.org/10.1364/ol.44.000819.

[18] Winker D. M., Hunt W. H., and McGill M. J. Initial performance assessment of CALIOP. Geophysical Research Letters 2007;34. https://doi.org/10.1029/2007GL030135.

[19] Mitchell C. J., Porco C. C., and Weiss J. W. Tracking the Geysers of Enceladus into Saturn's E Ring. The Astronomical Journal 2015;149:156. https://doi.org/10.1088/0004-6256/149/5/156.

[20] Martin W. et al. Hydrothermal vents and the origin of life. Nature Reviews Microbiology 2008;6:805–814. https://doi.org/10.1038/nrmicro1991.

[21] Morello C. and Berg M. J. A light scattering analysis of the cryovolcano plumes on enceladus. Journal of Quantitative Spectroscopy and Radiative Transfer 2024; 322:109018. https://doi.org/10.1016/j.jqsrt.2024.109018.

[22] Hecht E. Optics, 5th Ed. Pearson Education; Essex, UK: 1987.

[23] Kravtsov Y. and Orlov Y. Geometrical Optics of Inhomogeneous Media. Springer Series on Wave Phenomena. Springer Berlin; Heidelberg, DE: 2011. ISBN: 9783642840333.

[24] Baum B. A. et al. Bulk Scattering Properties for the Remote Sensing of Ice Clouds. Part III: High-Resolution Spectral Models from 100 to 3250 cm-1. Journal of Applied Meteorology and Climatology 2007;46:423–434. https://doi.org/10.1175/JAM2473.1.

[25] Heymsfield A. J. and Miloshevich L. M. Parameterizations for the Cross-Sectional Area and Extinction of Cirrus and Stratiform Ice Cloud Particles. Journal of the Atmospheric Sciences 2003;60:936–956. https://doi.org/"10.1175/1520-0469(2003)060<0936:PFTCSA>2.0.CO;2".

[26] Magee N. et al. Captured cirrus ice particles in high definition. Atmospheric Chemistry and Physics 2021;21:7171–7185. https://doi.org/10.5194/acp-21-7171-2021.

[27] Wadell H. Volume, Shape, and Roundness of Rock Particles. The Journal of Geology 1932;40:443–451. https://doi.org/10.1086/623964.

[28] Bohren C. F. and Huffman D. R. Absorption and Scattering of Light by Small Particles. John Wiley & Sons; Hoboken, NJ, USA: 1983.

[29] Jackson J. D. Classical Electrodynamics. John Wiley & Sons; New York, NY, USA: 1998.

[30] Wendling P., Wendling R., and Weickmann H. K. Scattering of solar radiation by hexagonal ice crystals. Appl. Opt. 1979;18:2663–2671. https://doi.org/10.1364/AO.18.002663.

[31] Cai Q. and Liou K.-N. Polarized light scattering by hexagonal ice crystals: theory. Appl. Opt. 1982;21:3569–3580. https://doi.org/10.1364/AO.21.003569.

[32] Muinonen K. Scattering of light by crystals: a modified Kirchhoff approximation. Appl. Opt. 1989;28:3044–3050. https://doi.org/10.1364/AO.28.003044.

[33] Takano Y. and Liou K.-N. Solar Radiative Transfer in Cirrus Clouds. Part I: Single-Scattering and Optical Properties of Hexagonal Ice Crystals. Journal of Atmospheric Sciences 1989;46:3–19. https://doi.org/"10.1175/1520-0469(1989)046<0003:SRTICC>2.0.CO;2".

[34] Macke A. Scattering of light by polyhedral ice crystals. Appl. Opt. 1993;32:2780–2788. https://doi.org/10.1364/AO.32.002780.

[35] Macke A., Mueller J., and Raschke E. Single Scattering Properties of Atmospheric Ice Crystals. Journal of Atmospheric Sciences 1996;53:2813–2825. https://doi.org/10.1175/1520-0469(1996)053<2813:SSPOAI>2.0.CO;2.

[36] Borovoi A. G. Light scattering by large particles: physical optics and the shadow-forming field. *Light Scattering Reviews 8: Radiative transfer and light scattering*. Ed. by A. A. Kokhanovsky. Springer Berlin Heidelberg; Berlin, Heidelberg: 2013, 115–138. ISBN: 978-3-642-32106-1. https://doi.org/10.1007/978-3-642-32106-1_3.

[37] Yang P. and Liou K. N. Light scattering by hexagonal ice crystals: solutions by a ray-by-ray integration algorithm. J. Opt. Soc. Am. A 1997;14:2278–2289. https://doi.org/10.1364/JOSAA.14.002278.

[38] Hesse E. and Ulanowski Z. Scattering from long prisms computed using ray tracing combined with diffraction on facets. Journal of Quantitative Spectroscopy and Radiative Transfer. Electromagnetic and Light Scattering by Non-Spherical Particles 2003; 79-80:721–732. https://doi.org/10.1016/S0022-4073(02)00317-5.

[39] Borovoi A. G. and Grishin I. A. Scattering matrices for large ice crystal particles. J. Opt. Soc. Am. A 2003;20:2071–2080. https://doi.org/10.1364/JOSAA.20.002071.

[40] Bi L. et al. Scattering and absorption of light by ice particles: Solution by a new physical-geometric optics hybrid method. Journal of Quantitative Spectroscopy and Radiative Transfer 2011;112:1492–1508. https://doi.org/10.1016/j.jqsrt.2011.02.015.

[41] Konoshonkin A. V., Kustova N. V., and Borovoi A. G. Beam-splitting code for light scattering by ice crystal particles within geometric-optics approximation. Journal of Quantitative Spectroscopy and Radiative Transfer 2015;164:175–183. https://doi.org/10.1016/j.jqsrt.2015.06.008.

[42] Liu C., Panetta R. L., and Yang P. The effective equivalence of geometric irregularity and surface roughness in determining particle single-scattering properties. Opt. Express 2014;22:23620–23627. https://doi.org/10.1364/OE.22.023620.

[43] Yang P. et al. Spectrally Consistent Scattering, Absorption, and Polarization Properties of Atmospheric Ice Crystals at Wavelengths from 0.2 to 100 µm. Journal of the Atmospheric Sciences 2013;70:330–347. https://doi.org/10.1175/JAS-D-12-039.1.

[44] Saito M. and Yang P. Oriented Ice Crystals: A Single-Scattering Property Database for Applications to Lidar and Optical Phenomenon Simulations. Journal of the Atmospheric Sciences 2019;76:2635–2652. https://doi.org/10.1175/JAS-D-19-0031.1.

[45] Saito M. et al. A Comprehensive Database of the Optical Properties of Irregular Aerosol Particles for Radiative Transfer Simulations. Journal of the Atmospheric Sciences 2021;78:2089–2111. https://doi.org/10.1175/JAS-D-20-0338.1.

[46] Timofeev D. N. et al. Light Backscattering Properties of Distorted Hexagonal Atmospheric Ice Particles within the Physical Optics Approximation. Atmospheric and Oceanic Optics 2022;35:158–163. https://doi.org/10.1134/S1024856022020130.

[47] Hesse E. et al. Discussion of a physical optics method and its application to absorbing smooth and slightly rough hexagonal prisms. Journal of Quantitative Spectroscopy and Radiative Transfer 2018;218:54–67. https://doi.org/10.1016/j.jqsrt.2018.06.019.

[48] Mie G. Beiträge zur Optik trüber Medien, speziell kolloidaler Metallösungen. Annalen der Physik 1908;330:377–445. https://doi.org/10.1002/andp.19083300302.

[49] Mishchenko M. I. et al. Sensitivity of cirrus cloud albedo, bidirectional reflectance and optical thickness retrieval accuracy to ice particle shape. Journal of Geophysical Research: Atmospheres 1996;101:16973–16985. https://doi.org/10.1029/96JD01155.

[50] Yang P. et al. Sensitivity of cirrus bidirectional reflectance to vertical inhomogeneity of ice crystal habits and size distributions for two Moderate-Resolution Imaging Spectroradiometer (MODIS) bands. Journal of Geophysical Research: Atmospheres 2001;106:17267–17291. https://doi.org/10.1029/2000JD900618.

[51] Yang P. et al. Single-scattering properties of droxtals. Journal of Quantitative Spectroscopy and Radiative Transfer. Electromagnetic and Light Scattering by Non-Spherical Particles 2003;79-80:1159–1169. https://doi.org/10.1016/S0022-4073(02)00347-3.

[52] Korolev A. and Isaac G. Roundness and Aspect Ratio of Particles in Ice Clouds. Journal of the Atmospheric Sciences 2003;60:1795–1808. https://doi.org/10.1175/1520-0469(2003)060<1795:RAAROP>2.0.CO;2.

[53] Waterman P. C. Matrix formulation of electromagnetic scattering. 1965. URL: https://api.semanticscholar.org/CorpusID:110182598.

[54] Mishchenko M. I., Travis L. D., and Mackowski D. W. T-matrix computations of light scattering by nonspherical particles: A review. Journal of Quantitative Spectroscopy and Radiative Transfer. Light Scattering by Non-Spherical Particles 1996;55:535–575. https://doi.org/10.1016/0022-4073(96)00002-7.

[55] Doicu A., Eremin Y., and Wriedt T. Acoustic and Electromagnetic Scattering Analysis Using Discrete Sources. Academic Press; London, UK: Jan. 2000.

[56] Yee K. Numerical solution of initial boundary value problems involving maxwell's equations in isotropic media. IEEE Transactions on Antennas and Propagation 1966; 14:302–307. https://doi.org/10.1109/TAP.1966.1138693.

[57] Yang P. and Liou K. N. Finite-difference time domain method for light scattering by small ice crystals in three-dimensional space. J. Opt. Soc. Am. A Oct. 1996;13:2072–2085. https://doi.org/10.1364/JOSAA.13.002072.

[58] Sun W., Fu Q., and Chen Z. Finite-difference time-domain solution of light scattering by dielectric particles with a perfectly matched layer absorbing boundary condition. Appl. Opt. 1999;38:3141–3151. https://doi.org/10.1364/AO.38.003141.

[59] Purcell E. M. and Pennypacker C. R. Scattering and adsorption of light by nonspherical dielectric grains. Astrophys J 1973;186:705–714. https://doi.org/10.1086/152538.

[60] Draine B. T. The discrete-dipole approximation and its applications to interstellar graphite grains. Astrophys J 1988;333:848–872. https://doi.org/10.1086/166795.

[61] Goedecke G. H. and O'Brien S. G. Scattering by irregular inhomogeneous particles via the digitized Green's function algorithm. Appl. Opt. 1988;27:2431–2438. https://doi.org/10.1364/AO.27.002431.

[62] Yurkin M. A. and Hoekstra A. G. The discrete-dipole-approximation code ADDA: Capabilities and known limitations. Journal of Quantitative Spectroscopy and Radiative Transfer. Polarimetric Detection, Characterization, and Remote Sensing 2011; 112:2234–2247. https://doi.org/10.1016/j.jqsrt.2011.01.031.

[63] Peltoniemi J. I. et al. Scattering of light by stochastically rough particles. Appl. Opt. 1989;28:4088–4095. https://doi.org/10.1364/AO.28.004088.

[64] Pfisterer R. N. Approximated scatter models for stray light analysis. Optics & Photonics News 2011;22:16–17.

[65] Yang P. and Liou K.-N. Single-scattering properties of complex ice crystals in terrestrial atmosphere. Contributions to atmospheric physics. https://api.semanticscholar.org/CorpusID:127657992 1998;71:223–248.

[66] Letu H. et al. Investigation of ice particle habits to be used for ice cloud remote sensing for the GCOM-C satellite mission. Atmospheric Chemistry and Physics 2016; 16:12287–12303. https://doi.org/10.5194/acp-16-12287-2016.

[67] Nousiainen T. and McFarquhar G. M. Light Scattering by Quasi-Spherical Ice Crystals. Journal of the Atmospheric Sciences 2004;61:2229–2248. https://doi.org/10.1175/1520-0469(2004)061<2229:LSBQIC>2.0.CO;2.

[68] Nousiainen T. and Muinonen K. Surface-roughness effects on single-scattering properties of wavelength-scale particles. Journal of Quantitative Spectroscopy and Radiative Transfer. IX Conference on Electromagnetic and Light Scattering by Non-Spherical Particles 2007;106:389–397. https://doi.org/https://doi.org/10.1016/j.jqsrt.2007.01.024.

[69] Um J. and McFarquhar G. M. Dependence of the single-scattering properties of small ice crystals on idealized shape models. Atmospheric Chemistry and Physics 2011; 11:3159–3171. https://doi.org/10.5194/acp-11-3159-2011.

[70] McFarquhar G. M. et al. A New Parameterization of Single Scattering Solar Radiative Properties for Tropical Anvils Using Observed Ice Crystal Size and Shape Distributions. Journal of the Atmospheric Sciences 2002;59:2458–2478. https://doi.org/10.1175/1520-0469(2002)059<2458:ANPOSS>2.0.CO;2.

[71] Mishchenko M. I. Calculation of the amplitude matrix for a nonspherical particle in a fixed orientation. Appl. Opt. 2000;39:1026–1031. https://doi.org/10.1364/AO.39.001026.

[72] Muinonen K. Light Scattering by Gaussian Random Particles. Earth Moon and Planets 1996;72:339–342. https://doi.org/10.1007/BF00117539.

[73] Muinonen K. et al. Light scattering by Gaussian particles with internal inclusions and roughened surfaces using ray optics. Journal of Quantitative Spectroscopy and Radiative Transfer. XI Conference on Electromagnetic and Light Scattering by Non-Spherical Particles: 2008 2009;110:1628–1639. https://doi.org/10.1016/j.jqsrt.2009.03.012.

[74] Collier C. et al. Effects of surface roughness with two scales on light scattering by hexagonal ice crystals large compared to the wavelength: DDA results. Journal of Quantitative Spectroscopy and Radiative Transfer 2016;182:225–239. https://doi.org/10.1016/j.jqsrt.2016.06.007.

[75] Riskilä E., Lindqvist H., and Muinonen K. Light scattering by fractal roughness elements on ice crystal surfaces. Journal of Quantitative Spectroscopy and Radiative Transfer 2021;267:107561. https://doi.org/10.1016/j.jqsrt.2021.107561.

[76] Waterman P. C. Matrix formulation of electromagnetic scattering. Proceedings of the IEEE. 1965;53:805–812.

[77] Liu Q. H. The PSTD algorithm: A time-domain method requiring only two cells per wavelength. Microwave and Optical Technology Letters 1997;15:158–165. https://doi.org/10.1002/(SICI)1098-2760(19970620)15:3<158::AID-MOP11>3.0.CO;2-3.

[78] Grynko Y., Shkuratov Y., and Förstner J. Light scattering by irregular particles much larger than the wavelength with wavelength-scale surface roughness. Opt. Lett. 2016; 41:3491–3494. https://doi.org/10.1364/OL.41.003491.

[79] Neshyba S. P. et al. Roughness metrics of prismatic facets of ice. Journal of Geophysical Research: Atmospheres 2013;118:3309–3318. https://doi.org/10.1002/jgrd.50357.

[80] Heymsfield A. Cirrus Uncinus Generating Cells and the Evolution of Cirriform Clouds. Part I: Aircraft Observations of the Growth of the Ice Phase. Journal of Atmospheric Sciences 1975;32:799–808. https://doi.org/10.1175/1520-0469(1975)032<0799:CUGCAT>2.0.CO;2.

[81] Kobayashi T. and Ohtake T. Hexagonal Twin Prisms of Ice. Journal of Atmospheric Sciences 1974;31:1377–1383. https://doi.org/10.1175/1520-0469(1974)031<1377:HTPOI>2.0.CO;2.

[82] Haralick R. M., Shanmugam K., and Dinstein I. Textural Features for Image Classification. IEEE Transactions on Systems, Man, and Cybernetics 1973;SMC-3:610–621. https://doi.org/10.1109/TSMC.1973.4309314.

[83] Lu R.-S. et al. Grinding surface roughness measurement based on the co-occurrence matrix of speckle pattern texture. Appl. Opt. 2006;45:8839–8847. https://doi.org/10.1364/AO.45.008839.

[84] Ulanowski Z. et al. Retrieving the size of particles with rough surfaces from 2D scattering patterns. Atti della Accademia Peloritana dei Pericolanti - Classe di Scienze Fisiche, Matematiche e Naturali 2011;89. https://doi.org/10.1478/C1V89S1P087.

[85] Ulanowski Z. et al. Incidence of rough and irregular atmospheric ice particles from Small Ice Detector 3 measurements. Atmospheric Chemistry and Physics 2014;14:1649–1662. https://doi.org/10.5194/acp-14-1649-2014.

[86] Born M. and Wolf E. Principles of Optics. Pergamon Press; Oxford, UK: 1999.

[87] Hovenier J. W., Mee C., and Domke H. Transfer of Polarised Light in Planetary Atmospheres. Springer Dordrecht; Dordrecht, NL: 2004.

[88] Bass M. Handbook of Optics. Vol 1: Geometrical and Physical Optics, Polarized Light, Components and Instruments. McGraw Hill Education; New York, NY, USA: 2009.

[89] Baran A. J. From the single-scattering properties of ice crystals to climate prediction: A way forward. Atmospheric Research 2012;112:45–69. https://doi.org/10.1016/j.atmosres.2012.04.010.

[90] Moosmüller H. et al. Black metal nanoparticles from abrasion processes in everyday life: Bicycle drivetrains and rock-climbing ropes. Optics Communications 2021;479:126413. https://doi.org/10.1016/j.optcom.2020.126413.

[91] Hulst H. C. van de. Light Scattering by Small Particles. Dover Publications; New York, NY, USA: 1981.

[92] Watson P. A. Rainfall crosspolarisation at microwave frequencies. Proc. Inst. Electr. Eng. 1973;120:413–418. https://doi.org/10.1049/piee.1973.0090.

[93] Morrison J. A. and Chu T. S. Perturbation calculations of rain-induced differential attenuation and differential phase shift at microwave frequencies. The Bell System Technical Journal 1973;52:1907–1913. https://doi.org/10.1002/j.1538-7305.1973.tb02715.x.

[94] Morrison J. A. Scattering of a plane electromagnetic wave by axisymmetric raindrops. Bell Syst. Tech. J. 1974;53:955–1019. https://doi.org/10.1002/j.1538-7305.1974.tb02779.x.

[95] Yurkin M. A. Chapter 9 - Discrete dipole approximation. *Light, Plasmonics and Particles*. Ed. by M. P. Mengüç and M. Francoeur. Nanophotonics. Elsevier; 2023, 167–198. ISBN: 978-0-323-99901-4. https://doi.org/10.1016/B978-0-323-99901-4.00020-2.

[96] Schmidt K., Yurkin M. A., and Kahnert M. A case study on the reciprocity in light scattering computations. Opt. Express 2012;20:23253–23274. https://doi.org/10.1364/OE.20.023253.

[97] Cunha R. da and Hopkins T. The parallel iterative methods package for systems of linear equations, user's guide. 2003. URL: https://kar.kent.ac.uk/21398/1/PIM2Hopkins.pdf.

[98] Papadopoulos A. Roshdi Rashed, Historian of Greek and Arabic mathematics. working paper or preprint. 2017. URL: https://hal.science/hal-01653436.

[99] Hormann K. and Agathos A. The point in polygon problem for arbitrary polygons. Computational Geometry 2001;20:131–144. https://doi.org/10.1016/S0925-7721(01)00012-8.

[100] Chang P. C., Walker J., and Hopcraft K. Ray tracing in absorbing media. Journal of Quantitative Spectroscopy and Radiative Transfer 2005;96:327–341. https://doi.org/10.1016/j.jqsrt.2005.01.001.

[101] Yang P. and Liou K. N. Geometric-optics–integral-equation method for light scattering by nonspherical ice crystals. Appl. Opt. Nov. 1996;35:6568–6584. https://doi.org/10.1364/AO.35.006568.

[102] Ballington H. Parent Beam Tracer Code. https://github.com/hballington12/pbt. 2024.

[103] Karczewski B. and Wolf E. Comparison of Three Theories of Electromagnetic Diffraction at an Aperture.* Part I: Coherence Matrices. J. Opt. Soc. Am. Sept. 1966; 56:1207–1214. https://doi.org/10.1364/JOSA.56.001207.

[104] Yurkin M. and Hoekstra A. The discrete dipole approximation: An overview and recent developments. Journal of Quantitative Spectroscopy and Radiative Transfer. IX Conference on Electromagnetic and Light Scattering by Non-Spherical Particles 2007;106:558–589. https://doi.org/10.1016/j.jqsrt.2007.01.034.

[105] Taylor L. A Beam Tracing Model for Electromagnetic Scattering by Atmospheric Ice Crystals. PhD thesis. University of Hertfordshire, UK, 2016. URL: https://uhra.herts.ac.uk/handle/2299/17645.

[106] Borovoi A., Konoshonkin A., and Kustova N. The physical-optics approximation and its application to light backscattering by hexagonal ice crystals. Journal of Quantitative Spectroscopy and Radiative Transfer. Electromagnetic and Light Scattering by Nonspherical Particles XIV 2014;146:181–189. https://doi.org/10.1016/j.jqsrt.2014.04.030.

[107] Sheffer A. Model simplification for meshing using face clustering. Computer-Aided Design 2001;33:925–934. https://doi.org/10.1016/S0010-4485(00)00116-0.

[108] Sommerfeld A. Partial Differential Equations in Physics. Academic Press; New York, NY, USA: 1949.

[109] Hesse E. et al. Modelling diffraction by facetted particles. Journal of Quantitative Spectroscopy and Radiative Transfer 2012;113:342–347. https://doi.org/10.1016/j.jqsrt.2011.11.017.

[110] OpenMP Architecture Review Board. OpenMP Application Program Interface Version 4.5. Nov. 2015. URL: https://www.openmp.org/wp-content/uploads/openmp-4.5.pdf.

[111] Gabriel E. et al. Open MPI: Goals, Concept, and Design of a Next Generation MPI Implementation. *Recent Advances in Parallel Virtual Machine and Message Passing Interface*. Ed. by D. Kranzlmüller, P. Kacsuk, and J. Dongarra. Springer Berlin Heidelberg; Berlin, Heidelberg: 2004, 97–104. ISBN: 978-3-540-30218-6. https://doi.org/10.1007/978-3-540-30218-6_19.

[112] Hennion P. E. Algorithm 77: Interpolation, differentiation, and integration. Commun. ACM 1962;5:96. https://doi.org/10.1145/366792.366811.

[113] Penttilä A. Fortran 95 implementation of meshconvert computer code. 2023. URL: https://wiki.helsinki.fi/xwiki/bin/view/PSR/Planetary%20System%20Research%20group/People/Antti%20Penttil%C3%A4/Collection%20of%20codes/.

[114] Shewchuk J. R. Triangle: Engineering a 2D quality mesh generator and Delaunay triangulator. *Applied Computational Geometry Towards Geometric Engineering*. Ed. by M. C. Lin and D. Manocha. Springer Berlin Heidelberg; Berlin, Heidelberg: 1996, 203–222. ISBN: 978-3-540-70680-9.

[115] Yurkin M., Maltsev V., and Hoekstra A. The discrete dipole approximation for simulation of light scattering by particles much larger than the wavelength. Journal of Quantitative Spectroscopy and Radiative Transfer. IX Conference on Electromagnetic and Light Scattering by Non-Spherical Particles 2007;106:546–557. https://doi.org/10.1016/j.jqsrt.2007.01.033.

[116] Penttilä A. et al. Comparison between discrete dipole implementations and exact techniques. Journal of Quantitative Spectroscopy and Radiative Transfer. IX Conference on Electromagnetic and Light Scattering by Non-Spherical Particles 2007; 106:417–436. https://doi.org/10.1016/j.jqsrt.2007.01.026.

[117] Muinonen K. Light Scattering by Gaussian Random Particles 1996:339–342. https://doi.org/10.1007/978-94-009-0209-1_46.

[118] Yurkin M. A. User Manual for the Discrete Dipole Approximation Code ADDA 1.4.0. 2020. URL: https://github.com/adda-team/adda/blob/master/doc/manual.pdf.

[119] Dandini P. et al. Halo ratio from ground-based all-sky imaging. Atmospheric Measurement Techniques 2019;12:1295–1309. https://doi.org/10.5194/amt-12-1295-2019.

[120] Mishchenko M. I. and Macke A. How big should hexagonal ice crystals be to produce halos? Appl. Opt. 1999;38:1626–1629. https://doi.org/10.1364/AO.38.001626.

[121] Ulanowski Z. Ice analog halos. Appl. Opt. 2005;44:5754–5758. https://doi.org/10.1364/AO.44.005754.

[122] Muinonen K. et al. Light scattering by randomly oriented crystals. Appl. Opt. 1989; 28:3051–3060. https://doi.org/10.1364/AO.28.003051.

[123] Grünbaum B. Isogonal Prismatoids. Discrete & Computational Geometry 1997;18:13–52. https://doi.org/10.1007/PL00009307.

[124] Keller J. B. Geometrical Theory of Diffraction∗. J. Opt. Soc. Am. Feb. 1962;52:116–130. https://doi.org/10.1364/JOSA.52.000116.

[125] Bi L. et al. Diffraction and external reflection by dielectric faceted particles. Journal of Quantitative Spectroscopy and Radiative Transfer. International Symposium on Atmospheric Light Scattering and Remote Sensing (ISALSaRS'09) 2011;112:163–173. https://doi.org/10.1016/j.jqsrt.2010.02.007.

[126] Warren S. G. and Brandt R. E. Optical constants of ice from the ultraviolet to the microwave: A revised compilation. Journal of Geophysical Research: Atmospheres 2008;113. https://doi.org/10.1029/2007JD009744.

[127] Mishchenko M. I. Scale invariance rule in electromagnetic scattering. Journal of Quantitative Spectroscopy and Radiative Transfer. Light in Planetary Atmospheres and Other Particulate Media 2006;101:411–415. https://doi.org/10.1016/j.jqsrt.2006.02.047.

[128] Muinonen K. and Saarinen K. Ray optics approximation for Gaussian random cylinders. Journal of Quantitative Spectroscopy and Radiative Transfer 2000;64:201–218. https://doi.org/10.1016/S0022-4073(98)00147-2.